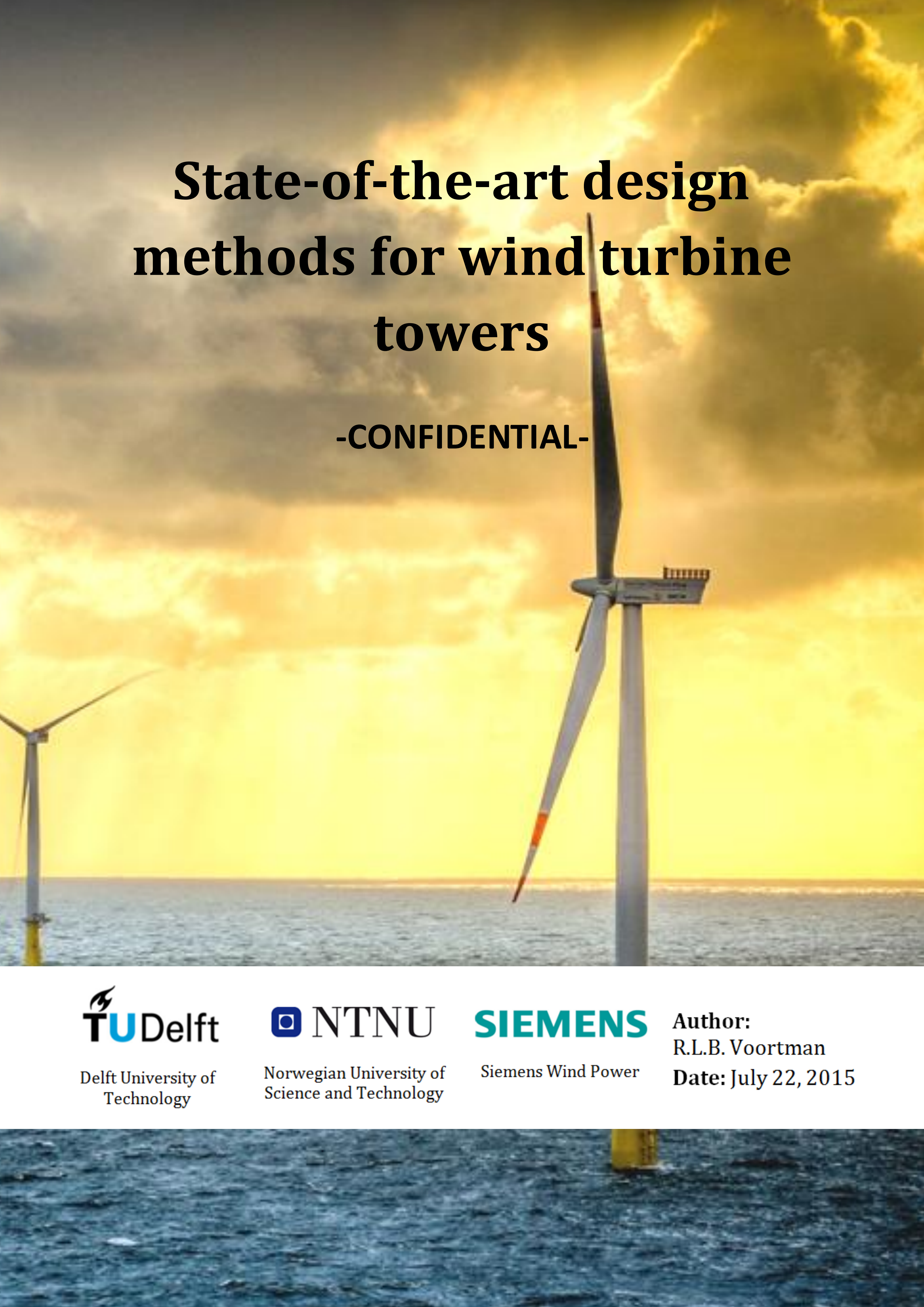

State-of-the-art design methods for wind turbine towers

-CONFIDENTIAL-

TUDelft
Delft University of Technology

NTNU
Norwegian University of Science and Technology

SIEMENS
Siemens Wind Power

Author:
R.L.B. Voortman

Date: July 22, 2015

Cover and back page:

Evening impression from the SylWin1 grid connection platform on two of the 70 3.6MW Siemens Wind Turbines located in offshore wind farm DanTysk in the North Sea [1].

State-of-the-art design methods for wind turbine towers

Master of Science Thesis

Ralph Lucas Bernard Voortman

-CONFIDENTIAL-

Graduation supervisors:

Prof. Dr. Ir. A.V. Metrikine	Delft University of Technology
Ir. J.S. Hoving	Delft University of Technology
Ir. P.S. van Lieshout	Delft University of Technology
Prof. Dr. Ir. T. Moan	Norwegian University of Science and Technology
Prof. Dr. Ir. Z. Gao	Norwegian University of Science and Technology
Ir. M.R. Claus	Siemens Wind Power
Ir. F. Wenneker	Siemens Wind Power

Date:

July 22, 2015

Abstract

The costs of wind energy have to be reduced in order to be competitive with conventional methods to generate electricity. The tower costs contribute significantly to the costs of a wind turbine. This thesis aims to suggest improvements in wind turbine tower design in comparison with industry standards nowadays in order to reduce the costs of wind turbine towers.

Nowadays tower flanges are modeled either not at all or as point masses in the aeroelastic code used for the load simulations. It has been investigated if modeling the mass, geometry and stiffness of the tower flanges influences the simulation results. Modeling the flanges lowers the first two eigenfrequencies (bending) by less than 1%. The mode shapes do not change and the differences in loads (+0.5%) and displacements (+2.5%) are found to be insignificant. The effect of geometry and stiffness is not contributing as much as modeling the mass. Modeling flanges as point masses is sufficient to represent the flanges in the aeroelastic code.

A constraint damping layer between the flange connections is proposed. Such a layer can be used to increase the damping of the tower. In this way, the fatigue loads on the tower can be reduced.

An improved flange design optimization method is suggested. A cost performance function is created, reducing the flange costs of more than 2.5% in comparison with the optimization method used nowadays within Siemens Wind Power.

Standardization of flange connections in wind turbine towers is considered. This is beneficial for the costs of handling equipment and tower internals, as project specific design and certification of these components can be omitted. Other advantages of flange standardization are risk mitigation and supply chain benefits. Standardization of the flanges with a fixed bolt pattern leads to a costs increase of almost 3% for the flanges. Additionally standardizing the flange width makes the flanges 7% more expensive. The cost benefits on tower internals and handling equipment are obvious, however not specifically investigated.

Improved fatigue life prediction methods are suggested. The tower sections can be designed less conservative if sector based fatigue loads will be considered. In combination with sector based SN-curves and stress concentration factors the tower can be orientated in such a way that the fatigue loads are less severe. In practice this means that the door frame should be directed in the least loaded direction. Up to 6% tower mass reduction can be realized for fatigue driven tower designs. However, this is only feasible with accurate load direction predictions.

The Effective Equivalent Stress Hypothesis (EESH), a multiaxial fatigue life prediction model proposed by literature, is implemented to investigate the influence of combined loading on tower welds. The phase angle between the stress components is a variable of the EESH and has significant influence on fatigue life predictions. A method is described that explains how the phase angle between the stress components can be calculated. Analyses showed however that for a tower weld the phase angle is hard to obtain. The original EESH is analyzed and has some drawbacks. The equivalent stress of the EESH is calculated with use of two factors: the effective damage sum ratio and the square root factor. The calculation of the effective damage sum ratio is a complex process for stochastic stress signals and the result is depending on assumptions made. Furthermore, the square root factor is independent of the shear stress magnitude, which does not correspond with reality. A simplified EESH is introduced in which this square root factor is omitted. This model is however not able to incorporate the out-of-phase angle and SCFs anymore. Both the original and simplified EESH are concluded not to be suitable methods for practical fatigue calculations of tower welds because of above mentioned drawbacks. Another method, the Gough-Pollard algorithm, is implemented. This algorithm is simple to apply and difference in damage contribution of the individual stresses is distinguished by using different SN-curves for the normal and shear stresses. For multiaxial fatigue calculations in tower welds, the Gough-Pollard algorithm is the preferred fatigue model out of the considered models. The method however does not incorporate the phase angle, which could be a suggestion for improvement.

According to the above multiaxial fatigue models, load safety factors between 1.16 and 1.40 are required when evaluating fatigue life in tower welds with the conventional uniaxial method. In this way the additional damage due to combined out-of-phase loading is incorporated in the fatigue life prediction. However, usage of correct multiaxial fatigue models instead of safety factors increases the accuracy of fatigue life predictions. More research should be done to generalize and validate the multiaxial fatigue models.

Acknowledgement

The work reported is my thesis for the Erasmus Mundus European Wind Energy Master – specialization Offshore Engineering. It's the last step towards obtaining my master's degrees in Offshore Engineering (TUDelft) and Wind Energy Technology (NTNU). Graduating is a challenging experience which I could never have done without the supporting people around me.

I would like to thank Prof. Metrikine, Prof. Gao and Prof. Moan for their professional and helpful assistance in performing this research. Furthermore I would like to thank Paula van Lieshout and Prof. Sonsino for their guidance concerning the fatigue part of this report and Jeroen Hoving for his presence in the graduation committee.

I'm very thankful I could carry out my research at the Siemens Wind Power department in The Hague. It was a great pleasure to be part of the team and want to thank all of them for the help and fun on the working floor. The good vibe at the office was motivating. I want to show my special gratitude towards my Siemens supervisors Marc Claus and Frits Wenneker. No question or request was ever too much for them. Their contributions were crucial for the report.

Besides that I would like to thank my friends I met before and during my studies for all the fun in and besides the study. Without all the little adventures in Enschede, Delft, The Hague, Copenhagen and Trondheim my student time wouldn't be complete. It made it much easier for me to stay focused at the times it was necessary.

Finally, I want to take this moment to express my gratefulness to my parents, brothers and sister for their love, support and encouragement throughout my whole life.

Contents

List of figures

List of tables

Nomenclature

Latin symbols	Unit	Explanation
A	$[m^2]$	Area
a	$[m]$	Distance inner flange bolt hole
a_l	$[m]$	Crack length
b	$[m]$	Distance outer flange bolt hole
c	$[m]$	Perpendicular distance from the neutral axis to the outer shell
D	$[-]$	Damage
d	$[m]$	Diameter
e	$[-]$	Size effect
E	$[N/m^2]$	Modulus of elasticity
En	$[j]$	Energy
f	$[1/s]$	Frequency
F	$[N]$	Force
F_h	$[-]$	Non-proportionality factor
G	$[N/m^2]$	Modulus of shear
H	$[-]$	Form factor
H	$[m]$	Wave height
K	$[N/m]$	Stiffness
k_1	$[-]$	SN-curve constant below knee point
k_2	$[-]$	SN-curve constant above knee point
K_{tb}	$[-]$	SCF due to bending
K_{tt}	$[-]$	SCF due to torsion
KI	$[-]$	Treshold stress intensity factor
l	$[m]$	Length
L	$[-]$	Spectrum length
M	$[N \cdot m]$	Moment
m	$[kg]$	Mass
m_1	$[-]$	Slope SN-curve below knee point
m_2	$[-]$	Slope SN-curve above knee point
MH	$[-]$	Material hardening factor
MW	$[10^6 j/s]$	Power unit
N	$[-]$	Number of cycles till failure
n	$[-]$	Counted number of cylces
R	$[-]$	Stress ratio
r	$[-]$	Share of load

S	$[N/m^2]$	Stress
SM	$[-]$	Sliding modulus
t	$[m]$	Thickness
W	$[m^3]$	Section modulus
w	$[m]$	Width

Greek symbols	**Unit**	**Explanation**
α	$[rad]$	Orientation of principal axes
μ	$[-]$	Damping ratio
δ	$[m/N]$	Elastic resilience
Δ	$[-]$	Range
ζ	$[-]$	Weibull scaling parameter
κ	$[-]$	Size effect factor
λ	$[-]$	Ratio in bolt calculations
ν	$[-]$	Poisson ratio
ρ	$[kg/m^3]$	Density
σ	$[N/m^2]$	Normal stress
τ	$[N/m^2]$	Shear stress
ϕ	$[rad]$	Plane angle

Abbreviations	**Explanation**
5MW-NRELT	5MW reference wind turbine designed by the NREL
6MW-SWT	6MW Siemens Wind Turbine designed by SWP
Amp	Amplitude
AMV	Arithmetic mean value
AVG	Average
BF	Bottom flange
BHawC	Bonus Energy Horizontal axis wind turbine Code
BT	Bolt type
CF	Cost factor
CPF	Cost performance function
CTOD	Crack tip opening displacement
DLC	Design load case
DNV	Det Norske Veritas
EDS	Effective damage sum
EESH	Effective equivalent stress hypothesis
EPFM	Elastic plastic fracture mechanics
ETM	Extreme turbulence model
FAD	Failure assessment diagram
FEM	Finite element model
FLS	Fatigue limit state
GL	Germanischer Lloyd
HAWC2	Horizontal Axis Wind turbine simulation Code 2nd generation
HH	Hub height
IIW	International Institute of Welding
LEFM	Linear elastic fracture mechanics
LMF	Lower middle flange
ML	Mud line
MPF	Mass performance function
MSL	Mean sea level

NB	Number of bolts
NCM	Normal current model
NREL	National Renewable Energy Laboratory
NSS	Normal sea state
RNA	Rotor nacelle assembly
SCF	Stress concentration factor
SHM	Structural health monitoring
SP	Scaling parameter
SS	Sea state
STD	Standard deviation
SWP	Siemens Wind Power
TF	Top flange
TI	Turbulence intensity
ULS	Ultimate limit state
UMF	Upper middle flange

Subscript	**Explanation**
a	Amplitude
A	Axial
bc	Bolt circle
be	Bending
cg	Coherent gust
$corr$	Correction
$crit$	Critical
dc	Detail category
eq	Equivalent
f	Flange
FM	Flange mass
i	Subscript
in	Inner
lim	Limit
md	Most damaging
n	Normal
np	Non-proportional
out	Outer
p	Flange plate
r	Range
R	Resistance
red	Reduced
rm	Raw material
sec	Secondary
sh	Shell
sig	Significant
t	Thickness
th	Threshold
to	Torsion
tot	Total
w	Weighted
x	Direction
y	Direction
z	Direction

Chapter 1

1 Introduction

1.1 Offshore wind energy

Wind energy plays a significant role in reducing greenhouse gas emissions and is essential for the European renewable energy targets for 2020. Of the almost 130 GW total installed wind energy capacity in Europe (2014), only 6.2 % consists of offshore wind energy [2]. The downside of offshore wind power is that the components should be able to resist harsh sea conditions and the installation is more complicated, making the investment per installed MW for an offshore wind turbine almost 40 % higher than for the onshore equivalent. However, in 2014 the installed offshore wind energy capacity has increased with more than 30%. The benefits are obvious: offshore the wind blows more often, the visual impact is lower and transportation of large components is easier. Europe's offshore wind potential is enormous and able to meet Europe's demand seven times over, as estimated by the European Environment Agencies [3].

1.2 Wind turbine technology

Different kind of offshore foundation types exist. Figure 1.1 gives an overview. From left to right the foundation types are monopile, gravity based, tripod, jacket and spar-buoy. The foundation selection depends on many factors such as turbine weight, environmental conditions, soil condition and sea depth. Tubular towers with monopiles are the most common structure for wind turbines (almost 80% of installed wind turbines in Europe [2]) for aesthetical, economical and safety reasons [4].

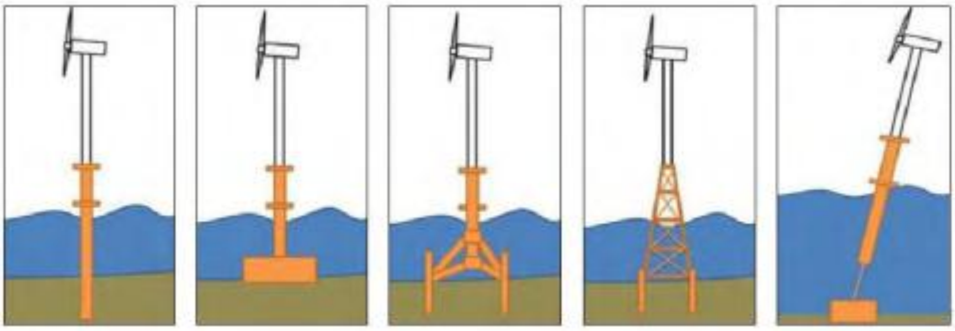

Figure 1.1: Offshore foundation types [5].

The names of the different components of an offshore monopile based wind turbine are given in Figure 1.2. The transition piece couples the tower with the monopile. Besides that, it offers a boat landing, ladder and a platform towards the door in the tower. The rotor and nacelle together is called the rotor nacelle assembly (RNA). This report will focus on the structural design of the tower.

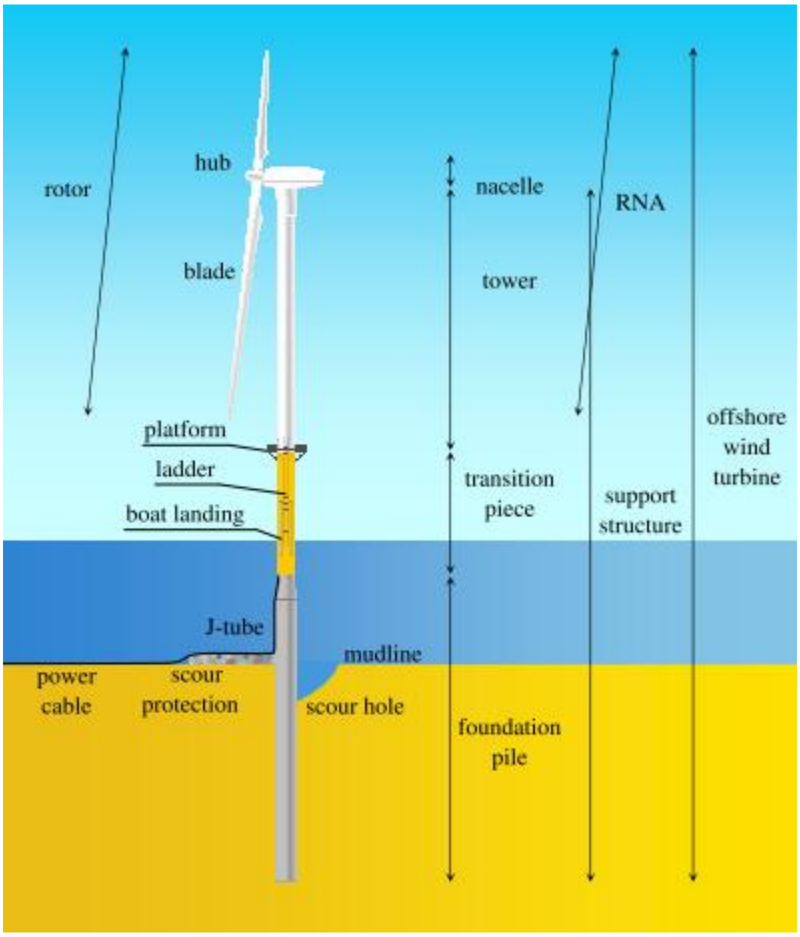

Figure 1.2: Offshore wind turbine component [6].

1.3 Importance of tower design

In order to compete with conventional energy resources, it is essential to reduce the costs of offshore wind energy. Some components in the value chain of an offshore wind farm carry more cost reduction potential than others. A study shows that approximately 15% of the turbine capital costs (RNA and tower) are determined by the costs for the tower [7]. Besides that, the design of the tower also influences the costs for installation and commissioning. This means that a reduction in the costs of the tower has a significant effect on the total costs of offshore wind energy.

1.4 Research objective

As the thesis title suggests, this thesis will considerer state-of-the-art design methods for wind turbine towers. This thesis aims to indicate and suggest improvements that can be made in offshore wind turbine tower design in comparison with industry standards nowadays in order to reduce the costs of the wind turbine tower.

1.5 Parties involved

The research described in this thesis is mostly carried out at the Siemens Wind Power (SWP) department in The Hague. One of the specializations of this department is offshore tower design.

SWP is a market leader in designing, manufacturing and maintaining offshore wind turbines. SWP is totally owned by Siemens by buying Bonus energy in Denmark in 2004. Driving down the cost of wind power is the key target as they strive to make renewable energy independent of subsidies. Siemens' market share of installed offshore wind power in Europe in 2014 was over 85% [2].

1.6 Thesis outline

After this introduction, the theoretical background of fatigue of materials, tower design and flange design will be discussed in Chapter 2. In Chapter 3 the flange Ultimate Limit State (ULS) and Fatigue Limit State (FLS) loads are determined for a reference wind turbine with use of the aeroelastic code HAWC2. Flanges are designed for this wind turbine and the influence of flange design on the global dynamical behavior will be analyzed by modeling the flanges in HAWC2. A suggestion for application of a flange damping layer is made. Chapter 4 discusses flange design improvements. A cost performance function for flange design optimization is introduced. Furthermore a flange standardization procedure is proposed and the costs and benefits are analyzed with use of SWP reference projects. Chapter 5 will discuss the benefits and drawbacks of sector based fatigue design. Multiaxial fatigue in tower welds will be analyzed in Chapter 6. The multiaxial fatigue models called the Gough-Pollard algorithm and Effective Equivalent Stress Hypothesis (EESH) are analyzed and applied on tower welds for different simulations and compared with the conventional uniaxial method using the nominal stress to calculate the fatigue damage. The thesis will be finalized with conclusions and recommendations.

Chapter 2

2 Theoretical background

The relevant theoretical fundamentals of fatigue of materials, tower design and flange design are described in this chapter. Section 2.1 will explain the basics of fatigue life calculations of structures, which is important in both flange and tower design. Section 2.2 will briefly cover the relevant basics of tower design. The flange design process and relevant flange issues are described in Section 2.3.

2.1 Fatigue life calculations of structures

In materials science, fatigue is the weakening of a material caused by repeatedly applied loads. A short theoretical background will be given on how the fatigue life of structures is calculated nowadays. Evaluating the fatigue life is of mayor importance in the design of wind turbine towers since it's subjected to highly dynamical loading. This theoretical background will explain how the fatigue life of materials can be calculated by use of engineering methods used nowadays. The connection with the physical background is tried to be explained.

2.1.1 SN-curve

The fatigue life of a component is normally presented in a stress life diagram, called a SN-curve or Wöhler curve. For this curve the stress range ΔS versus cycles till failure N is plotted. A SN-curve will in most cases have a span of several decades in cycles, and is therefore plotted on log-log format.

The high cycle range of fatigue life is above 10^3 cycles. SN data in the high cycle range tend to follow a log-linear relationship, the SN-curve, see Equation 2.1.

$$N \cdot \Delta S^{m_1} = k_1 \qquad \text{Equation 2.1}$$

The values for m_1 and k_1 depend on the considered component. These values depend for example on the stress concentrations due to the overall geometry and the residual stresses within the material due to a certain fabrication method.

The low cycle range below 10^3cycles is general not defined in relevant design standards because marine structures are not within this range [8]. At low stress ranges, specimens may theoretically have infinite fatigue life. In the case of constant amplitude loading there will be a threshold in fatigue crack growth rate. If the stress range gives a stress intensity range for the initial defect that is less than the threshold, the initial crack will not grow, and fatigue life is “infinite”. The fatigue limit is defined by:

$$S_{lim} = \frac{KI_{th}}{H\sqrt{\pi \cdot a_l}} \qquad \text{Equation 2.2}$$

With KI_{th} the threshold stress intensity factor below no stress growth takes place and H the form factor representing the boundary conditions of the considered fatigue location, important parameters in fracture mechanics. The value a_l represents the crack length [9].

In general for environmentally loaded structures some stress ranges will be above the fatigue limit, and some will be below. The cycles that are above the fatigue limit will cause crack growth (active cycles). As the crack grows, the fatigue limit will be gradually lowered, see Equation 2.2, and more cycles in the spectrum will become active [10].

In cumulative damage calculations, assuming a fatigue limit as found in constant amplitude testing, the resulting fatigue design will be non-conservative. If, on the other hand, the fatigue limit is ignored at all, the design may become over-conservative [11].

Haibach [10] used a fracture mechanics model to demonstrate that with a fictitious extrapolation of the SN-curve with a slope $(2m_1\text{-}1)^{-1}$ the effect of a growing crack on the fatigue threshold will be taken into account in cumulative damage calculations. The model is valid for stationary load histories, which is a good approximation for wave and wind loaded structures [12].

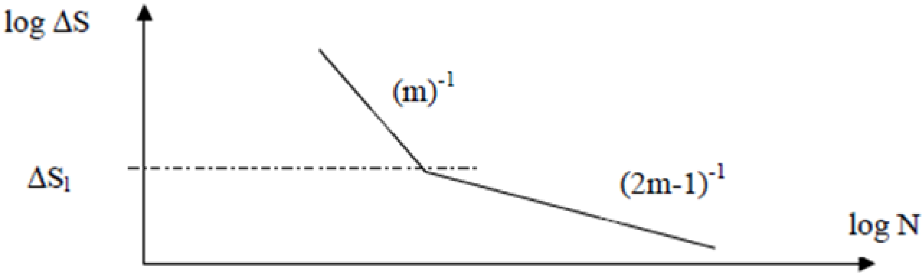

Figure 2.1: SN-curve with extrapolation beyond the fatigue limit [12].

2.1.2 Fatigue damage accumulation

Practically all fatigue design of steel structures and the damage calculations are based on the Miner summation procedure. In a stress history of several stress ranges ΔS_i, each with a number of cycles n_i the damage sum follows from:

$$D = \sum_i \frac{n_i}{N_i} \qquad \text{Equation 2.3}$$

Where N_i is the number of cycles till failure belonging to ΔS_i for a given SN-curve. In a constant amplitude test, this lead to the following failure criterion:

$$D_f \geq 1 \qquad \text{Equation 2.4}$$

The stress spectrum can be obtained by rainflow counting, the most used cycle counting algorithm. It produces a stress spectrum from a stress history that yields the same fatigue damage.

Figure 2.2 shows how with use of the stress spectrum (a) and SN-curve (b) the Miner summation procedure (c) can be applied to calculate the cumulative damage of a structure. The Miner summation is the most widely used cumulative damage models for failures caused by fatigue.

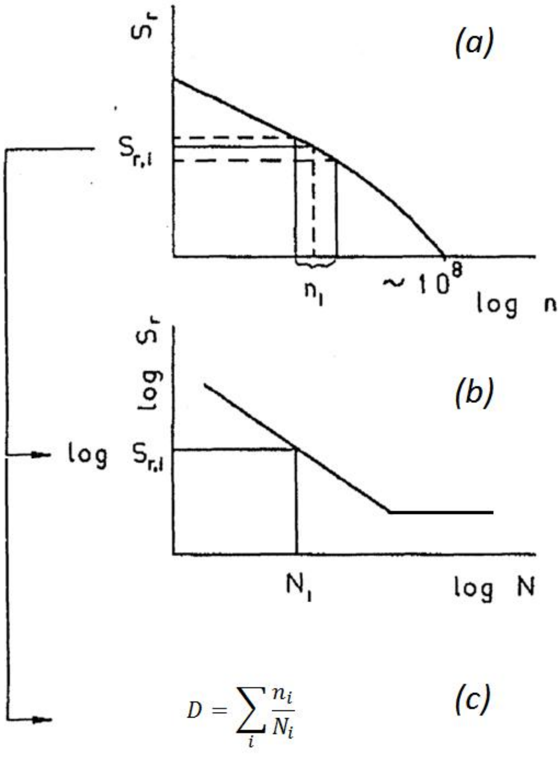

Figure 2.2: Fatigue calculation procedure [12].

2.1.3 Definition of stress categories

There are different concepts for the evaluation of the fatigue strength of welded structures. The most common concept is the nominal one. Generally, all design codes for welded structure are based on this concept. In a wind turbine tower, the nominal stress can be calculated with use of basic mechanical equations, see Section 2.2.3. Besides the nominal stress, also the hot-spot stress, structural stress or local stress can be used. Since in this report only the nominal stress will be used, the other concepts will not further be explained.

2.1.4 Fatigue scales

Fatigue problems can be viewed from different scales:

- Macroscopic scale (engineering scale)
- Mesoscopic scale (intermediate scale)
- Microscopic scale (physicist scale)

Most of the fatigue models are based on the macroscopic scale, the scale of the continuous medium. The traditional theories of fracture mechanics (Section 2.1.5) is continuum based.

The mesoscopic scale is the scale related to an elemental volume containing few material grains. Metal crystals and dislocations are known to possess some preferred orientations (slip systems) along which plastic strain can develop. It is long known that localized plastic strains developing in some crystals are the main cause of fatigue crack nucleation [13].

The microscopic scale is the scale of the dislocations. A dislocation is a linear of one-dimensional defect around which some of the atoms are misaligned. Experimentally observed characteristics of the crack dynamics or the crack-surface topography have to be modeled on this scale. For example, in the case of brittle fracture the crack at its tip must be atomically sharp and break the bonds between atoms. So, for the detailed understanding of fracture and crack propagation, an understanding in the atomic scale is needed. However, atomistic studies of fracture are rather computationally demanding. In the region away from the crack-tip, no atomic scale discretization is needed. This leads to the use of a multi-scale modeling approach that couples the crack propagation across several length and energy scales [14]. However, even a multi-scale model is often still too computational demanding for practical fatigue life prediction of structures.

2.1.5 Fracture mechanics

Fracture mechanics is used to evaluate the strength of a structure or component in the presence of a crack or flaw. Fatigue failure is brittle like in nature even in normally ductile metals, in that there is very little, if any, gross plastic deformation associated with failure. The process occurs by the initiation and propagation of cracks, and ordinarily the fracture surface is perpendicular to the direction of an applied tensile stress. Some ferrous and titanium alloys have a limiting stress level, called the fatigue limit, below which fatigue failure will not occur, see Section 2.1.1. Most of the nonferrous alloys (aluminum, copper, magnesium) do not have a fatigue limit [15]. The scatter in results is a consequence of the fatigue sensitivity to a number of test and material parameters that are impossible to control precisely. These parameters include specimen fabrication and surface preparation, metallurgical variables, specimen alignment in the apparatus, mean stress and test frequency [12].

2.1.5.1 LEFM vs. EPFM

Linear elastic fracture mechanics (LEFM) is used for material conditions which are predominantly linear elastic during the fatigue process. It is only valid when the size of the plastic zone is small relative to characteristic dimensions like plate thickness and the crack length. This is called small-scale yielding [16]. The fracture mechanics explanation in this section is based on LEFM.

Most engineering material show some nonlinear elastic and inelastic behavior under operating condition. Therefore a more general theory of crack growth is needed for elastic-plastic materials. Outside the validity range of LEFM, elastic plastic fracture mechanics (EPFM) should be applied. EPFM applies to materials that exhibit plastic deformation before fracture, which makes use of the crack tip opening displacement (CTOD). With use of this parameter a failure assessment diagram (FAD) can be made. The FAD method makes use of two ratios: brittle fracture and plastic collapse. With use of the CTOD, the stress intensity can be calculated. The plastic collapse ratio is calculated using a reference stress [9].

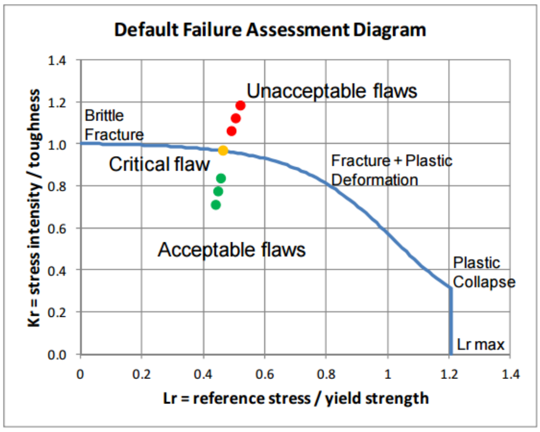

Figure 2.3: Example of the default FAD and crack evaluation points [17].

2.1.5.2 Process of fatigue failure

Within fracture mechanics, the process of fatigue failure is characterized by three distinct steps [18]:

1. Crack initiation, wherein a small crack forms at some point of high stress concentration.
2. Crack propagation, during which this crack advances incrementally with each stress cycle.
3. Final failure, which occurs very rapidly once the advancing crack has reached a critical size.

Fatigue stage 1: Crack initiation

This stage is also called stage 1 crack growth: slip tends to accumulate in distinctive bands, called persistent slip bands, leading to extrusions and intrusions on the surface. Stage 1 takes place within one or a few grains at the surface and is affected by the crystallographic structure of the material. There is no established theory for modeling stage 1 crack growth. In most design analyses Stage 1 is assumed to be part of the initiation stage.

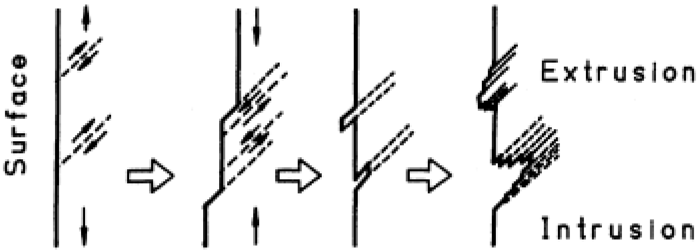

Figure 2.4: The development of persistent slip bands, extrusions and intrusions by cyclic slip [12].

Fatigue stage 2: Crack propagation and final failure

When a stage 1 fatigue crack has grown through the first grains, crack development is no longer affected by the crystallographic structure of a single grain, but will be dependent on average properties of the material. The crack orientation and shape will change to a fracture mode with the crack plane normal to the maximum fluctuating stress. This is referred to as stage 2 crack growth. Compared to stage 1, the crack growth rate per cycle is much larger.

Figure 2.5: Stage 2 fatigue crack growth under influence of stress range ΔS [19].

This stage can be modeled with use of a curve in which crack growth rate $\frac{da_l}{dN}$ is plotted against the stress intensity factor $K = S\sqrt{\pi a_l}H$ (see Equation 2.2). The crack growth curve may be considered as a material property.

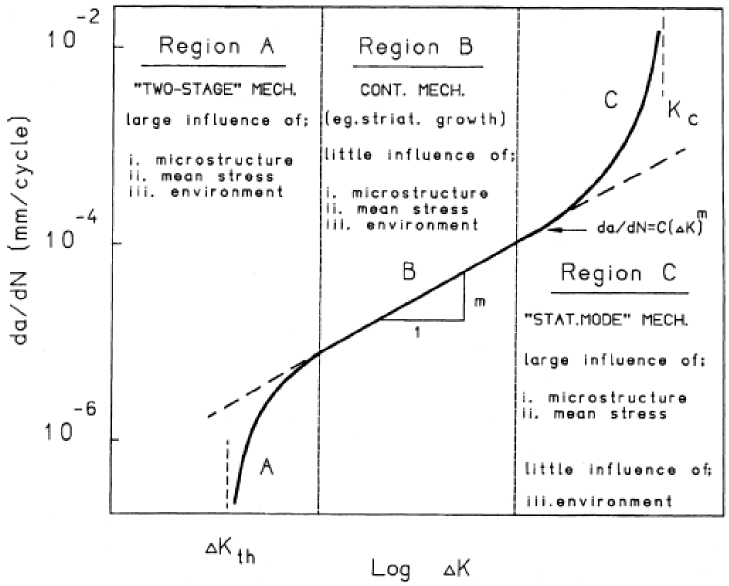

Figure 2.6: Schematic crack growth rate curve [12].

Threshold region

In most cases dealing with environmentally loaded structures, most of the crack growth history will be in the threshold region, where the crack growth rate is uncertain, influenced by a large number of parameters. Region A, the threshold region (Figure 2.6), can be modeled with use of methods by Klesnil and Lucas or Donahue [9]. However, for a welded joint, microstructure and mean stress are not controlled, and assessment of a crack growth curve in this region is uncertain. It is common to use an extrapolated Paris-Erdogan crack growth relation (Equation 2.5) or a cut-off in this region.

Finite life region

For region B (Figure 2.6), the finite life region, the crack growth curve may be approximated by the Paris-Erdogan crack growth relation.

$$\frac{da_l}{DN} = C(\Delta K)^{m_1} \qquad \text{Equation 2.5}$$

C and m_1 are fitting parameters, which can be seen as material parameters. Equation 2.5 can be rewritten in a SN-curve with use of a fracture mechanics analysis.

$$N = \int_{a_{l,initial}}^{a_{l,final}} \frac{d a_l}{C (\Delta K)^{m_1}} \qquad \text{Equation 2.6}$$

The exponent m_1 becomes the negative inverse slope of the SN-curve and the fitting parameter C can, in combination with the integral over the crack length, be rewritten in the constant k_1 used for describing the SN-curve (see Section 2.1.1) [12]. However, this approach can only be done if the linear elastic fracture mechanics approach is assumed.

Final failure region

In region C crack growth rate is accelerating rapidly and the growth can be modeled with the Forman equation [9]. For practical fatigue calculations, region C is of minor significance. In this region crack growth rate is so large that final failure is imminent.

2.1.5.3 Welded joints

For welded joints, crack propagation (fatigue stage 2) is dominating. The number of cycles in this stage is much larger than the number of cycles in the crack initiation stage (fatigue stage 1). This means that the crack propagation stage constitutes a major part of the fatigue life. The reason for this is that welding introduces many defects in the material. By post weld treatments like grinding or peening of the weld toe the slag intrusions may be removed, leading to an improved fatigue life due to the introduction of an initiation stage.

2.1.5.4 Application fracture mechanics

Fracture mechanics gives a good insight how cracks develop. However, fracture analysis is not always practical for analyzing the fatigue life of tower welds because of the following reasons:

- Most of the load history takes place in the threshold region of fatigue stage 2. It is common to use an extrapolated Paris-Erdogan crack growth relation (Equation 2.5) in the threshold region, which is actually only valid in the finite life region. Figure 2.6 shows that this is a conservative assumption.
- Even in sound welds, microscopic defects are present, acting as crack nucleation sites. The fatigue notch factor of a weld is therefore much greater than what can be predicted from the external geometry.
- Small crack are outside the validity range for linear elastic fracture mechanics.

However, when the cracks have developed, fracture mechanics analysis is useful for calculation of residual life, for inspection planning and for reliability assessment [12].

2.1.6 Multiaxial fatigue

Multiaxial random fatigue has been ignored by engineers for a long time, despite the fact that fatigue critical areas such as the weld toes of many structures are subjected to multiaxial states of stress–strain. The latter do not result only from local constraints (stress concentrations) but can also be caused by multiaxial external loading such as combined bending and torsion. Studies show that combined bending and torsion loadings give significant life reductions in comparison with pure bending loading [20].

Figure 2.9 shows that when loading comes from different directions (i.e. normal and shear loading, Figure 2.8) the fatigue life could be reduced dramatically. The state of stress at the root of a notch is usually multiaxial, even under uniaxial loading. If the secondary stress amplitudes are larger than 15% of the primary stress amplitudes [21] and when these signals are out-of-phase, taking multiaxiality into account is important for an accurate life time prediction. However, different methods available to calculate multiaxiality yield different results. Experiments should be conducted to validate these results and choose the most appropriate method or to come with a new unified and simplified approach. Understanding multiaxial fatigue will contribute in a more accurate fatigue life time prediction. In this way an improved justification of life time extension of a structure can be given, the maintenance and repair const can be reduced and the risk of component failure decreases.

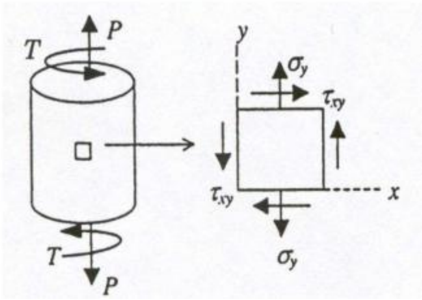

Figure 2.7: Multiaxial loading [22].

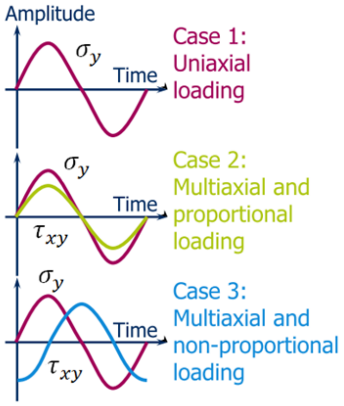

Figure 2.8: Proportional and non-proportional loading [23].

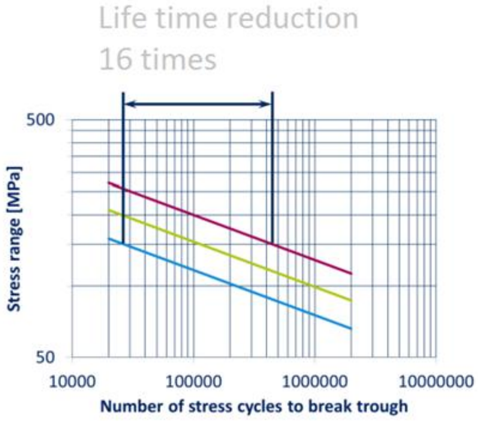

Figure 2.9: Fatigue life of multiaxial proportional and non-proportional loading of a ductile structural steel component according the Effective Equivalent Stress Hypothesis [24] [23].

2.1.6.1 Proportional vs. non-proportional loading

Before discussing proportional and non-proportional loading, a short introduction of Mohr's circle is given. Mohr's circle is a two-dimensional graphical representation of the transformation law for the stress tensor. After performing a stress analysis on a material body assumed as a continuum, the components of the stress tensor at a particular material point are known with respect to a coordinate system. The Mohr circle can then be used to determine the principal stress directions with respect to the reference coordinate system. The procedure of drawing the circle is explained in detail in [25].

During constant amplitude cyclic loading, as the magnitude of the applied stresses vary with time, the size of Mohr's circle of stress also varies with time. In some cases, even though the size of the

Mohr's circle varies during cyclic loading, the orientation of the principal axes (principal stress direction) with respect to the loading axes remains fixed (α=constant, see Figure 2.10). This is called proportional loading. In many cases, however, the principal directions of the alternating stresses are not fixed, but change orientation (α varies, see Figure 2.11). This type of loading is called non-proportional loading. The different stress paths are displayed in Figure 2.12.

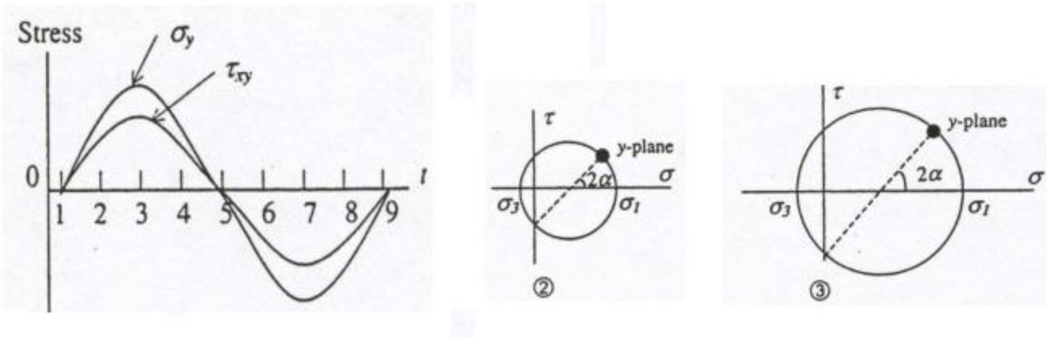

Figure 2.10: Mohr's Circles at proportional loading at time 2 and 3 [26].

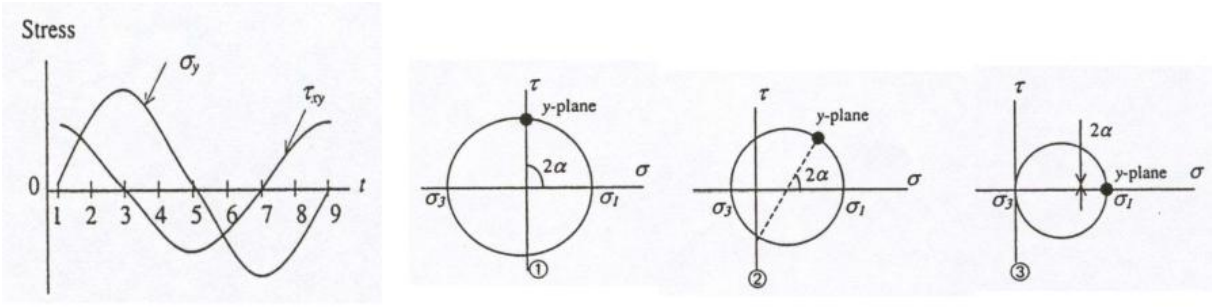

Figure 2.11: Mohr's Circles at non-proportional loading at time 1, 2 and 3 [26].

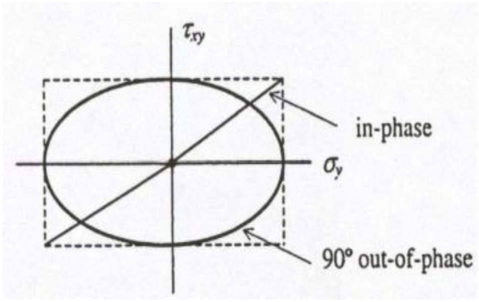

Figure 2.12: Stress paths for proportional (in-phase) and non-proportional (out-of-phase) loading [26].

At any instant the orientation of the principal stresses will depend on the ratio of normal stress to shearing stress on that face. This in turn will depend on the ratio of the bending and torsion loads. If in the time domain both torsion and bending follow constant amplitude sinusoidal cycles of the same frequency, and both are zero at time zero, this ratio will not vary in the time domain. Introducing a phase shift by, for instance, starting with the torsion input at maximum value when bending is zero, causes the ratio to vary with time, thus giving rotating principal axes [27].

Wind turbines subjected to out-of-phase torsion and bending are typical examples. The effects of non-proportional cyclic loading should not be ignored, since it can produce additional cyclic hardening and often results in a shorter fatigue life compare to proportional loading as can be seen in Figure 2.9. Besides that, a phase-shift between the loading components results in a reduction of fatigue life for ductile materials because due to the rotation of the plane with maximum shear stress, a larger number of slip systems is activated compared to the proportional loading. The effect is however dependent on the material; the fatigue life of steel decreases while aluminum components are not affected by non-proportional loading [23].

A device to validate different multi-axial fatigue models is depicted in Figure 2.13. This hexapod is suggested by the joint industry 4D-fatigue project team which focuses on the phenomenon of multi-axial fatigue in welded structural details and is planned to be build soon [28].

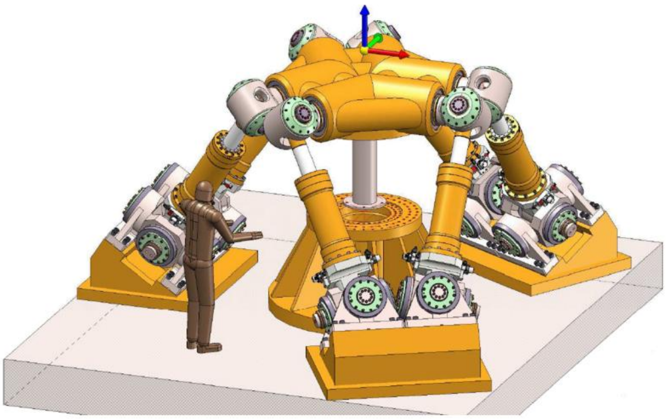

Figure 2.13: Hexapod to test multi-axial fatigue [28].

2.1.6.2 Multiaxial fatigue models

In general, multiaxial fatigue criteria can be grouped into two categories:

- integral damage parameters and
- critical plane approaches.

The integral damage parameters form a reference value averaged over all material planes of a material volume element. Energy based approaches are representative integral damage parameters. On the other hand, fatigue damage is related to the physical quantities specified on individual material planes of a material element. Often, fatigue failure is predicted when the fatigue damage accumulation on a material plane reaches a limit. The main argument in favor of the critical plane approaches is that the fatigue process is clearly related to specific material planes on which crack start to grow.

Another way to categorize the multiaxial fatigue theories is according to the major physical quantity used in the theory. Consequently, the theories can be classified as [26][19]:

- stress based;
- strain based;
- energy based;
- critical plane based and
- fracture mechanics based.

Their advantages and disadvantages will be discussed briefly.

Strain and stress based

Historically, most attention has focused on situations that require more than 10^4 cycles to failure where stress is low and deformation is primarily elastic. SN-curves are based on high-cycle fatigue situations. Where the stress is high enough for plastic deformation to occur (low cycle fatigue), the accounting of the loading in terms of stress is less useful and the strain in the material offers a simpler and more accurate description. The strain based approaches can deal with loading causing inelastic strain, (both high cycle and low cycle fatigue), but cannot take the non-proportional effect into account. This is due to the fact that non-proportional hardening is reflected by additional stress responses.

Energy based

Failure of a material should involve the absorption of energy. Therefore, an energy quantity is naturally used for considering fatigue failure. However, energy is a scalar quantity and many energy based approaches are formulated in terms of a critical plane concept, because purely energy based methods didn’t achieve the expectations [19]. Energy based approaches use products of stress and strain to quantify fatigue damage and can be used for non-proportional loading [26].

Critical plane based

Experimental observations indicate that cracks nucleate and grow on specific planes, the critical planes. Depending on the material and loading conditions, these planes are either maximum shear stress planes or maximum tensile stress planes. Multiaxial fatigue models relating fatigue damage to stress and or strains on these planes are called critical plane models. These models, therefore, not only can predict the fatigue life, but also the orientation of the crack or failure plane. Different damage parameters using stress, strain or energy quantities have been used to evaluate damage on the critical plane. Critical plane approaches attempt to reflect the physical nature of fatigue damage in their formulation and can predict both fatigue life as well as the orientation of the failure plane.

The ingredients of the critical plane criteria are the normal and shear stresses acting on a material plane. The various proposed formulae are different, but the process to follow is merely the same [13]. The fatigue crack will appear on the plane where the criterion is on its maximum. Besides the stress ranges, also the mean stress is sometimes taken into account. Besides the strains and stresses, often some material parameters are involved as well.

Fracture mechanics based

The fracture mechanics based approaches are critical plane approaches in nature. Fatigue is modeled as a crack growing process on a certain plane, the critical plane. If energy release rate is used as the crack driving force, the fracture mechanics based hypotheses can be rewritten in terms of energy based approaches.

2.1.6.3 Method to incorporate non-proportionality and additional hardening

For non-proportional loading, the additional hardening of material caused by the rotation of the principal stress/strain axes reduces the fatigue life of a component [22]. This phenomenon can be explained by the slip behavior of the material. The change of the principal stress/strain axes due to non-proportional loading allows more grains to undergo their most favorable orientation for slip and increases the interaction between slip systems, which is responsible for additional hardening [29].

Li [30] introduced a new equivalent stress by taking a correction factor F_{cor} into account which includes the non-proportionality factor (F_h) and material additional hardening factor (MH).

$$\sigma_{eq,Li} = F_{cor} \cdot \sigma_n \qquad \text{Equation 2.7}$$

$$F_{cor} = (1 + F_h \cdot MH) \qquad \text{Equation 2.8}$$

The non-proportional loading factor F_h can be calculated as follows:

$$F_h = \frac{\tau_{a,min}\tau_{a,w}}{\sigma_{eq}^2} \qquad \text{Equation 2.9}$$

This new path-dependent factor for multiaxial high-cycle fatigue can be stated the ratio of the multiplication of shear stresses to the equivalent stress squared according the von Mises criterion. The first shear stress component $\tau_{a,min}$ represents the minimum shear stress amplitude and the second component $\tau_{a,w}$ the weight value of shear stress amplitude on all planes, which can reflect the overall level of shear stress amplitude.

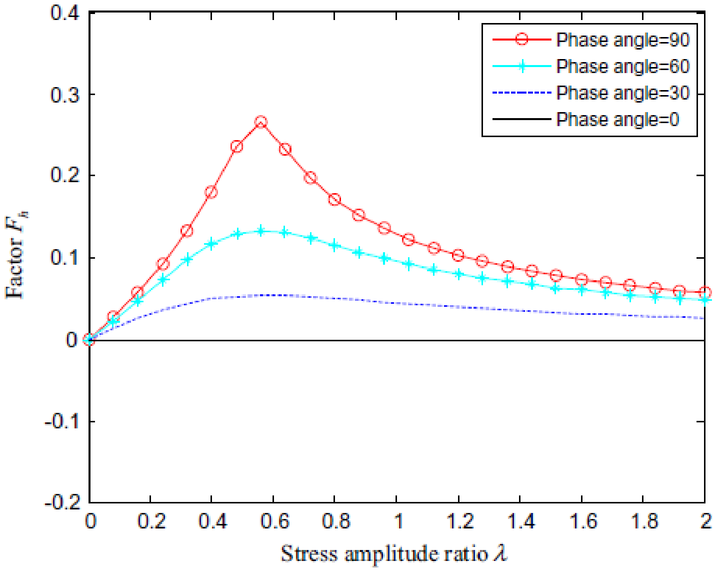

Figure 2.14: Correlation between the stress amplitude ratio λ and the factor F_h [30].

The stress amplitude ratio λ, the ratio between the shear stress and the normal stress, may have strong or weak influence on material fatigue strength, which is material dependent. Different materials may have different atomic arrays and different crystallographic orientations, which will also have a significant influence on activation of slip systems. Stress level, similar to stress amplitude ratio, also affects material fatigue strength due to that high stress level may easily lead to several crack initiation sites, while low stress level probably causes only one crack initiation site. The value of the non-proportional loading factor F_{np} depends on the stress amplitude ratio and phase angle as is seen in Figure 2.14. A maximum value of F_{np} = 0.27 will be found under a phase angle of 90°. The additional hardening parameter MH is determined with use of experiments. A reasonable assumed constant value for MH for steel used in tower section is 0.97. In this way the correction factor F_{cor} will vary between 1.0 and 1.23, depending on the phase angle and stress amplitude ratio.

2.1.7 Time domain vs. frequency domain fatigue calculations

The offshore wind industry standard (both onshore and offshore) is to use time domain simulations, which enables taking all non-linearities (aerodynamic loading, hydrodynamic loading, speed and pitch controls [31]) of the turbine operation into account. Frequency domain fatigue damage calculations are fast and easy to use for fatigue damage predictions [32]. It is convenient to use in the design phase of mechanical components, especially when the fatigue life is included in the objective function of optimal design.

Even if several issues are still under discussion, the frequency method has shown the significant beneficial effects in terms of computational effort. Both during the reconstruction of the stress state and during the post-processing by the multiaxial methods, the direct frequency approach has shown computational times suitable for the first stages of the design, when it is important to use quick and adaptable tools for the verifications of several alternative design configurations.

The principal advantage of this frequency-domain methodology is the capability to produce (exact or approximated) analytical expressions, by which cycle distribution and fatigue damage can be estimated without requiring knowledge of each stress or strain time history. The analytical solutions used are generally explicit functions of some spectral bandwidth parameters of the process power spectral density, which will become the main quantities controlling the fatigue damage [33].

As rainflow counting is the standard in the wind industry these days, a frequency domain approximation of the rainflow ranges has long since been investigated [34]. As the methods (Rayleigh, Rice and Dirlik) incorporate an increasing number of spectral moments, the ability to incorporate the broad-band-effects of the stress response should improve. The most accurate, when compared to time domain rainflow counting of the same event, is the Dirlik method [35]. This method is completely empirical. By running large numbers of broad-band signals in both time and frequency domain, the parameters in the Dirlik formula were tuned. No theoretical background exists. Despite the number of contributions, due to the complexity of the matter, the main issue concerning the relationship between fatigue damage and power spectral density of stress, strain or load is still open.

2.1.8 Structural health monitoring

Fatigue damage prognosis can be done with structural health monitoring (SHM) data. Some prognoses use fracture mechanics-based fatigue crack growth modelling.

Structural health monitoring is a discipline that aims to identify the health of a mechanical system through its lifecycle. The damage state of a system can be described as a five-step process to answer following questions: (1) Existence, is there damage in the system? (2) Location, where is the damage in the system? (3) Type, what kind of damage is present? (4) Extent, how severe is the damage? (5) Prognosis, how much useful life remains [36]?

Recently, wind turbine manufacturers, owners and operators have shown increasing interest in the SHM technology. Since the wind turbine systems are installed in off-shore wind parks or high elevation mountain regions with harsh environmental conditions, application of SHM technology will save maintenance and repair costs throughout its 10–30 year lifecycle. Moreover, implementation of an SHM system will assist in understanding wind turbine behavior under normal operational conditions in order to improve efficiency and lifetime at reduced material investment. Although the damage occurring to the tower is common, most research has mainly applied the SHM technology to the rotor blade and research of health monitoring of the tubular tower is still rare.

An SHM system is being considered to detect minor damage sites before they can combine and propagate to cause failure of the wind turbines. Strain measurement by strain gauges is a common technique, however not often applied for condition monitoring. Strain gauges have a short lifetime. For wind turbines, strain measurement can be very useful for lifetime prediction and safeguarding of the stress level, especially for the blades. More advanced sensors might open an interesting application area. Optical fiber sensors are promising, however still too expensive and not yet applied in wide range. Availability of cost effective systems, based on fiber optics, can be expected within some years. Strain measurement as condition monitoring input will then be more important.

This type of monitoring is mainly focused on crack detection and growth. Methods are normally off line and not suitable for on-line condition monitoring of wind turbines. An exception might be the usage of optical fuses in the blades and acoustic monitoring of structures [37].

In order to improve safety considerations, to minimize down time, to lower the frequency of sudden breakdowns and associated huge maintenance and logistic costs and to provide reliable power generation, the wind turbines must be monitored from time to time to ensure that they are in good condition. Among all the monitoring systems, the SHM system is of primary importance because it is the structure that provides the integrity of the system [38].

2.2 Tower design

76% of the installed wind turbines in Europe have a tubular tower structure. Tubular towers are made of different sections manufactured in the production facility and finally assembled on site. Nowadays towers often consist of 2 or 3 sections, having a cylindrical or conical shape.

For onshore towers, transportation constraints impose limits on the diameter and length of the elements. The diameter should be lower than about 4.3 m to pass under bridges and the elements length is comprised between 20m and 30m. These constraints don’t apply to offshore towers. Their limits are primarily determined by the lifting capacity or stability of the vessel.

Typical base diameters for offshore towers nowadays (4-6 MW) are 5-6m. The plate thicknesses for these towers vary from around 15 mm for the upper sections to more than 80 mm for the lower sections, depending on the turbine type and environmental conditions. The tower sections have a typical length of 10-36 m [39]. Within SWP, the tower design of the 6MW turbine (called the 6MW-Siemens Wind Turbine (6MW-SWT)) often looks like as depicted in Figure 2.15. Tower section 1 is connected with the RNA with use of the top flange connection (TF). The towers sections are connected with each other with use of the upper and lower middle flange connection (UMF and LMF, respectively) and the bottom flange connection (BF) connects the tower with the transition piece.

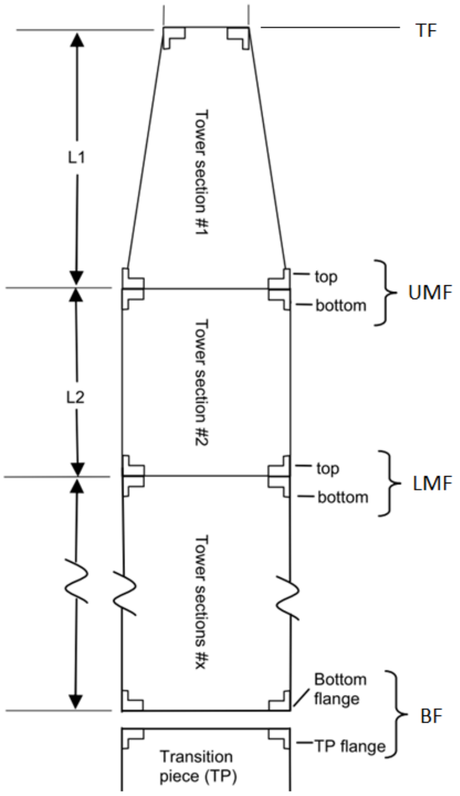

Figure 2.15: Tower sections with the corresponding flange connections [1].

2.2.1 Tower design method

In the current offshore wind turbine support structure design method, the tower and foundation, which form the support structure are designed separately by the turbine and foundation designer. This method yields a suboptimal design and it results in a heavy, overdesigned and expensive support structure. A multidisciplinary approach to design the tower and foundation simultaneously is developed nowadays. The result of the integrated multidisciplinary design optimization shows 12.1% reduction in the mass of the support structure, while satisfying all the design constraints [5].

Aerodynamics, hydrodynamics, structure and soil mechanics are the modeled disciplines that should be modeled to capture the full dynamic behavior of the foundation and tower under different environmental conditions. Different design constraints should be taken into account; local and global buckling, modal frequencies, and fatigue damage along different stations of the structure.

2.2.2 Structural dynamics

A wind turbine is constantly loaded. With a global structural dynamic analysis the deformations and eigenfrequencies of different components due to this loading can be determined.

The excitation of resonant tower oscillations by rotor thrust fluctuations at blade passing frequency (the so called 1P frequency) should be avoided. With a three bladed wind turbine, the excitation frequencies lay around the 1P and 3P frequency. Dynamic magnification impacts directly on fatigue loads, so the further the eigenfrequencies from the exciting frequencies, the better [40]. The excitation frequencies should at least differ 5% from the eigenfrequencies of the tower [41]. The first three eigenfrequencies of the tower are normally relevant in monopile based wind turbines. In general, the first eigenfrequency represents the frequency of the first mode in fore-aft direction and the second eigenfrequency the frequency of the first mode in side-to side direction. The third frequency represents the tower torsion frequency. Beside the blade passing frequencies, also the wave and wind frequencies should not cause resonance.

Two suitable locations for the first natural frequencies of an offshore tower are shown in Figure 2.16. The first eigenfrequencies can be calculated with:

$$f_{1,2} = \frac{1}{2\pi}\sqrt{\frac{K}{m}} \qquad \text{Equation 2.10}$$

K represents the tower stiffness and the tower mass. As can be seen are the first natural frequencies in the soft-stiff region, the most common place for these frequencies. Designing a tower with the first eigenfrequencies in the stiff-stiff region requires a very stiff structure (material inefficient).

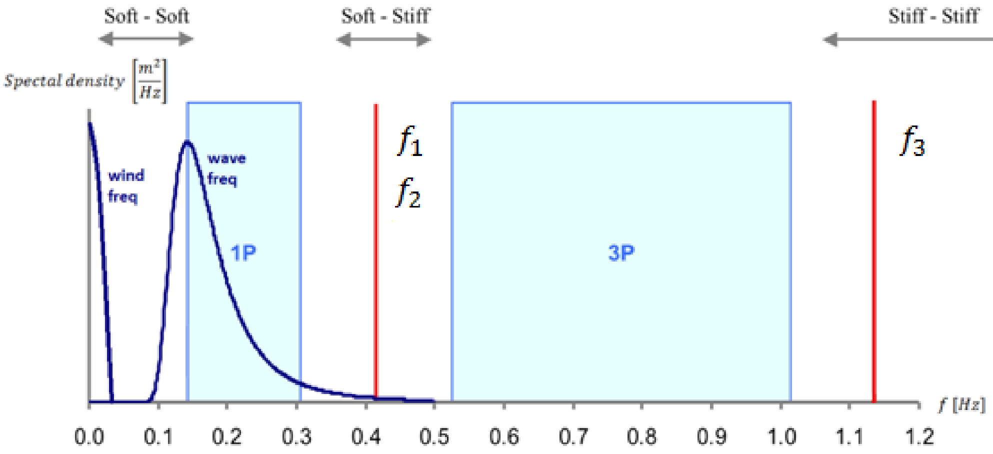

Figure 2.16: Relevant frequency spectra for wind turbine design [42].

2.2.3 Nominal stress calculations

With use of simulation programs like HAWC2 (Section 3.1) the moments and forces at a certain location in the tower can be simulated. With the following basic mechanical equations these moments (M) and forces (F) can be calculated into tower shell forces.

$$F_{sh} = \frac{M}{W_{sh}} \cdot A_{sh} - F_{z,mass} \qquad \text{Equation 2.11}$$

The section modulus W can be calculated with Equation 2.12.

$$W = \frac{I}{c} \qquad \text{Equation 2.12}$$

I represents the moment of inertia and c is the perpendicular distance from the neutral axis to the outer shell. The section modulus of the shell can now be written with use of the shell outer diameter d_{out} and shell thickness t_{sh}:

$$W_{sh} = \pi \cdot \frac{(d_{out})^4 - (d_{out} - 2 \cdot t_{sh})^4}{32 \cdot d_{out}} \qquad \text{Equation 2.13}$$

And the shell area as:

$$A_{sh} = \frac{1}{4} \cdot \pi \cdot \left(\frac{{d_{sh}}^2 - (d_{out} - 2 \cdot t_{Sh})^2}{2} \right) \qquad \text{Equation 2.14}$$

$F_{z,mass}$ is the total weight above the considered shell location.

2.3 Flange design

Nowadays practically all wind turbines consisting of tubular tower sections use bolted tower flange connections to connect the individual tower sections as well as the tower to the foundation/transition piece and the nacelle.

However, some research has been done on friction connections [43] and the company Northstarwind [44] even offers a wind turbine with this kind of connections. The tower has bolted friction joints both in longitudinal and lateral directions. Curved panels are assembled on-site to form cicular cross-sections. In this way a tower can be constructed without transportation limitations. This connection is however not interesting for offshore towers, where extra assembly efforts on site are highly expensive. This chapter will focus on the bolted tower flange connection, from now on just called flange connection.

2.3.1 Flange types

Two types of bolted tower joints are the T-flange and L-flange. The amount of bolts and dimensions should be chosen in such a way that the connection will not fail or deform in an unacceptable way under extreme loads. If the ultimate stress is reached, the connection will open and the bolts will be subjected to extra forces due to a lever effect of the flange, see Figure 2.17. The flange plate or the bolt will break with possible failure of the connection as a result [45]. Section 2.3.5.3 will give a more extensive explanation.

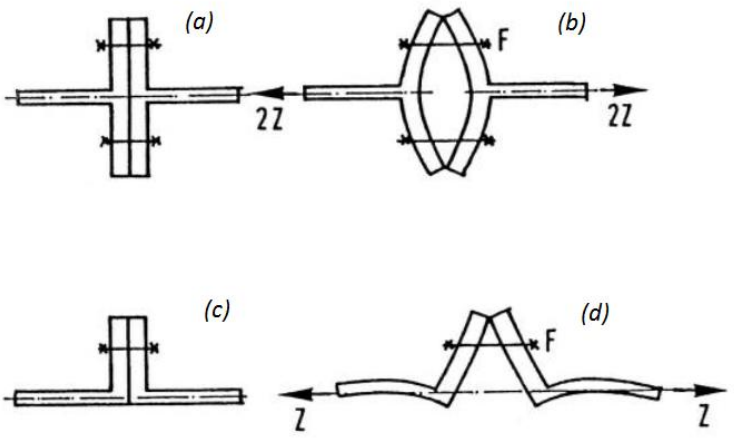

Figure 2.17: Unloaded and loaded T-flange connection (a and b) and L-flange connection (c and d) [45].

The most common connection between tower segments in wind turbines is the bolted L-flange, resp. single sided connection, as displayed in Figure 2.18. A pair of rather thick steel flanges are welded to the shell ends and bolted together with pre-tensioned high strength bolts.

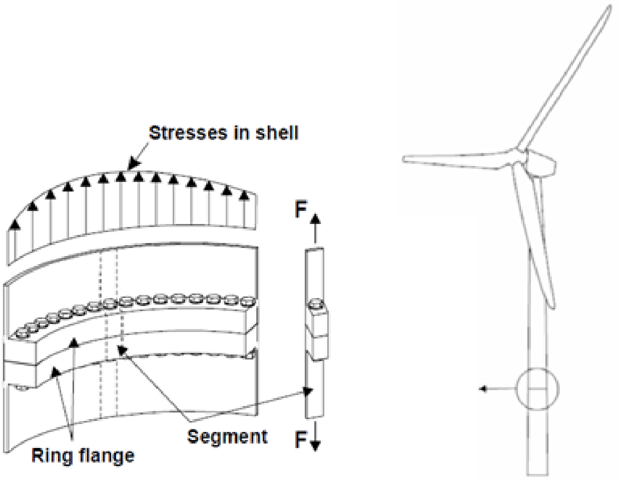

Figure 2.18: Flanges welded to the tower shell ends [46].

The bolted connection makes fast assembly during erection and easy disassembling at the end of lifetime possible. For the L-flange connection, during assembly no crew is needed outside the tower. This increases safety of working environment [41]. Another reason why not to use T-flanges is that sea water can stack on the flange that is sticking out, which will speed up corrosion. To conclude, L-flanges are more suitable for (offshore) tower connection than T-flanges. This is the reason that this report will focus on L-flanges. Figure 2.19 shows four different types of conventional L-shaped ring-flange connections.

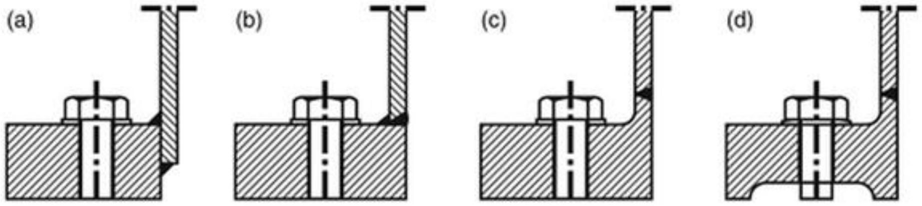

Figure 2.19: Scheme of different model types of conventional ring-flange connections: (a) slip-on flange, (b) welding on flange, (c) welding-neck flange and (d) welding-neck flange with defined contact area [45].

The welding-neck flange (type (c)) is the standard connection used in tubular wind turbine towers, because this connection is easy to weld and has a higher fatigue safety than the other welds. The weld quality can be checked easily due to several inspection techniques to find inner and outer flaws. The production costs are however around 30 % higher than type (a) or (b). Type (d) is rarely used because it the most expensive option due to extra machining.

2.3.2 Parameters in a flange connection

Figure 2.20 and Figure 2.21 display the most important geometrical dimensions of a flange connection. The different components will be discussed here.

2.3.2.1 Flanges

A flange connection consists of a lower and upper flange, which are bolted together. The geometry of the upper and lower flange of one connection is in general the same, only at the bottom and at the top flange connection this might not be the case. The top flange connection connects the upper tower section with the rotor nacelle assembly.

The flange holes are equally spread over the circumference so that the strength of the flange connection is equal in every direction. The amount of holes is dependent on the loads the connection should be able to resist. One side of the flange has a neck which is welded to the tower section. The flange holes are positioned as close as possible to inner diameter of the tower shells in order to get the strongest possible connection, see Section 2.3.5.3.

2.3.2.2 Bolts

The bolts connect the flanges. With use of bolt extenders the length of the bolted connection can be increased and hence the resilience (inversed stiffness) of the bolts. This will cause the bolt share of load to become smaller (and consequently the flange share of load larger), see Section 2.3.5.2.

Between the bolt head/nut and the flange material a washer is used. These are used to spread the load of a bolt over a larger area and to help prevent loosening under vibration.

2.3.2.3 Material

According to DNV design standard J101 [47], offshore structures above the lowest waterline shall be designed with service temperatures equal to the *lowest daily mean* temperature for the area where the unit is to operate. This is a conservative assumption, because materials have a higher change on brittle fracture at lower temperatures.

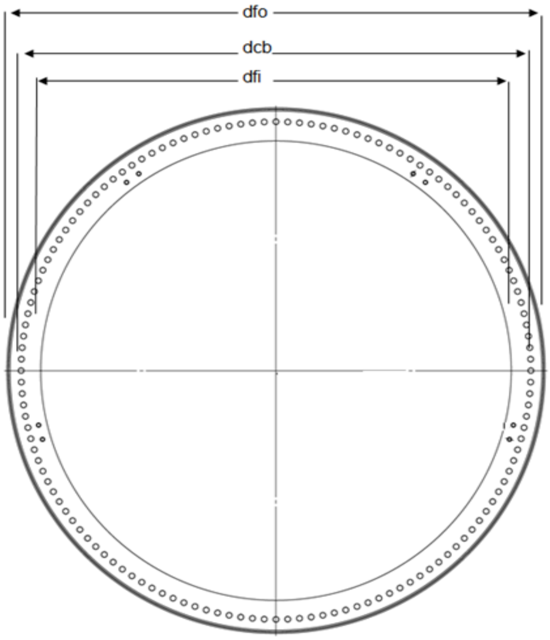

Figure 2.20: Flange top view [1].

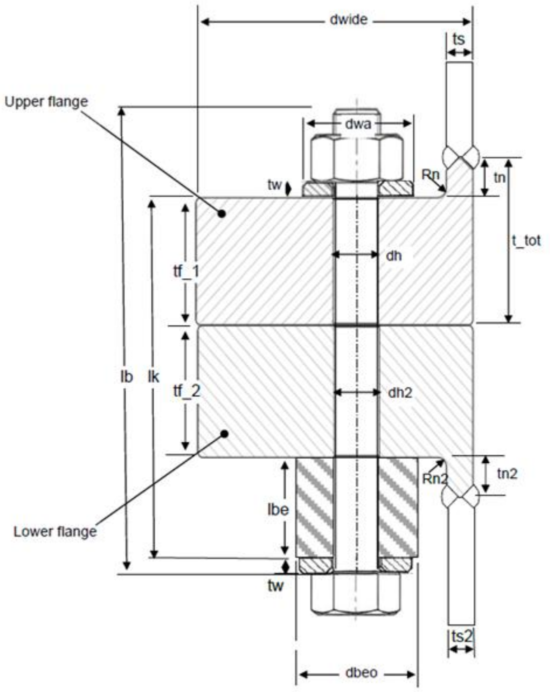

Figure 2.21: Flange segment section [1].

Abb.	Description
d_{fo}	Outer flange diameter
d_{cb}	Bolt circle diameter
d_{fi}	Inner flange diameter

Table 2.1: Abbreviations in Figure 2.20.

Abb.	Description
d_{wide}	Width of flange
t_s	Thickness of shell
d_{wa}	Outside diameter of washer
t_w	Thickness of washer
R_n	Weld neck rounding
t_n	Weld neck height
t_{tot}	Total height of flange
t_F	Thickness of flange
d_h	Diameter of flange hole
l_{be}	Length of bolt extender
d_{beo}	Outer diameter of bolt extender
l_b	Length of bolt
l_k	Clamp length

Table 2.2: Abbreviations in Figure 2.21.

2.3.2.4 Tool and bolt clearance checks

When choosing the position and amount of bolts in the flanges, it is important to consider the required space for the tightening tool, the washer and bolt extender, see Figure 2.22.

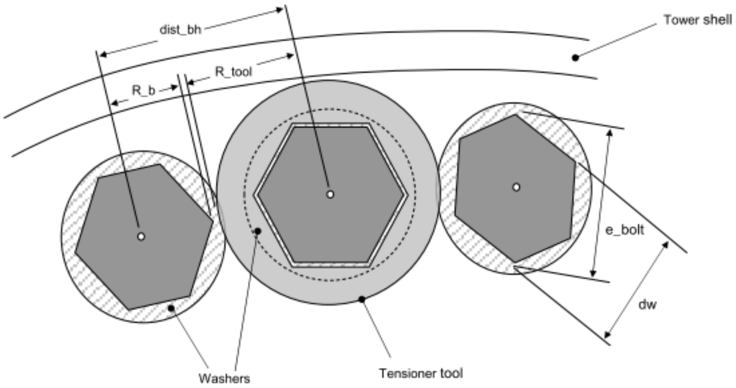

Figure 2.22: Spacing of the bolts [1].

2.3.3 Fabrication

The fabrication process of flanges is laborious and costly. Contact imperfections have a negative influence on the resistance and restricting tolerances are necessary. The flanges can be forged or more economically rolled from flat profiles and welded. They are then machined to the required dimensions and welded to the cans. Welding may introduce additional geometrical imperfections and if the tolerances are not met for the welded flange a second machining operation is necessary. To ensure perfect alignment of paired flanges the bolts holes are drilled using CNC machines [48].

2.3.4 Imperfections

Geometrical imperfections of the flanges may exist due to production flaws, damages due to transport or installation imperfections. These imperfections can have an influence on the forces through the bolts and are therefore of importance by calculation the maximum carrying capacity of the flange. The conservative calculation methods in the codes cover these imperfections, however more research could be done to decrease the imperfections and come with a more optimized flange design [39] [9].

Three different imperfection types are stated in Figure 2.23. Ovalization of the flange is another imperfection. Flanges do not always meet their roundness criterions once welded on the tower. The ovalization can to a certain extend be corrected by use of hydraulic jacks during installation. After installation the hydraulic jacks are removed. The following checks should be performed to see whether flange ovalization correction can be applied [1]:

- no yielding in the bolt material after the corrected flange connection is bolted together;
- shear < 30% of maximum allowable shear load;
- no yielding in flange.

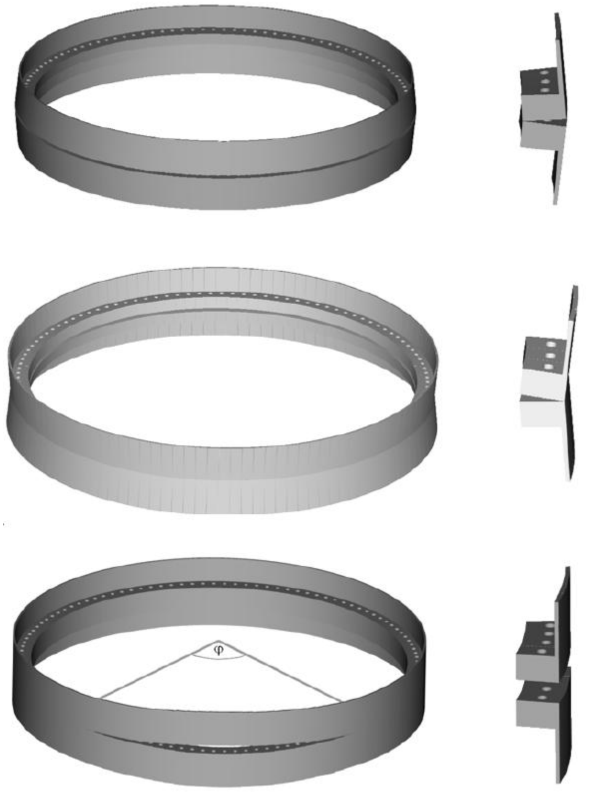

Figure 2.23: Different sorts of flange connection imperfections [49].

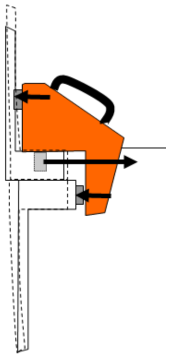

Figure 2.24: Hydraulic jack for flange correction [1].

2.3.5 Structural analysis of a flange connection

A bolted joint is intended to transmit forces and moments between the joined parts in a clearly defined position relative to one another. The bolts are to be designed in such a way that they withstand the loads which occur.

For design purpose it is assumed that the resistance of the three dimensional bolted ring flange connection which is loaded mostly in bending can be described by the resistance of a segment with a single bolt and a connection width equivalent to the arc length between bolts holes, see Figure 2.18. With help of numerical analyses of the whole system Seidel proved the correctness of this assumption [50].

2.3.5.1 Spring model

The forces and axial deformations in the single bolted joint can be described by means of a simple mechanical spring model. In this model, the bolt and the clamped parts are considered as tension and compression springs with the elastic resiliences δ_S and δ_p, respectively. Resilience is the ability of a material to absorb energy when it is deformed elastically, and release that energy upon unloading. Proof resilience is defined as the maximum energy that can be absorbed within the elastic limit, without creating a permanent distortion [51]. Appendix A shows how the resilience of the bolt and the clamped plate can be calculated.

Figure 2.25 shows the conversion of an axial clamped joint into the spring model. F_A represents the axial working load.

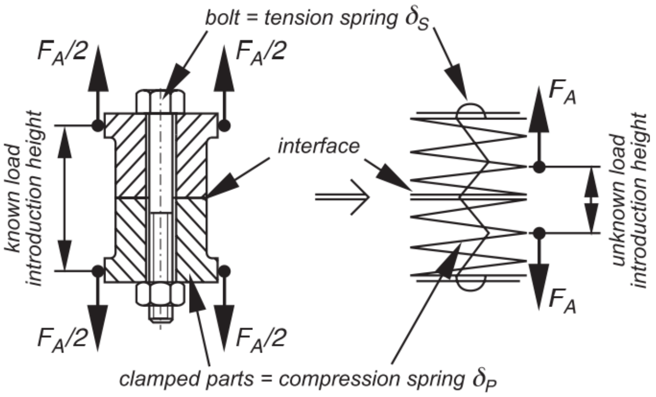

Figure 2.25: Simple spring model [25].

The simple spring model is valid for axis symmetrical bolted joint connections and assumes a linear relation between the axial working load and the bolt load. For bolted L-flange connections of wind turbine towers this is however not the case. The relationship between the axial working load (force in the shell) and the bolt force in a L-flange connection is non-linear as can be seen in Figure 2.26.

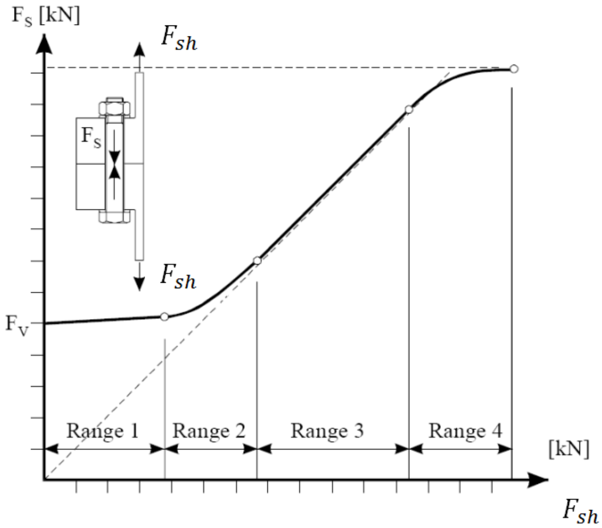

Figure 2.26: Non-linear relation between shell force and bolt force [49].

In range 1 the bolt force remains constant and equivalent to the pretension while the contact pressure between the flanges decreases progressively. At the beginning of range 2 the joint opens, i.e. the contact zone decreases and progresses outwards until edge bearing at the beginning of range 3. Disadvantageous prying effect then leads to bolt forces greater than the forces in the shell. Their ratio is function of the flange geometry which determines the lever arm acting on the bolt [39]. Plastic deformation of the bolt will take place in range 4 with bolt failure as consequence.

2.3.5.2 Resilience and clamp solid

For the strength and fatigue analysis of a flange connection, the resiliences (inversed stiffness) of both the flange and the bolt have to be determined. To calculate these values, the geometry of the so called *clamp solid* is important.

The clamp solid is the clamping region between the bolt head or nut and the interface of the clamped parts. This zone under compressive stress widens from the bolt head or nut toward the interface and has the shape of a paraboloid of revolution. However, this will be represented in a simplified manner by a substitution deformation cone of the same resilience.

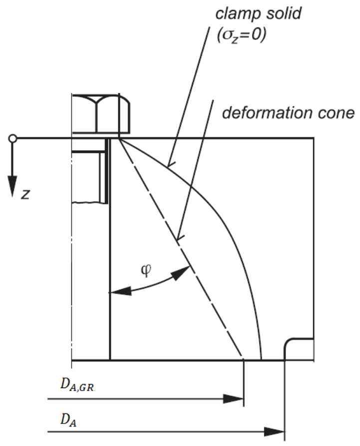

Figure 2.27: Clamp solid and deformation cone [50].

The deformation cone angle ϕ in joints with standard bolts can be calculated with use of the VDI guideline [25]. This angle is used to calculate $D_{A,GR}$, the maximum diameter of the deformation cone, depicted in Figure 2.27. This parameter is used in resilience calculations. In above figure this value is smaller than the basic solid diameter at the interface D_A. If the diameter at the interface is smaller than the deformation cone diameter, the resiliences have to be calculated in a different way than when this is not the case, see Appendix A.

With use of the resiliences the bolt share of the load r_s and the flange share of the load r_p can be calculated, see Equation 2.15 and Equation 2.16.

$$r_s = \frac{\delta_p}{\delta_s + \delta_p} \qquad \text{Equation 2.15}$$

$$r_p = \frac{\delta_s}{\delta_s + \delta_p} \qquad \text{Equation 2.16}$$

This means the following relation exists:

$$r_s + r_p = 1$$ Equation 2.17

Besides for the resilience calculations, the stress cones can be used to check if they overlap for two neighboring bolts, in order to prevent opening of the joint between the bolts (in the imaginary case where you have a lightly loaded flange with very few bolts) [1].

In general, in L-shaped flange connections the bolts are positioned close to edge of the flange and not in the middle. The parameter S_{sym}, the distance S between the bolt axis and the imaginary laterally symmetrical clamp solid, has a non-zero valid, see Figure 2.26. This means that the connection is eccentrically clamped. The forces on the flanges are transmitted by the tower sections. These shells are welded at the sides of the flange. The distance a, from the line of action of the axial working load to the axis of the laterally symmetrical clamp solid has a non-zero value. The connection is eccentrically loaded.

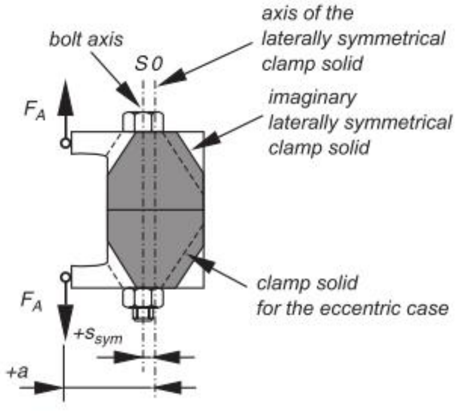

Figure 2.28: Eccentric loading and clamping [50].

2.3.5.3 *Strength calculations*

The verification of the ultimate limit state (ULS) of flanges is usually performed according to the plastic hinge theory developed by Petersen [45], which is extended by Seidel [51]. Petersen original approach contains three possible failure modes: A, B and C. Seidel enhanced the calculation by replacing failure mode C by two failure modes D and E. Even though bolts in ring-flange connections are pre-loaded, the pre-tensioning load in bolts is not to be considered in the ULS verification.

The connection resistance is taken as the lowest resistance from the failure modes A, B, D and E. To prevent failure of the flange connection, the connection resistance F_U should be higher than the design force in the tower shell. Table 2.3 gives a description of the modes. Figure 2.29 and Figure 2.30 show the models used to describe the failure modes.

The following assumptions are made:

- The flange is made out of structural steel.
- The flange is regarded at a beam with the width of one bolt.
- The limit states are calculated based on the theory of yield hinges.

Appendix B describes the calculation of the different failure modes and the abbreviations used in Figure 2.29 and Figure 2.30.

Failure Mode	Description
A	Bolt yielding due to tension.
B	Failure of the bolt due to tension and yield hinge in tower shell.
D	Yield hinge in tower shell and in flange material, additional bending stiffness of bolts is included.
E	Assumed yield hinge in flange in middle of the washer.

Table 2.3: Petersen/Seidel failure mode description.

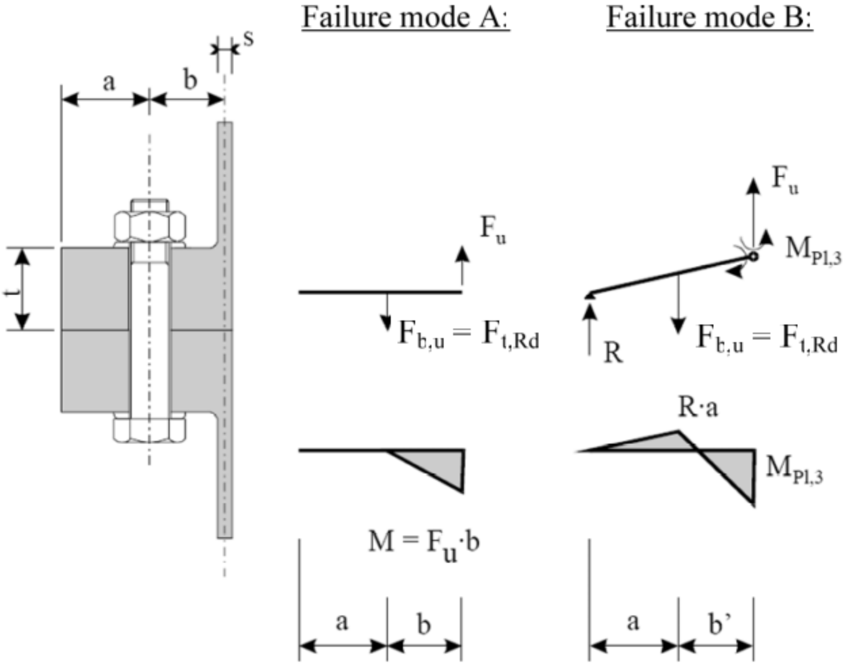

Figure 2.29: Failure modes A and B according Petersen [45].

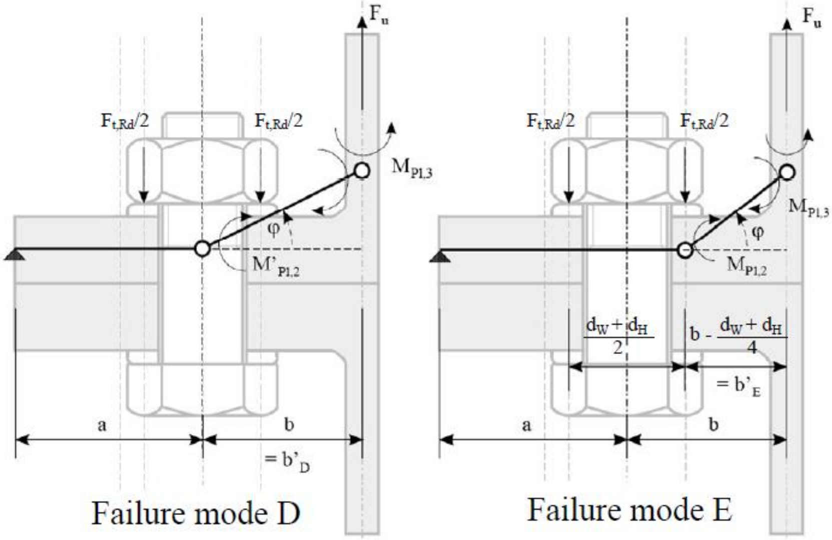

Figure 2.30: Failure modes D and E according Seidel [51].

2.3.5.4 *Fatigue calculations*

Fatigue failure of flange connections is governed by the fatigue resistance of the bolts which is intrinsically low due to the stress concentrations introduced at the thread foot [39]. This is the reason why in literature and in common practice only the fatigue of the bolts in a flange connection will be considered. The relation between forces in the shell, due to external loading, and the bolt stresses is already discussed with use of Figure 2.26. The different ranges are discussed as well.

With regard to fatigue safety, ring-flange connections should be designed in such a way that the bolted joint stays in the elastic regime. This requires a sufficient high pre-loading of the bolt, which should be larger than the pre-stress decrease in the flange plates due to the external loading [27].

The pre-stress by the bolt, S_v, is determined by the bolt characteristics and is defined as in Equation 2.18.

$$S_v = \frac{F_v}{A_s} \qquad \text{Equation 2.18}$$

With A_S the surface area of the bolt. The pre-stress force by the bolt F_v can be found in design guidelines [50].

In the next sections the most common bolt-load functions used in fatigue calculations will be explained. This bolt-load function is described by Schmidt-Neuper [17] .

Bolt-load function

Schmidt-Neuper models the real bolt-load function with use of a tri-linear function which is described by Equation 2.19 - Equation 2.24 [52][48]. The function is displayed in Figure 2.31. Experiments show that that this approximation comes very close to the real bolt function range 1 and 2. Range 3 is modeled quite conservative.

$$\lambda = \frac{0.7 \cdot a + b}{0.7 \cdot a} \qquad \text{Equation 2.19}$$

$$F_{sh,1} = \frac{a - 0.5 \cdot b}{a + b} \cdot F_V \qquad \text{Equation 2.20}$$

$$F_{sh,2} = \frac{1}{\lambda \cdot r_s} \cdot F_V \qquad \text{Equation 2.21}$$

$$F_{S,range\,1} = F_V + r_p \cdot F_{sh} \qquad \text{Equation 2.22}$$

$$F_{S,range\,2} = F_V + r_p \cdot F_{sh,1} + \left(\lambda \cdot F_{sh,2} - \left(F_V + r_p \cdot F_{sh,1}\right)\right) \cdot \frac{F_{sh} - F_{sh,1}}{F_{sh,2} - F_{sh,1}} \qquad \text{Equation 2.23}$$

$$F_{S,range\,3} = \lambda \cdot F_{sh} \qquad \text{Equation 2.24}$$

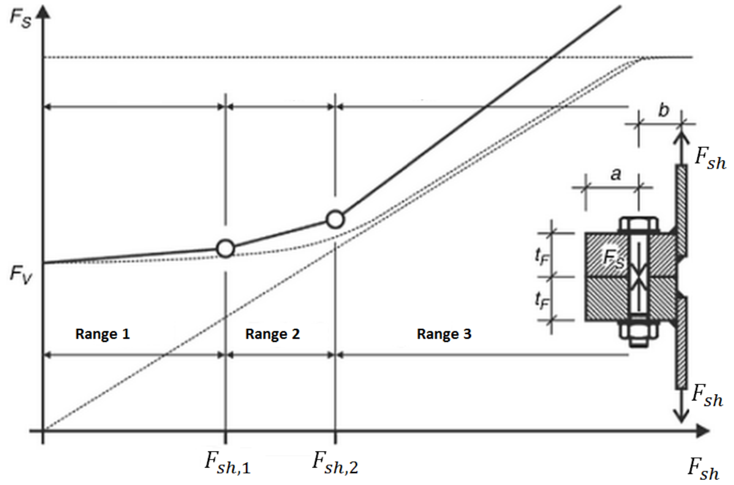

Figure 2.31: Bolt-load function representation according Schmidt-Neuper [45].

SN-curve

According to the GL and EN 1993-1-9 guidelines [53] [54], the reduced detail category 50 is sufficient for high strength bolts when the bending moments are taken into account. This means that the reference value of the fatigue strength at 2 million cycles is 50 MPa. However, for bolt diameters (d_s) larger than 30 mm a size effect e_{size} should be applied.

$$e_{size} = \left(\frac{30}{d_s}\right)^{0.25} \qquad \text{Equation 2.25}$$

The reduced reference value of the fatigue strength at 2 million cycles is given as:

$$\Delta\sigma_{red} = e_{size} \cdot \Delta\sigma_{dc} \qquad \text{Equation 2.26}$$

The fatigue limit will be represented by a change in the curve at 5 million cycles (m changes from 3 to 5, see Section 2.1.1).

For M42 and M48 bolts, used in the next chapter, this means that the SN-curve can be constructed with the values listed in Table 2.4 and Equation 2.27 and Equation 2.28.

$\boldsymbol{BT}$	$\boldsymbol{m_1}$	$\boldsymbol{\Delta\sigma\ [Mpa]}$	$\boldsymbol{\Delta\sigma_{red}\ [MPa]}$	$\boldsymbol{k_1 = (2 \cdot 10^6 \cdot \sigma_{red}^3)}$	$\boldsymbol{m_2}$	$\boldsymbol{\Delta\sigma_2 [MPa] = \left(\frac{k_1}{5 \cdot 10^6}\right)^{\frac{1}{m_1}}}$	$\boldsymbol{k_2 = (5 \cdot 10^6 \cdot \sigma_2^5)}$
M42	3	50	45.97	$1.94 \cdot 10^{11}$	5	33.85	$2.23 \cdot 10^{14}$
M48	3	50	44.46	$1.76 \cdot 10^{11}$	5	32.77	$1.89 \cdot 10^{14}$

Table 2.4: SN-curve parameters for M42 and M48 bolts.

$$\Delta\sigma^{m_1} \cdot N = k_1\ for\ N < 5 \cdot 10^6 \qquad \text{Equation 2.27}$$

$$\Delta\sigma^{m_2} \cdot N = k_2\ for\ N > 5 \cdot 10^6 \qquad \text{Equation 2.28}$$

The shape of these curves is explained in Section 2.1.

Chapter 3

3 Flange loading and influence of flange design on global dynamical behavior

This chapter investigates the loading on the flange connections and its influence on the global dynamical behavior of an offshore wind turbine. The 5MW offshore reference wind turbine designed by the National Renewable Energy Laboratory (5MW-NRELT) will be used for this purpose [55]. An initial design for the offshore foundation is made with use of environmental data.

Section 3.1 gives an introduction about the aeroelastic code HAWC2. In Section 3.2 it will be explained how the offshore foundation is designed and which simulations will be used in order to calculate the loading at the flange locations. In Section 3.3 the maximum moments and forces at the flange locations will be considered for two different ultimate limit state (ULS) cases. The fatigue limit state (FLS) will be discussed in Section 3.4. Section 3.5 explains the flange design process for the 5MW-NRELT. An extensive fatigue analyses will follow in Section 3.6. Section 3.7 will explain how these flanges are modeled in HAWC2 in order to investigate their influence on the global dynamical behavior. In Section 3.8 the influence of the mass and flexibility of the flanges on the global dynamical behavior of the wind turbine will be investigated. The final section will discuss the influence of damping of the flanges and will introduce a method how this damping can be increased.

3.1 HAWC2 introduction

The aeroelastic code HAWC2 is intended for calculating wind turbine responses in the time domain and has a structural formulation based on multi-body dynamics. The programme makes use of Timoshenko beams[56]. The aerodynamic part of the code is based on the blade element momentum theory, but extended from the classic approach to handle dynamic inflow, dynamic stall, skew inflow, shear effects on the induction and effects from large deflections. It has mainly been developed within the years 2003-2006 at the aeroelastic design research programme at Risoe, National laboratory Denmark, but is continuously updated and improved [57].

In Figure 3.1 the blue coordinate system represents the main body coordinate system and the black coordinate system represents the wind directions.

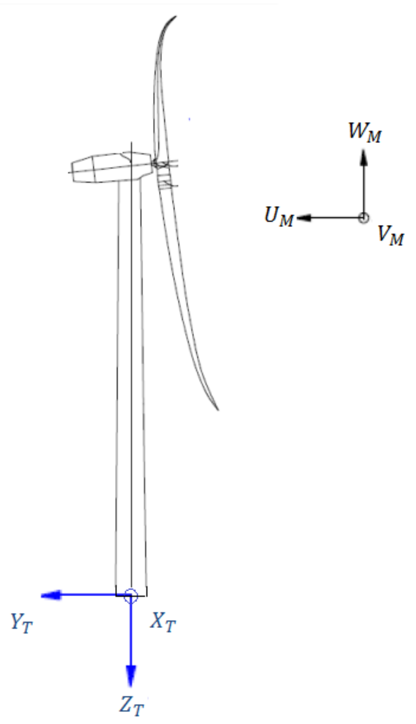

Figure 3.1: HAWC2 wind (black) and body (blue) coordinate systems [57].

3.2 Reference wind turbine, location and environmental data

The details of the 5MW-NRELT are listed in Appendix D. The fictive wind turbine, used to calculate the loads at the flange locations, is located in the Dutch North Sea 70 km north west of Den Helder. The environmental data are retrieved from that location. Appendix E shows an analysis of the data package and displays the lumped sea states used for the simulations.

The support structure of an offshore wind turbine has a location dependent design. This support structure is in this case a monopile. The monopile is connected to the wind turbine tower with use of a transition piece, see Figure 1.2. For simplicity, in the HAWC2 analysis this transition piece is considered to be part of the monopile. To establish a realistic model for the HAWC2 simulations, the so called interface level has to be determined. This interface elevation is the distance from the mean sea level to the top of the transition piece. After this elevation is calculated, the hub height can be determined (assuming a fixed tower height, following the 5MW-NRELT specifications). Table 3.1 summarizes the calculated elevation values. Appendix E shows the calculations done to determine these values. The different flange locations are depicted in Figure 3.2.

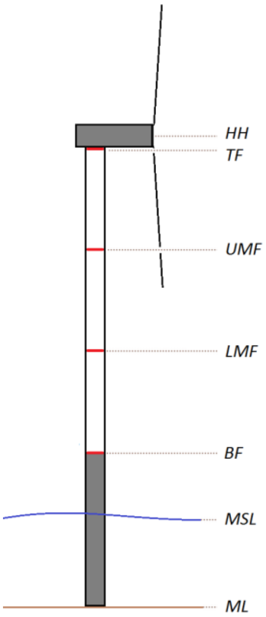

Figure 3.2: Flange locations.

Abbreviation	**Level**	**Relative height [m]**
HH	Hub height	107.5
TF	Top flange	105
UMF	Upper middle flange	77
LMF	Lower middle flange	47
BF	Bottom flange	17.3
MSL	Mean sea level	0
ML	Mudline	-25

Table 3.1: Elevation values.

3.3 Flange ULS loading

With use of the HAWC2 simulations the loading on the flanges will be determined. In this section a description will be given of the ULS simulations in HAWC2. The next scheme gives an overview of how the ULS calculations can be done [42].

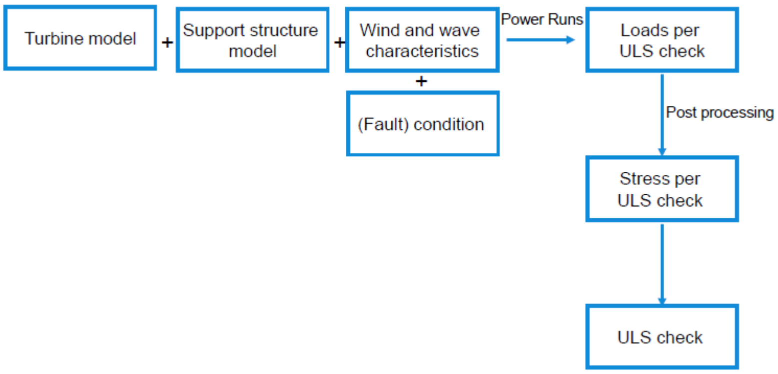

Figure 3.3: ULS check overview [42].

For design purposes, the life of an offshore wind turbine can be represented by a set of design situations covering the most significant conditions that an offshore wind turbine may experience. In this report only two design load cases (DLCs) according to the IEC 61400-3 guideline [58] will be considered: power production with extreme turbulence (DLC 1.3) and power production with extreme gust (DLC 1.4). These DLCs have a good potential to give the highest loads from all ULS DLCs, however other ULS DLCs may exist which give higher loads (emergency shutdown/parked and fault conditions for example). To prevent many load simulations it's assumed that investigating the aforementioned DLCs is sufficient to get a rough estimate of the ULS loading at the flange locations.

HAWC2 is able to calculate the moments around the axes and the forces along the axis at defined locations in the structure. In the following analyses the moments are not calculated at a specific point on the circumference of the tower, but will for simplicity be calculated as:

$$M_{tot} = \max\left(\sqrt{M_x^2 + M_y^2}\right) \qquad \text{Equation 3.1}$$

From the HAWC2 outputs the vertical force in the tower shell can be calculated (Equation 2.11).

3.3.1 First ULS load case: DLC 1.3

DLC 1.3 according to IEC 61400-3 embodies the requirements for ultimate loading resulting from extreme turbulence conditions. Normal sea state conditions shall be assumed for this design load case and the significant wave height for each individual sea state shall be taken as the expected value of the significant wave height conditioned on the relevant mean wind speed. This can be subtracted from the give data package. The ULS load case has the specifications as stated in Table 3.2.

Operating conditions	Power production
Wind conditions	Turbulence Intensity (TI) according the Extreme Turbulence Model (ETM)
Sea conditions	Normal Sea State, Normal Current Model, Mean Sea Level
Wind and wave directionality	Codirectional (same direction), Unidirectional (wave and wind direction don't change in time)

Table 3.2: DLC 1.3 specifications.

The focus will be on the critical condition; the largest wind loads (around rated wind speed). For every wind speed the sea state with the closest wind speed is chosen with corresponding significant wave height H_{sig} and spectral period T_{spec}, see Appendix E. A yaw error of 8 degrees should be considered. The simulations are performed with three different seeds per simulation. One simulation takes 10 minutes.

DLC	V_{wind} $[m/s]$	SS [#]	$TI\ (ETM)$ [%]	H_{sig} $[m]$	T_{spec} $[s]$	$Current$ $[m/s]$	$Yaw\ error$ $[deg]$
1.3a	$V_{rated} - 2$ (9.4)	13	29.9	0.75	4.92	0.55	0
1.3b							8
1.3c	V_{rated} (11.4)	9	27.5	1.75	7.04	0.55	0
1.3d							8
1.3e	$V_{rated} + 2$ (13.4)	7	15.6	1.75	5.86	0.55	0
1.3f							8

Table 3.3: DLC 1.3 parameters.

3.3.1.1 Result discussion

The results of these simulations are displayed in the following tables. Graphs of the time series can be found in Appendix F.

DLC	$\boldsymbol{M_{BF}}$ $[\boldsymbol{MNm}]$	$\boldsymbol{M_{LMF}}$ $[\boldsymbol{MNm}]$	$\boldsymbol{M_{UMF}}$ $[\boldsymbol{MNm}]$	$\boldsymbol{M_{TF}}$ $[\boldsymbol{MNm}]$		$\boldsymbol{F_{BF}}$ $[\boldsymbol{MN}]$	$\boldsymbol{F_{LMF}}$ $[\boldsymbol{MN}]$	$\boldsymbol{F_{UMF}}$ $[\boldsymbol{MN}]$	$\boldsymbol{F_{TF}}$ $[\boldsymbol{MN}]$
1.3a	72.5	48.6	26.7	8.1		42.5	32.2	19.8	5.2
1.3b	71.4	49.2	26.9	8.0		41.7	32.7	19.9	5.1
1.3c	77.6	52.2	27.5	9.5		46.0	35.1	20.6	6.7
1.3d	84.5	56.1	28.9	10.4		50.6	38.0	21.8	7.5
1.3e	54.6	37.1	21.1	7.6		30.3	23.4	14.8	4.6
1.3f	57.6	37.6	20.8	7.5		32.3	23.7	14.5	4.5

Table 3.4: DLC 1.3 results; 10 min, 3 different seeds simulation results.

From Table 3.4 it can be concluded that the moments in the tower at the bottom flange are the highest. This is logical since the arm of the moment is the longest here. Together with the moments, also the forces in tower shell (Equation 2.11) are the highest at the bottom. This means that the bottom flange should be able to resist the highest loads.

The highest loading takes place at rated wind speed. The considered wind turbine is a pitch regulated wind turbine, which means that when the wind speed exceeds the rated wind speed, the wind loads become smaller due to pitching of the blades. This means that the thrust on the rotor is the highest at rated wind speed.

Table 3.5 and Table 3.6 show the means and standard deviations of the moments.

	Mean fore-aft moments $[\boldsymbol{MNm}]$	**Mean side-to-side moments** $[\boldsymbol{MNm}]$	**Mean yaw moments** $[\boldsymbol{MNm}]$	**Mean tot moments** $[\boldsymbol{MNm}]$
BF	4.50	4.92	1.20	1.20
LMF	2.95	4.62	1.20	1.20
UMF	1.44	4.32	1.20	1.20
TF	0.87	4.06	1.20	1.20

Table 3.5: DLC 1.3 mean values; 10 min, 3 different seeds simulation results.

	STD fore-aft moments $[\boldsymbol{MNm}]$	**STD side-to-side moments** $[\boldsymbol{MNm}]$	**STD yaw moments** $[\boldsymbol{MNm}]$	**Mean tot moments** $[\boldsymbol{MNm}]$
BF	11.2	3.66	3.10	1.20
LMF	7.63	2.36	3.10	1.20
UMF	4.31	1.15	3.10	1.20
TF	2.55	0.38	3.10	1.20

Table 3.6: DLC 1.3 standard deviations; 10 min, 3 different seeds simulation results.

The mean and the standard deviation of the fore-aft and side to-side-moments become larger the lower the flange is located as can be concluded from Table 3.5 and Table 3.6. The increasing weight of the tower the lower flanges have to carry is the reason why the mean of the for-aft moment become larger. The standard deviation becomes larger because the distance to the prime force location (hub) and hence the arm of the moment becomes larger.

The mean and the standard deviation for the yaw moments are the same at every flange. The torque in the structure does not change over height, because the rotor is the only source of the torque.

3.3.2 Second ULS load case: DLC 1.4

DLC 1.4 according to EIC 61400-3 specifies a transient case which has been selected as a potentially critical event. Normal sea state conditions shall be assumed and the significant wave height for each individual sea state shall be taken as the expected value of the significant wave height conditioned on the relevant mean wind speed. Again wind speed around the rated wind speed will be considered, as these wind speeds generate the highest thrust. It may be assumed that the wind and waves are codirectional prior to the transient change in wind direction.

Operating conditions	Power production
Wind conditions	Extreme coherent gust with direction change (ECD)
Sea conditions	Normal Sea State, Normal Current Model, Mean Sea Level
Wind and wave directionality	Codirectional (same direction), Unidirectional (wave and wind directions don't change in time)

Table 3.7: DLC 1.4 specifications.

The extreme coherent gust with direction change shall have a magnitude of $V_{cg} =$ 15 m/s [58]. The simulations are performed with three different seeds. One simulation takes 10 minutes. The above gust is applied in the simulation after 5 minutes.

DLC	V_{wind} $[m/s]$	SS [#]	$TI\ (ETM)$ [%]	H_{sig} $[m]$	T_{spec} $[s]$	$Current$ $[m/s]$
1.4a	$V_{rated} - 2$ (9.4)	13	18.5	0.75	4.92	0.55
1.4b	V_{rated} (11.4)	9	17.6	1.75	7.04	0.55
1.4c	V_{rated} (11.4)	7	15.6	1.75	5.86	0.55

Table 3.8: DLC 1.4 parameters.

3.3.2.1 Result discussion

The maximum moments and forces of these simulations are displayed in the following table. The means and standard deviations are not showed, because these are of no interest after having discussed the ones from the first DLC.

DLC	M_{BF} $[MNm]$	M_{LMF} $[MNm]$	M_{UMF} $[MNm]$	M_{TF} $[MNm]$		F_{BF} $[MN]$	F_{LMF} $[MN]$	F_{UMF} $[MN]$	F_{TF} $[MN]$
1.4a	76.2	45.2	23.8	11.8		44.8	30.1	17.0	9.1
1.4b	93.2	50.0	24.6	16.3		50.0	33.3	17.7	13.7
1.4c	67.2	43.4	23.5	12.8		38.6	28.1	16.8	10.0

Table 3.9: DLC 1.4 results; 10 min, 3 different seeds simulation results.

Especially during the gust rise peak moments are visible, see Appendix F. During the rise time the largest moment occurs (1.4b at bottom flange, 93.2 MNm).

3.3.3 Result discussion both ULS load cases

The maximum values of the moments and the forces in the tower shell during the two considered load cases are displayed in Table 3.10.

	M_{BF} $[MNm]$	M_{LMF} $[MNm]$	M_{UMF} $[MNm]$	M_{TF} $[MNm]$		F_{BF} $[MN]$	F_{LMF} $[MN]$	F_{UMF} $[MN]$	F_{TF} $[MN]$
Max	93.2	56.1	28.9	16.4		56.3	38	21.8	13.9
DLC [-]	1.4b	1.3d	1.3d	1.4b		1.4b	1.3d	1.3d	1.4b

Table 3.10: DLC maxima; 10 min, 3 different seeds simulation results.

DLC 1.3d and 1.4b yield the highest values. Both maximum DLCs occur at rated wind speed. During this wind speed the rotor generates the highest thrust. From Table 3.10it can be concluded that this maximum thrust force value also causes the highest moments and forces at the considered four locations in the tower shell.

3.4 Flange FLS loading

For dynamically loaded structures, fatigue assessment is essential. The fatigue strength assessment will be carried out on the basis of a cumulative damage ratio, as described in Section 2.1.2. The next scheme summarizes how the fatigue calculations for the four flanges are done in this report [42].

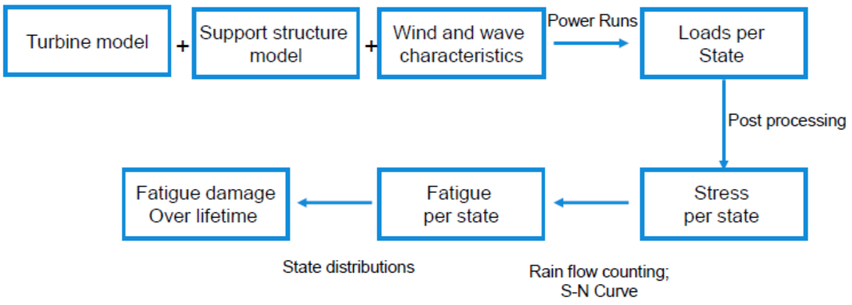

Figure 3.4: Fatigue calculation steps [42].

The fatigue calculation are performed according DLC 1.2 in the IEC 61400-3 guideline. In real fatigue calculations there are more DLCs to consider, but an assumption is made that considering this DLC will give a rough estimate for the fatigue loads at the flange locations.

The specifications from Table 3.11 will be used for the fatigue calculations. The wind speeds, wave heights and wave spectral periods as defined in the combined sea states from Appendix E will be used.

The normal turbulence model will be applied. For the fatigue calculations, unidirectional loads are assumed. This means that both the wind and wave loads only act in a single direction. The most prevailing wind direction is 240 degrees, for all wind speeds, see the wind rose in Appendix E. It is assumed that the wind always comes from this direction. The same for the waves; it is assumed that they always come from their prevailing direction of 330 degrees, as is depicted in Appendix E. The wind turbine is assumed to be yawed into the wind direction.

Operating conditions	Power production
Wind conditions	Normal Turbulence Model
Sea conditions	See combined sea states
Wind and wave directionality	Unidirectional

Table 3.11: FLS specifications.

3.5 Flange design

With use of the calculated ULSs and FLSs the BF, LMF, UMF and TF can be designed. Section 2.3.5 explains in detail which failure modes it should be able to resist. Besides that it explains more about the flange fatigue calculations. The input parameters for the flange designs are listed in Table 3.12. The used bolt type is M42.

Fixed parameters	**Abbreviation**	**BF**	**LMF**	**UMF**	**TF**
Distance to tower top $[m]$	z_{top}	87	57	27	0
Flange outer diameter $[m]$	d_{out}	6.0	5.2	4.6	4.0
Design max bending moment $[MNm]$	M_{Be}	93.2	56.1	28.9	16.4
Design max torsional moment $[MNm]$	M_z	9.8	9.8	9.8	9.8
Tower mass above flange $[ton]$	m_{tf}	350	200	85	0
Shell thickness $[mm]$	t_{sh}	35	32	28	25

Table 3.12: Flange fixed parameters.

With use of the Siemens flange tool, flanges with the properties as given in Table 3.13 are designed. These properties will be used as input in the HAWC2 structural data file.

Variable parameters	**Abbreviation**	**BF**	**LMF**	**UMF**	**TF**
Flange width $[m]$	w_f	400	370	350	350
Flange plate thickness $[mm]$	t_f	120	110	105	100
Total resilience flange and bolt section $[10^{-9}\ m/N]$	δ_{tot}	0.99	0.94	0.91	0.88
Nr of bolts $[-]$	NB	124	108	100	100
Equivalent flange E-modulus $[MPa]$ $(N_b \cdot \frac{1}{\delta_{tot}})$	E_{eq}	125	114	109	113
Equivalent flange G-modulus $[MPa]$ $(\frac{E}{2\ (1+\upsilon)})$	G_{eq}	48	44	42	44

Table 3.13: Flange variable parameters.

3.6 Flange fatigue life analysis

In general the fatigue of a flange connection is determined by the fatigue life of the bolts [1]. As bolts perform poorly when subjected to oscillating loads, the correct determination of stresses in the bolt for fatigue design is an important task in order to obtain a safe and economic design [54].

The bolts are loaded by the forces in the shell. The forces in the shell can be calculated with use of the external moments and the weight of the tower (Equation 2.11). The stresses in the bolts can be calculated from these shell forces with use of the flange geometrical values and the bolt load function described in Section 2.3.5.4. Rain flow counting on the stress signal is applied and with use of the SN-curve for the bolts the fatigue damage for a specific sea state for the specified simulation time is calculated.

Every sea state is simulated in HAWC 2 with three different seed numbers. The simulations took 10 minutes each and the average fatigue damage value is taken.

3.6.1 Result discussion

Figure 3.5 shows the results of the average fatigue damages of the flanges after the 10 minutes simulations. The sea states with the highest wind speeds yield the highest fatigue values (sea state 1 and 18). The damage values for a simulation time of 10 minutes are recalculated to a 25 year life time and multiplied with their occurrences according Appendix E. Figure 3.6 shows the damages for the different sea states. The sum of the damage values for the different sea states gives the total fatigue damage per flange as can be seen in Table 3.14.

Flange	**BF**	**LMF**	**UMF**	**TF**
25 years damage	1	0.215	0.130	0.016
Expected life	25	116	192	1563

Table 3.14: Total fatigue life of the flanges.

From this table it can be concluded that the maximum fatigue damage occurs at the bottom of the tower. The fatigue damage decreases the higher the flange is located in the tower. This could have been expected, regarding the decreasing moments. Only the bottom flange design is FLS driven, as its damage value is 1. It’s designed so it can just withstand its fatigue lifetime. The other flanges are ULS driven.

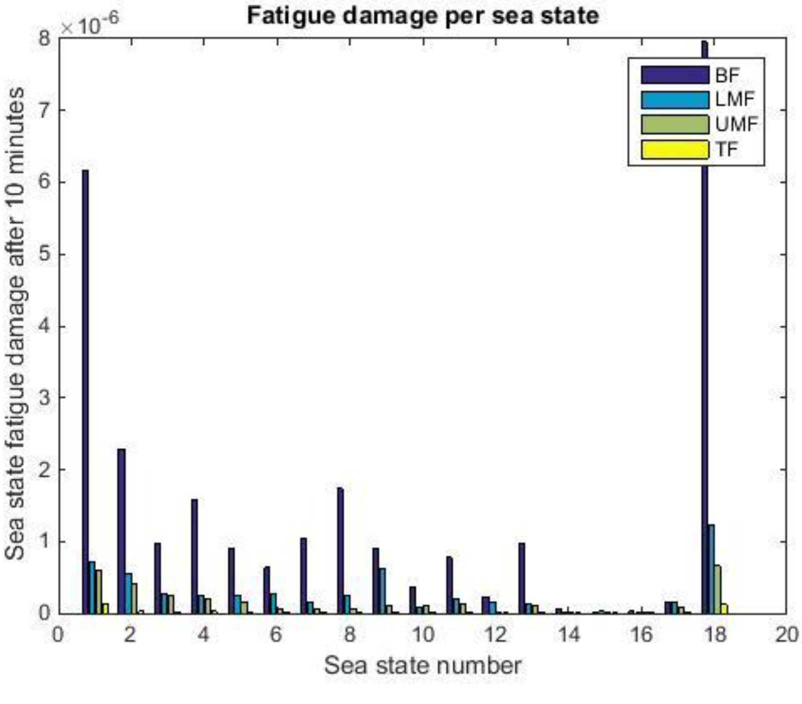

Figure 3.5: Fatigue damage per sea state simulation.

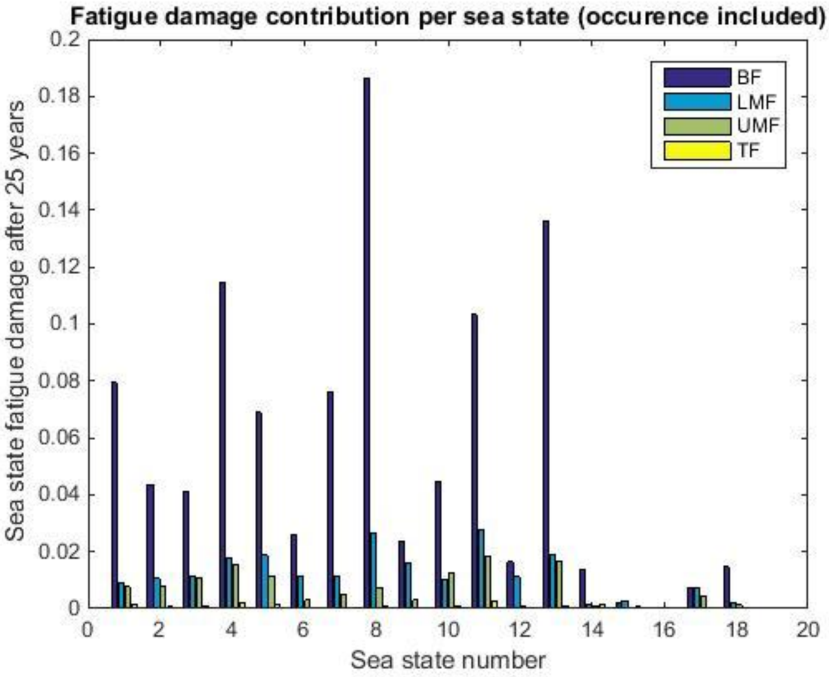

Figure 3.6: Fatigue damage contribution per sea state.

3.7 Flange representation in HAWC2

3.7.1 The considered models

In the current 5MW-NRELT model in HAWC2 the flanges are not modeled in the structural model of the tower. For the 6MW-SWT, modeled in BHawC, the flanges are modeled as an additional lumped mass to represent the flange weight.

This section will analyze if these simplification of representing the flanges are accurate enough. This will be done by analyzing the HAWC2 simulations of the 5MW-NRELT in which:

- the flanges are not modeled at all (as in the current 5MW-NRELT model);
- the flanges are modeled as point masses (as in the current 6MW-SWT model);
- the flanges are modeled with their geometry, mass and flexibility.

In this way it can be analyzed if the simplified models are accurate enough. Table 3.15 gives an overview of the different models which will be run in HAWC2.

	"Tower without flanges" model	**"Tower with flange mass" model**	**"Tower with flange properties" model**
Flange mass		X	X
Flange geometry			X
Flange flexibility			X

Table 3.15: Three different considered models.

3.7.2 Flange modeling

Figure 3.7 gives a representation of how the flange parameters are included in the structural data file of the tower. The points represent nodes in the HAWC2 data file. The red colored nodes represent the nodes at the flange welds. The properties of the tower data file between these nodes are changed in such a way that they represent the flange connection. Figure 3.7 gives an example how the E-modulus is modeled.

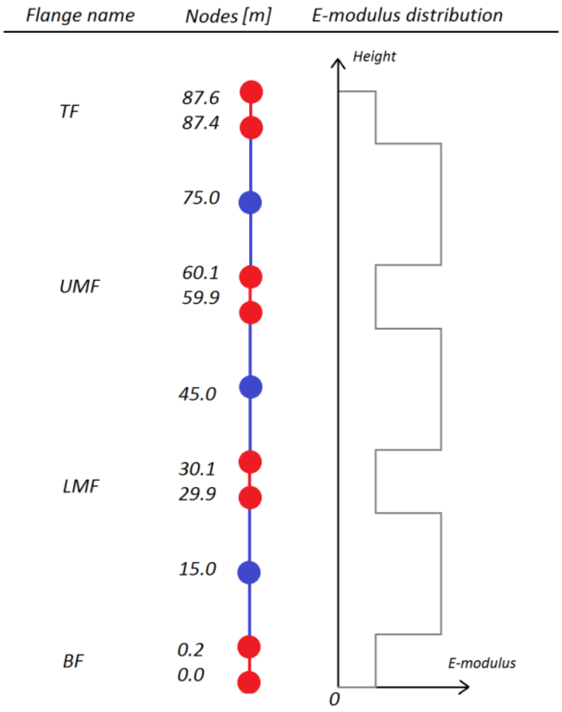

Figure 3.7: Flange model in HAWC2.

Including the mass in the HAWC2 model is quite simple. Point masses are added at the flange locations. Including the flexibility is a bit more complicated. The beam elements in the HAWC2 program are Timoshenko 3D beam elements. The Timoshenko beam theory takes into account shear deformation and rotational inertia effects, making it suitable for describing the behavior of short beams (unlike the ordinary Euler-Bernoulli beam theory).

At the location of the flanges, the distributed mass is increased and the area and polar moments of inertia and radii of gyration are changed to values that correspond with the flange values. To include the flexibility of the flanges, also the elastic modulus (E) and shear modulus (G) values in the tower data file should be adjusted at the flange locations. The flanges should have an elastic modulus that represents the stiffness of the flange. The total number of bolts is multiplied with the stiffness of one bolt connection to get the equivalent stiffness of the whole flange connection.

$$E_{eq} = \frac{1}{\delta_{tot}} \cdot N_{bolts} \qquad \text{Equation 3.2}$$

The stiffness of one bolted connection ($\frac{1}{\delta_{tot}}$) in the four considered flanges can be calculated analytically. The method as described in Appendix A is used. The total resilience is the sum of the bolt and plate resilience.

Including these data in the tower data file will represent the bending stiffness (EI_x and EI_y) and longitudinal stiffness (AE) of the flange. The corresponding equivalent shear modulus (G) is calculated with the simple relation for isotropic linear elastic materials:

$$G = \frac{E}{2\,(1+\upsilon)} \qquad \text{Equation 3.3}$$

The same Poisson ratio as in the tower shells is assumed ($\upsilon = 0.3$).

3.8 Flange influence on dynamical behavior

The load case which yields the highest overturning moment for the bottom flange (DLC 1.4b) will be used as comparison load case. The three different flange models as described in Table 3.15 will be considered.

3.8.1 Eigenfrequencies

The added masses cause a difference in the eigenfrequency in the structure as can be seen in Table 3.16. Only the first two eigenfrequencies are displayed, because these frequencies contain most of the energy. As expected, the increased mass will lower the eigenfrequency ($f_{nat} = \frac{1}{2\pi}\sqrt{\frac{k}{m}}$) . Adding the flexibility of the flanges, lowers the eigenfrequencies even more. The influence is however small.

	Flange mass excl. Flange flex. excl.	**Flange mass incl. Flange flex. excl.**	**Flange mass incl. Flange flex. incl.**
Frequency Nr.	**Frequency [Hz]**	**Difference [%]**	**Difference [%]**
f_1	0.2242	-0.77	-0.81
f_2	0.2265	-0.78	-0.83

Table 3.16: The two first eigenfrequencies.

Appendix I displays the frequencies and mode shapes of the used reference wind turbine in a water depth of 20 m. This table can be used as a comparison. An analysis of the mode shapes in HAWC2 shows that adding the flanges does not influence the mode shapes. The mode shapes are still the same as from the original wind turbine without modelled flanges. The first eigenfrequency represents the frequency of the first mode in fore-aft direction and the second eigenfrequency the frequency of the first mode in side-to side direction. A comparison of the two first eigenfrequencies with the frequencies in reference table in Appendix I shows that they are slightly lower than the reference values for a water depth of 20 m. This is logical since a longer length (simulations in this report are done for a water depth of 25 meter) decreases the first eigenfrequencies [32].

The dependence of the frequency on the flange stiffness is displayed in the Figure 3.8. The first two eigenfrequencies are most important, because most of the excitation energy will be around these two. With a flange stiffness of around 100 GPa, the eigenfrequencies changes are small in comparison with assuming no flange (stiffness steel 210 GPa).

The differences in eigenfrequencies are that low that differences in the fatigue life are not to be expected.

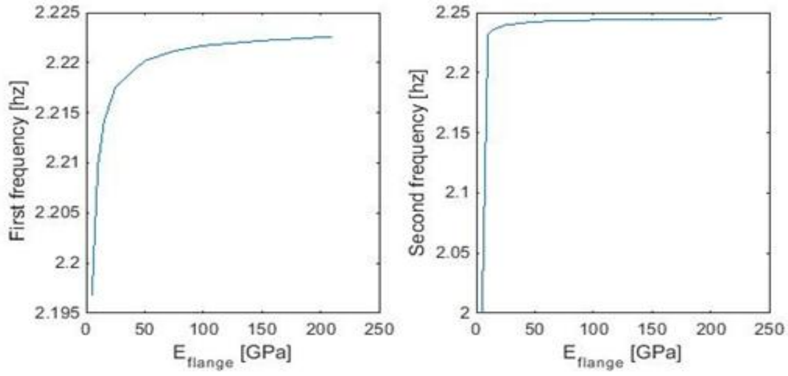

Figure 3.8: Eigenfrequency dependency on flange stiffness.

3.8.2 Deflections

Table 3.17 and Table 3.18 give the parameters of the deflections due to the external moments at the lower middle flange and the top flange.

	Flange mass excl. Flange flex. excl.	**Flange mass incl. Flange flex. excl.**	**Flange mass incl. Flange flex. incl.**
Location	**Deflection mean [m]**	**Difference [%]**	**Difference [%]**
x **LMF**	0.04	-0.5	-0.5
y **LMF**	0.15	-0.7	-0.7
x **TF**	0.14	-1.5	-1.2
y **TF**	0.50	-1.4	-1.2

Table 3.17: Deflections mean values.

	Flange mass excl. Flange flex. excl.	**Flange mass incl. Flange flex. excl.**	**Flange mass incl. Flange flex. incl.**
Location	**Deflection std [m]**	**Difference [%]**	**Difference [%]**
x **LMF**	0.02	-0.9	-0.9
y **LMF**	0.05	-1.7	-1.3
x **TF**	0.07	-1.6	-1.6
y **TF**	0.17	-2.3	-1.9

Table 3.18: Deflections standard deviation values.

It can be concluded that adding the flange masses and flexibilities have little influence on the mean and standard deviation of the deflections of the structure.

3.8.3 Moment differences

Besides the eigenfrequency differences, the difference in the moments at the flange locations are investigated. DLC1.4b, the load case that yields the highest moment, is run again with added masses and flexibility.

	Flange mass excl. Flange flex. excl.	Flange mass incl. Flange flex. excl.	Flange mass incl. Flange flex. incl.
Location	**Moment [MNm]**	**Difference [%]**	**Difference [%]**
M_{max} **BF**	83.6	+0.13	+0.21
M_{max} **LMF**	41.8	+0.41	+0.37
M_{max} **UMF**	18.3	+0.15	+0.23
M_{max} **TF**	12.3	+0.34	+0.26

Table 3.19: Moments standard deviation values.

From above table it can be concluded that including the flange masses and flexibilities have little influence (less than 0.5%) on the occurring moments.

3.8.4 Conclusion

Including the mass of the flanges in the HAWC2 simulations lowers the first two eigenfrequencies of the structure with 0.77% and 0.78%, while including the flexibility as well lowers the eigenfrequencies only with an additional 0.04%. The eigenfrequencies of the structure are almost not influenced by the flanges and the mode shapes remain the same.

The mean of the deflections at the flange locations are less than 1.5% changed in the direction of the unloaded situation. The standard deviations of the deflections decreased with maximal 2.3%. The moments at the flange locations are increased with less than 0.5%.

To conclude, the effect of modeling the tower flange connections (mass, geometry, stiffness) in HAWC2 is small. The effect of geometry and stiffness is not contributing as much as modeling the mass. Modeling the flanges as point masses is therefore sufficient to represent the flanges in the aeroelastic code.

3.9 Damping of flanges

This section will give a short introduction on damping in general and it will explain that the introduction of damping is beneficial for the fatigue life of a wind turbine. A test set-up to determine frictional damping of layered components (a flange) will be discussed. Extra tower damping can be introduced with use of a so called constraint damping layer between the flanges. A suggestion is made what such a layer can look like.

3.9.1 Introduction

All dynamic processes in mechanical systems are more or less damped. Consequently, damping is highly relevant in the fields of technology and applied physics which deal with dynamics and vibrations. Damping in mechanical systems is understood to be the irreversible transition of mechanical energy into other forms of energy as found in time-dependent processes. Damping is mostly associated with the change of mechanical energy into thermal energy. Damping can also be caused by releasing energy into a surrounding medium. Electromagnetic and piezoelectric energy conversion can also give rise to damping if the energy converted is not returned to the mechanical system. Engineering structures require a certain minimum amount of damping for vibration control, particularly if the structure is excited at is natural frequency [59].

The excitation of tower resonance can be minimized by maximizing the damping and ensuring that the natural frequencies are well separated from the exciting frequencies. Phenomenologically the damping in a mechanical system can be composed of the following contributions:

- Material damping by micro-plastic deformation.
- Friction contact-surface damping. Energy dissipation due to micro-slip along frictional interfaces, which provides a beneficial damping mechanism and plays an important role in the vibration behavior of structures [60].

The latter form of damping can be introduced by flanges as explained in the next section.

3.9.2 Damping modeling

Even though the mass and the stiffness distribution of a structure can be modeled within a Finite Element Model (FEM) quite precisely, there is still a lack of suitable damping models. The process of modeling damping matrices and experimental verification of those is challenging because damping cannot be determined via static tests as can mass and stiffness. Furthermore, damping is more difficult to determine from dynamic measurements than natural frequency [61].

For a layered and jointed structural member, the damping ratio, μ, is expressed as the ratio between the loss energy dissipated due to the relative dynamic slip between the interfaces and the total energy introduced into the system and is expressed as [62]:

$$\mu = \frac{En_{loss}}{En_{loss} + En_{unload}} \qquad \text{Equation 3.4}$$

En_{loss} represents the energy loss due to interface friction. En_{unload} is the energy to be introduced during the unloading process [62]. Damping prediction can be done by a study of the micro-slip phenomenon using FEM [60]. This can be done with use of layer elements on the joints' interfaces in the FEM model. The used damping parameters can be found experimentally from a generic isolated joint test bench [63]. To validate the applied models, experiments should be conducted.

3.9.3 Frictional damping for a layered and jointed structural member

It is established that the damping capacity of structures jointed with connecting bolts can be improved substantially by increasing the number of layers connected with bolts of smaller diameters along with use of washers.

A paper by Nanda [62] describes experiments that have been conducted on a number of specimens to study the damping in layered and jointed structures, see Figure 3.9 for the experimental set-up. The results were consistent with the numerical results. Intensity of interface pressure, its distribution characteristics, relative spacing of the connections bolts, dynamic slip ratio, frequency and amplitude of vibration are found to play a vital role in the damping capacity of such layered and jointed structures. The following conclusions are drawn from the experiment depicted in Figure 3.9:

- Damping increases with an increase in the number of layers in a layered and jointed structure due to an increase in the interface friction layers which causes an increase in the energy loss due to interface friction.
- Damping decreases with an increase in initial amplitude of excitation due to introduction of higher energy into the system compared to that of the dissipated energy due the interface friction
- Damping decreases with an increase in tightening torque on the connection bolts owing to higher interface pressures with lower dynamic slip ratio at the interfaces which tent to behave like a solid beam [64].

These results indicate that the introduction of an extra layer between the flanges can increase the damping of flange connections.

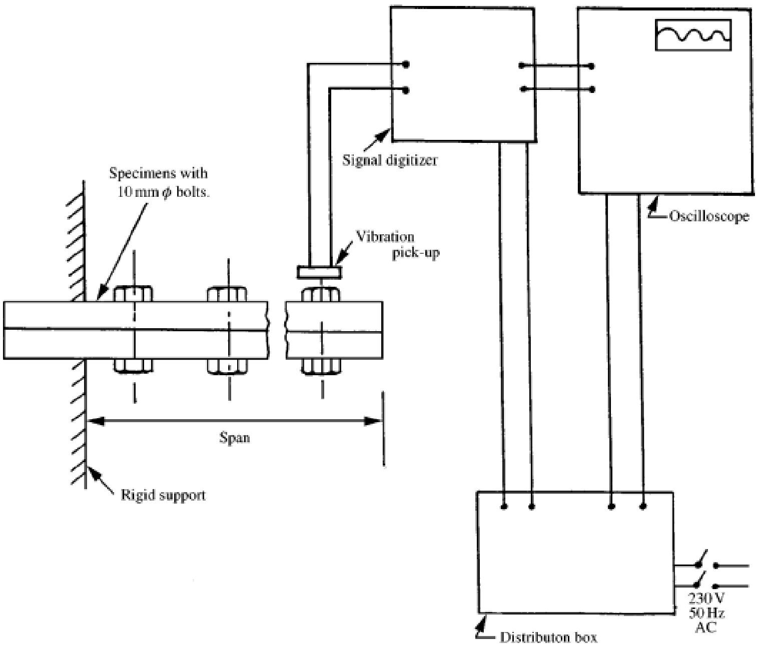

Figure 3.9: Experimental set-up for determining damping in layered structures [62].

3.9.4 Constraint damping layer

A constraint damping layer is a damping treatment that can be applied to increase the structures ability to dissipate mechanical energy. Bringing structures with little internal damping (steel) into intimate contact with a highly damped, dynamically stiff material, such a constraint damping layer can be realized, see Figure 3.10. Of the common damping materials in use, many are viscoelastic; that is, they are capable of storing strain energy when deformed, while dissipating a portion of this energy through hysteresis.

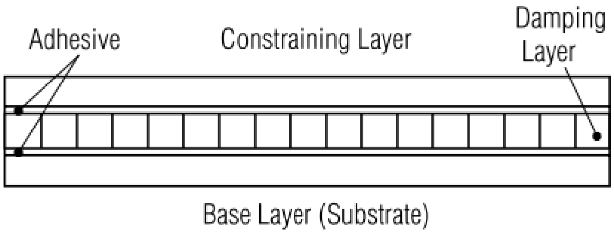

Figure 3.10: Constraint damping layer [65].

Constrained layer damping systems are usually used for very stiff structures. A “sandwich” is formed by laminating the base layer to the damping layer and adding a third constraining layer. When the system flexed during vibrations, shear strains develop in the damping layer. Energy is lost through shear deformation, rather than extension of the material.

3.9.5 Investigation of a constraint damping between flanges

This section tries to explain how a constraint damping layer can be applied within flange connections.

First of all, it should be noted that the introduction of a damping layer on the complete surface between the two flange plates will increase the bolt share of load dramatically, see Figure 3.11. This is caused by the fact that the soft damping layer increases the relative stiffness of the bolt in comparison with the layered components (flanges and damping layer); see Section 2.3.5.2 for the calculations.

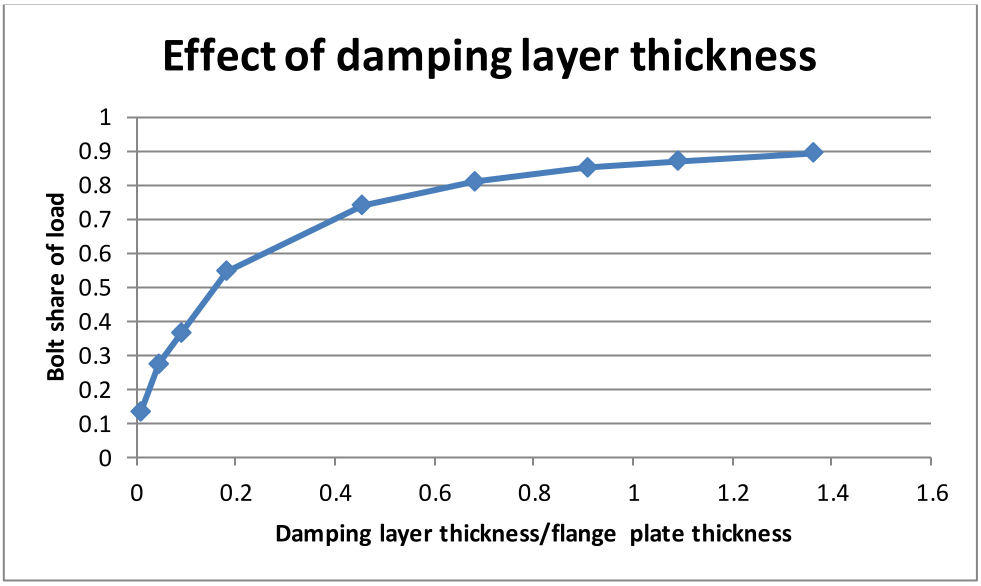

Figure 3.11: Effect of damping layer on the bolt share of load.

Increasing the bolt share of load will decrease the fatigue life of the bolt connection. This is undesired, especially for the bottom flange which design is often fatigue driven. Therefore the damping layer should not take the static but only the dynamic loads.

To prevent the damping layer taking the static loads, the layer should only partly been laid between the flanges, see Figure 3.12 b. However, with the introduction of such a layer the flange failure modes (Section 2.3.5) might not be valid anymore. Furthermore, the function between the shell stress and bolt stress (Figure 2.26) will change as well. Another aspect that should be considered is the costs. The introduction of a partly laid damping layer will increase the flange costs due to the production of an extra layer and extra machining of the flange.

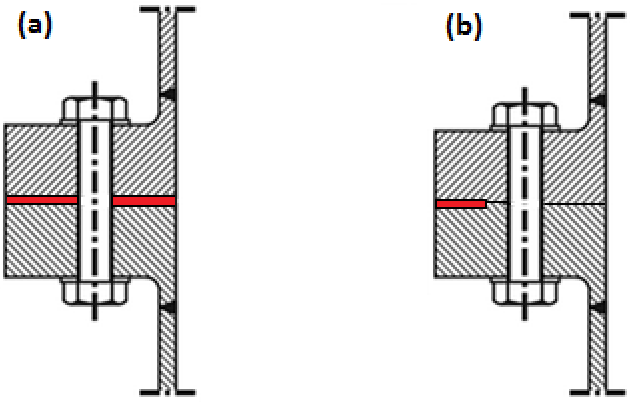

Figure 3.12: Damping layer on complete surface (a) and a partly damping layer (b) [45].

The success of such a layer is dependent on the material choice, pre-stress of the bolts and shape of the material layer. Constrained damping layers are usually made from highly viscoelastic polymers or fiber composites. A layer with a tapered thickness can also be considered. By playing with the different variables, a constraint damping layer can be designed which maximizes the tower damping. Figure 3.12b shows a layer on the inner side of the flange connection. In this way the layer will not be exposed to weather influences. Having the layer on the outer side of the flange connection will however realize more damping. A damping layer on the outside is further away from the centerline of the wind turbine and hence the displacement of the flanges due to bending is slightly higher. However the difference will be small since the flange width is relatively small in comparison with the radius. A layer on both sides is possible as well; however the surface of the connected plates without layer should not become too small in order to ensure that the bolt share of load stays low and hence the bolt fatigue damage.

The ideal material for the damping layer must provide efficient energy dissipation under compression. Besides the material damping, it should introduce energy dissipation due to micro-slip along the frictional interfaces. With use of FEM models and experiments, the influence the flange constraint damping layer can be investigated.

Chapter 4

4 Improvements in flange design

Tower flange connections serve to connect the individual tower sections (typically 2 or 3), as well as the tower to the offshore transition piece and the nacelle. Currently at SWP, these flanges are custom designed for each tower design. While this approach leads to an optimal tower structural design, it also requires that tower internals and handling equipment have to be custom designed.

Firstly, in Section 4.1 the SWP flange design method will be explained. Then Section 4.2 will discuss the proposed improvements in this method. The relevance of standardization will be explained in Section 4.3. A standardization procedure will be proposed and explained in Section 4.4. The benefits and costs of this standardization procedure are listed in Section 4.5. Section 4.6 and 4.7 explain the influence of standardization on the tower design and the influence of the transportation load case on the flange design. An alternative of standardization is given in Section 4.8. Finally, conclusions will be drawn in Section 4.9.

4.1 Flange design optimization method within SWP

4.1.1 Design criteria

Within SWP, the flanges are designed according the criteria below [1].

1. Loads on the flange should stay lower than the ULS critical failure mode (Section 2.3.5).
2. The fatigue damage of a single bolt should stay lower than 1 (Section 2.3.5).
3. The width of the flange should be large enough to accommodate the maximum deformation cone (Section 2.3.5).
4. The stress cones of the single bolt connections should overlap in order to prevent joint opening between adjacent bolts (see Section 2.3.5).
5. Bolts in a flange connection should not rupture in case four bolts are evenly removed around the circumference.
6. The width of the flange should be large enough to attach tower internals.

7. The bolt length should be large enough to clamp the two flange plates together and accommodate the minimum clamp length belonging to the used bolts.
8. Plastic deformation should not occur during horizontal transport.

The last load case will be explained in more detail in Section 4.7, because this load case is often governing for the flange width. Improvements in transport are proposed in order to reduce these loads, see Section 4.7.

4.1.2 Flange parameters

The flange parameters in general are already described in Section 2.3.5. The specific details for the flanges used in the 6MW-SWT will be discussed in this section. The bottom flange, lower middle flange and upper middle flange are designed tower specifically. The top flange at SWP is turbine specific, i.e. the same top flange is used for all the turbines of a specific turbine type (6MW-SWT for example). The top flange will not be considered in the optimization and standardization procedures, because it's already standardized. Most of the new installed 6MW-SWTs are made out of three tower sections. The lower two sections are cylindrical, while the top section has a conical shape, see Figure 2.15.

At SWP the flange connections for onshore and offshore towers are designed with a standardized outer diameter. With this design philosophy, the outer diameters of the tower sections are fixed, because they are equal to the flange outer diameter. The inner diameters of the tower shells depend on the outer diameter and the used wall thickness. The bolt diameters for the newest offshore wind turbines (3-6 MW) are typically M42 or M48. The flanges are made of S355 steel. The fixed outer diameter of the shell and the variable wall thickness and bolt types will cause the bolt circle diameter to vary.

For bolt calculations, the flange is divided in as many segments as bolts in one flange. These single bolt connections should be able to resist the ULS and FLS loads. The lengths of the bolt extenders are dimensioned to accommodate the min- and maximum clamp lengths of the bolts.

4.1.3 SWP optimization method

The feasibility of a flange design is checked with the criteria as listed in Section 4.1.1. The program Matlab is used in order to design the optimized and standardized flanges. The function 'fminsearchbnd' is applied to find the flange design with the lowest performance function; a multivariable function that represents the flange costs or flange mass. The function 'fminsearchbnd' is a 'fminsearch' function that constraints the variables with a lower and upper bound. The 'fminsearch' function finds a minimum of a multivariable function using a derivative free method [66].

In the current flange design method of SWP, the performance of the design is expressed with use of a mass performance function (MPF) which makes use of the flange thickness and width, as stated in Equation 4.1.

$$MPF = t_f * w_f \qquad \text{Equation 4.1}$$

The design with the lowest MPF value will be most mass efficient, since the lowest amount of steel has to be used to manufacture the flange. If the flange design doesn't meet one of the criteria listed above, a high penalty value will be added to the MPF, in order to let the optimization tool not choose this design. The optimization tool first considers a flange design with the maximum amount of bolts. Then it will subtract four bolts of the design and analyses if this design still fulfills the criteria. The optimization tool selects feasible design cases with a certain performance function value and number of bolts. A low number of bolts is beneficial because it will reduce the bolt purchase costs, flange production costs and the installation time. With use of the Pareto criterion, the optimum design cases are chosen. A way of describing Pareto optimality is to describe any state as Pareto optimal when no Pareto improvement is possible. This effectively means that it is impossible to improve the condition of any single individual (less bolts or a lower MPF value) without harming the condition of another individual (more bolts or a higher MPF value). If multiple designs persist (multiple Pareto optimum points, see Figure 4.1), currently at SWP the design with the lowest amount of bolts will be chosen.

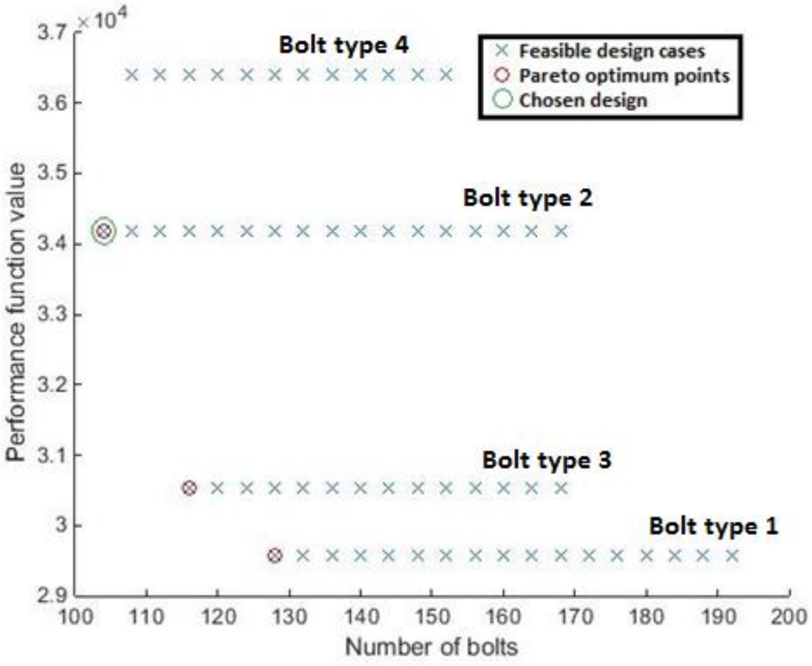

Figure 4.1: Feasible design cases for an example project [1].

Figure 4.1 shows four lines of feasible flange designs. They represent the design cases with bolt type 1 till 4, see Table 4.1. The two lines with the highest performance function represent the longer bolts (M42-320, M48-380), because they require a higher minimal flange thickness in order to realize the minimal clamp length. The two lower line are the shorter version bolts (M42X280, M48X330), requiring a lower minimal flange thickness, causing a lower performance function.

Bolt type (BT)	**Bolt**	**Bolt length**	**Number of bolts (NB)**	**Flange width (w_f)**	**Min flange thickness due to clamp requirement**	**Flange thickness (t_f)**	**Flange width*Flange thickness**
1	**M42**	280 mm	128	394	65	75	29550
2	**M42**	320 mm	108	346	85	105	36330
3	**M48**	330 mm	116	385	72	79	30415
4	**M48**	380 mm	104	352	97	97	34144

Table 4.1: Optimum flange design for different bolt types.

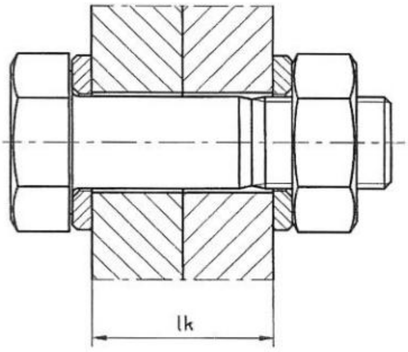

Figure 4.2: Clamp length [50].

The flange thickness is often governed by the minimum bolt clamp length or the flange failure modes, defined by Petersen and Seidel (Section 2.3.5). The width however, is often determined by the transport load case. A reduction of the forces during horizontal transport will therefore result in lighter flange designs. Section 4.7 wil desribe proposals how this can be realized. Section 4.2 will describe improvements that can be made in the above mentioned design method used nowadays within SWP to realize a more cost efficient flange design.

4.1.4 SWP reference projects

With use of 30 past 6MW-SWT projects improvements in flange design will be proposed. The tower designs of these projects will be used as reference material for both proposing an improved flange optimization procedure and proposing the flange standardization cases. The considered projects are all located in European waters with a water depth varying from 15 up to 40 m. Figure 4.3 till Figure 4.7 depict the geometrical values of the flanges designed following the SWP design method.

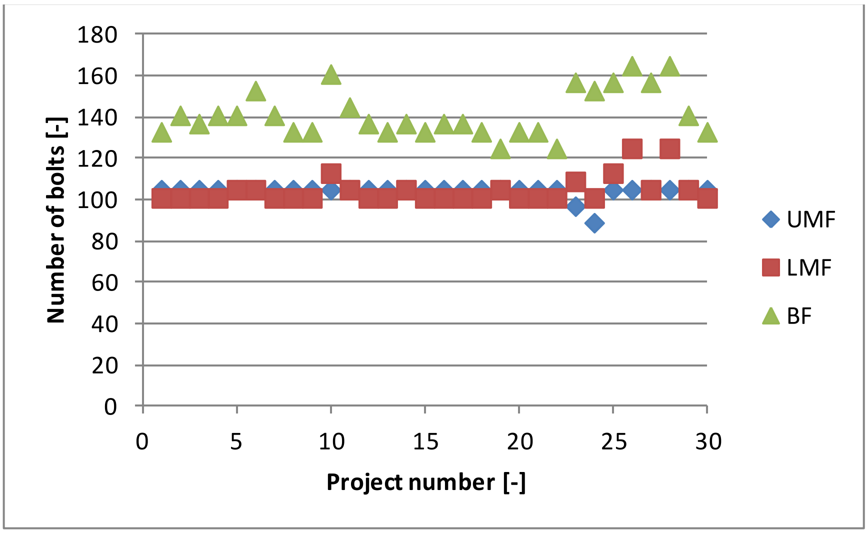

Figure 4.3: Number of bolts.

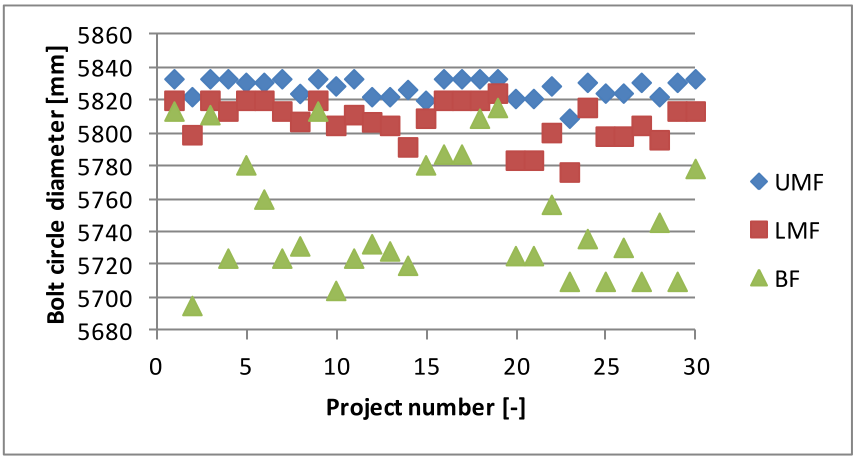

Figure 4.4: Bolt circle diameter.

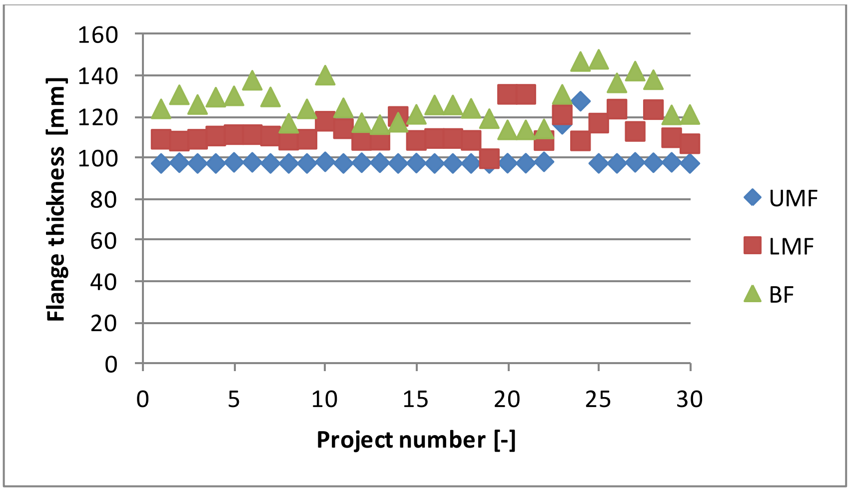

Figure 4.5: Flange thickness.

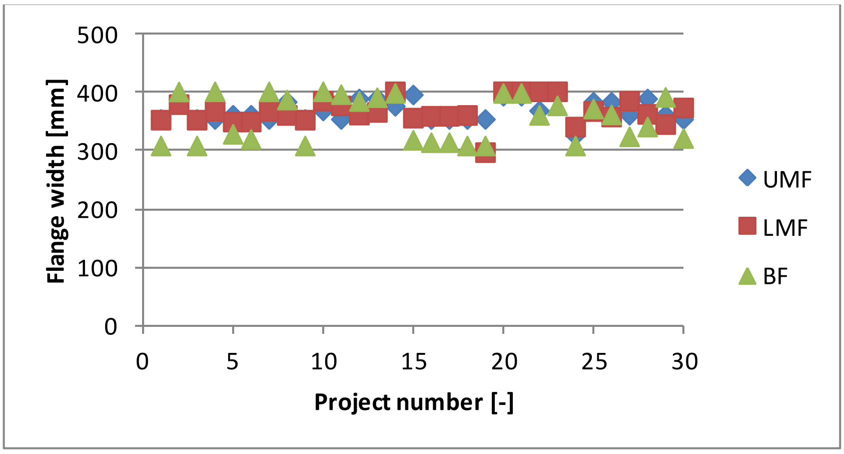

Figure 4.6: Flange widths.

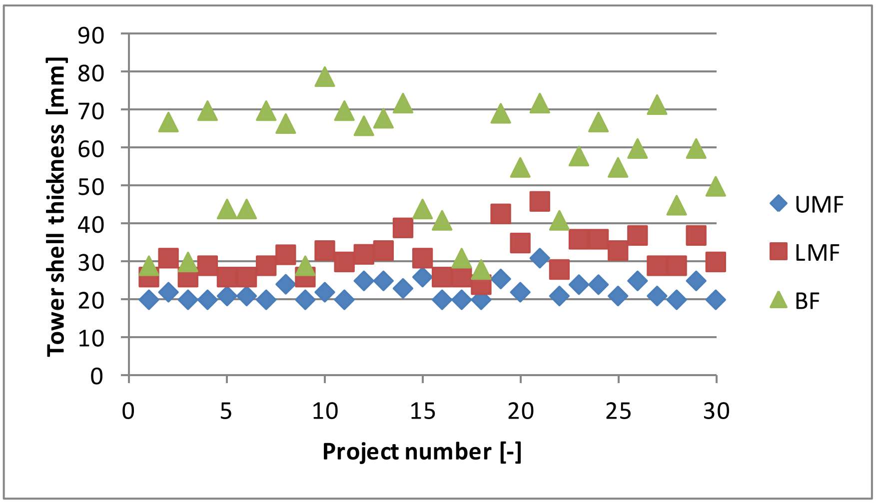

Figure 4.7: Tower shell thicknesses.

4.2 Flange design optimization

4.2.1 Extra optimization to allow for lower amount of bolts

The first proposed improvement is related to the optimization procedure. As stated above, in the current design optimization the flange geometry is optimized for the flange design with the maximum number of bolts in a flange. Subsequently four bolts are subtracted and the flange design is checked again if it's still feasible. However, not another optimization procedure is performed with this lower number of bolts. In the improved method again an optimization is performed to allow for a flange with a lower number of bolts that is still feasible due to a larger width and/or thickness of the flange.

4.2.2 Cost optimization model

The second proposed improvement is related to the performance function. As explained in the previous section, currently the bolt type is chosen which realizes a design with the lowest amount of bolts. This means that for example a heavy design can be chosen over a very light design, only because this design has four bolts less. This might not be the most cost efficient design. To overcome this problem, the mass and number of bolts should be given a weight factor in order to indicate their importance. This weight factor can be expressed in terms of costs. In this way a cost optimization function can be made. Minimizing the cost optimization performance function will give the most cost optimal design. In order to get a cost optimized performance function, factors that influences the costs of a flange connection should be identified, see Table 4.2. The costs of flange raw material are dependent on the flange raw material mass, while the other costs are related to the number of bolts.

Factors of influence for total flange costs	Abbreviation
Flange raw material outer diameter	$d_{out,rm}$
Flange raw material inner diameter	$d_{in,rm}$
Flange raw material height	$t_{f,rm}$
Number of bolts	NB
Cost factors	$F1 - F6$

Table 4.2: Factors of influence flange costs.

The cost performance function (CPF) is stated in Equation 4.2. These costs are divided in costs relating to the flange raw material (C_{RM}) and costs related to the number of bolts (C_{NB}).

$$CPF = C_{RM} + C_{NB} \qquad \text{Equation 4.2}$$

$$C_{RM} = F1 + \rho \cdot \pi \cdot \frac{1}{4}\left({d_{out,RM}}^2 - {d_{in,RM}}^2\right) \cdot \ t_{f,RM} \cdot \ (F2 + F3) \qquad \text{Equation 4.3}$$

$$C_{NB} = NB \cdot (F4 + F5 + F6) \qquad \text{Equation 4.4}$$

The outer diameter, inner diameter and thickness are the geometrical values of the raw material needed to manufacture the flange, see Appendix H. The density ρ of steel is 7850 kg/m^3. The values of the cost factors $F1 - F6$ are dependent from external suppliers and therefore prone to changes. The next section will give a best estimate.

4.2.2.1 Cost factors SWP

At SWP, the estimated cost price of the flange raw material is set on €1/kg. Machining the raw material is estimated on €1.10/kg, including drilling holes. To give a costs indication: for an average lower middle flange (d_{out} =6000 mm, d_{in}=5280 mm, t_f=110mm) the total flange manufacturing costs are €24.000.

4.2.2.2 Improved cost factors

In reality a flange that is twice as heavy doesn't cost twice as much. Therefore, a base price will be introduced to get a more realistic cost model. This base price is set on 25 % of the total average flange costs, €6000. The other €18.000 can be divided by costs due to drilling the holes (5€ per hole) and costs due to purchase of the raw material (€1/kg) and machining the flange (€0.50/kg).

The estimated prices for the different bolts are the averaged prices from four different suppliers. The extender prices are deduced from the external dimensions of the extender and estimated on 1€/kg, including machining. This means a price of €3 and €6 for the extenders for the M42 and M48 bolts respectively, see Appendix H. Table 4.3 shows an overview of an estimation of the cost factors.

Abbreviation	Explanation	Estimated price
F1	Base price for a flange	€6000
F2	Costs of raw flange material	€1/kg
F3	Costs of machining raw material	€0.50/kg
F4	Costs of bolts	M42X280: €12.9/bolt assembly M42X320: €14.4/bolt assembly M48X330: €18.8/bolt assembly M48X380: €20.8/bolt assembly
F5	Costs of extenders	80mm: €3/extender 110mm:€6/extender
F6	Costs of drilling bolt holes	€5/bolt hole

Table 4.3: Cost factors.

Besides the purchase and manufacturing costs, the number of bolts also influences the installation and service time of one wind turbine. However, these costs will not be included in the analysis;

otherwise the scope of this research will become too large. Furthermore, the installation and service costs are quite hard to quantify. Spending a bit more time on installation and maintenance because of a higher number of bolts doesn't always directly result in higher costs. The maintenance and service boats are rented for large periods of time, to compensate for weather down time and uncertainties. Besides that, the middle flanges are sometimes already connected with each other on the quay side.

4.2.3 Cost optimization results

As explained, the flanges designed within SWP are optimized with use of a Pareto optimization between the number of bolts and mass performance function as stated in Equation 4.1, while the improve optimization uses Equation 4.2. New flange designs will be made for the 30 considered 6MW-SWT projects (Section 4.1.4) according the improved optimization method. The results will be compared with the flange designs according the normal SWP method. The parameters stated in Table 4.4 are fixed for the flanges at all the flange locations and are independent of the optimization method.

d_{out} $[mm]$	6000
BT $[-]$	Variable
t_{sh} $[mm]$	Project dependent
d_{bc} $[mm]$	Variable

Table 4.4: Independent parameters different optimization cases.

The average optimized flange masses (flange nose and bolt holes not taken into account) for the SWP and the proposed cost optimization are listed in Table 4.5 .

	SWP optimization case	Improved optimization case
UMF mass $[kg]$	5042	4423 (-12%)
LMF mass $[kg]$	5723	5106 (+11%)
BF mass $[kg]$	6219	5768 (-7%)

Table 4.5: Flange masses different optimization cases.

The cost optimization method yields flanges with a lower mass than the current method used within SWP. This is however not due to the fact of the extra optimization (Section 4.2.1), but because of the use of a different performance function. Instead of picking a feasible design with the lowest amount of bolts (often resulting in the longer bolt type 4 bolts (see Table 4.1 for the different bolt types)), the most cost efficient design is chosen (often resulting in shorter bolt type 3 and bolt type 2 bolts, see Figure 4.8). Because of these shorter bolts, a lower minimum clamp length is required, resulting in lower minimum flange thicknesses.

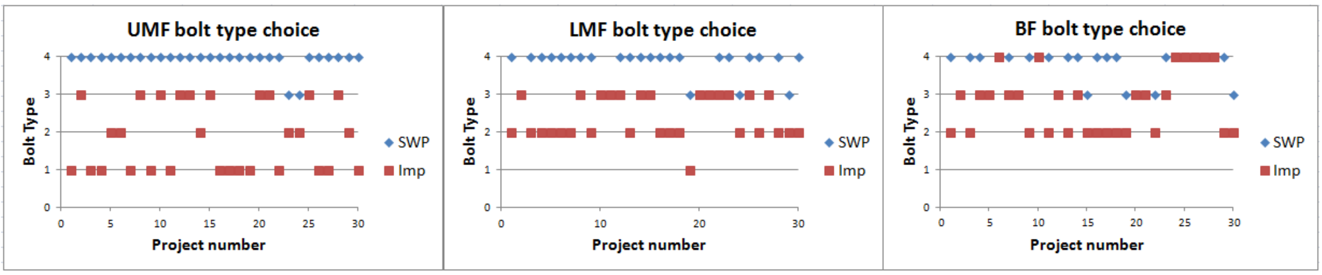

Figure 4.8: Bolt type choice for the SWP and improved optimization cases.

The flange costs calculated for the two different optimization cases are listed in Table 4.6.

	SWP optimization case	Improved optimization case
UMF costs [€]	26 023	25 102 (-3.4%)
LMF costs [€]	27 167	26 341 (-3.0%)
BF costs [€]	29 081	28 563 (-1.8%)

Table 4.6: Flange costs different optimization cases.

These costs consist of one flange ring including all the bolts. The costs for the total flange connection can be calculated by multiplying above mentioned costs by two and subtracting the costs for the bolts, otherwise the costs of the bolts will be included twice. The bottom flange has only one flange ring, which is connected to the transition piece. The costs of the total flange connections are listed in Table 4.7.

	SWP optimization case	Improved optimization case
UMF connection costs [€]	48 776	47 347
LMF connection costs [€]	51 101	49 678
BF connection costs [€]	24 697	24 421
Total costs UMF, LMF, BF [€]	124 574	121 446 (-2.5%)

Table 4.7: Average flange connection costs.

It can be concluded that flanges designed following the improved optimization case are more mass and cost efficient than those designed by the current SWP method.

4.3 Relevance of standardization

As an alternative to custom designed flanges, the use of standardized flanges will be considered in this part of the report. Such standardized tower flanges could be attractive to reduce transport and installation costs, furthermore supply chain benefits could be exploited for further cost reduction, because the flanges can be sourced in larger numbers. The next sections will describe the effects of standardization on different aspects of the supply chain.

4.3.1 Handling equipment

Handling in general is referred to various operations related with a component and is in general divided into four specific operations: lifting, transport, storage and installation. The lifting of a component is referred to lifting operation performed on a component using lifting equipment, e.g.: load and unload prior to transport, installation using a crane, etc. During transport the component is supported by additional structure/equipment and subject to inertia loads from masses due to movements (accelerations) of vehicle and or vessel. For storage of components on harbor and/or on site, the support structure must ensure stability from permanent-, live- and environmental loads. Installation equipment refers to all types of temporary or secondary equipment such as guiding cones, temporary bumpers that are calculated in accordance with lifting, transport or storage calculation procedure. All these types of handling equipment have interfaces with the flanges and standardizing the flanges can lead to standardization of the handling equipment as well.

Figure 4.9: Sea transport of towers [1].

Figure 4.10: Tower transport frame [1].

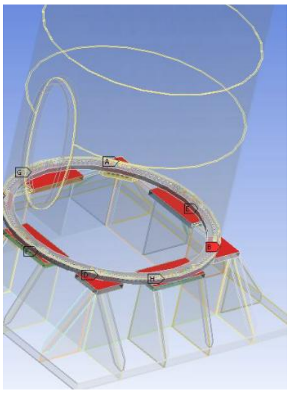

Figure 4.11: Tower adapter plates on transport frame [1].

The tower sections of the 6MW-SWTs are designed specifically for each project; hence dimensions and weights vary. A complete tower consists of 2-3 tower sections each with different flange geometry etc. Handling and lifting of tower sections must be considered from fabrication site to installation site and all operations in-between. The tower sections are transported onshore in horizontal position and in some special offshore cases in vertical position.

The on and off loading of tower sections for onshore transport are conducted by use of special designed lifting equipment such as “T-hook” and “J-hook”. By use of “J-hook” and or “T-hook” at the tower flanges the tower sections are handled horizontal. By use of T-hook at the bottom flange and the lifting brackets at the top end of the tower the sections are upended from horizontal to vertical. The tower bracket is usually designed for the horizontal lift, upending and vertical lift, see Figure 4.12 [1].

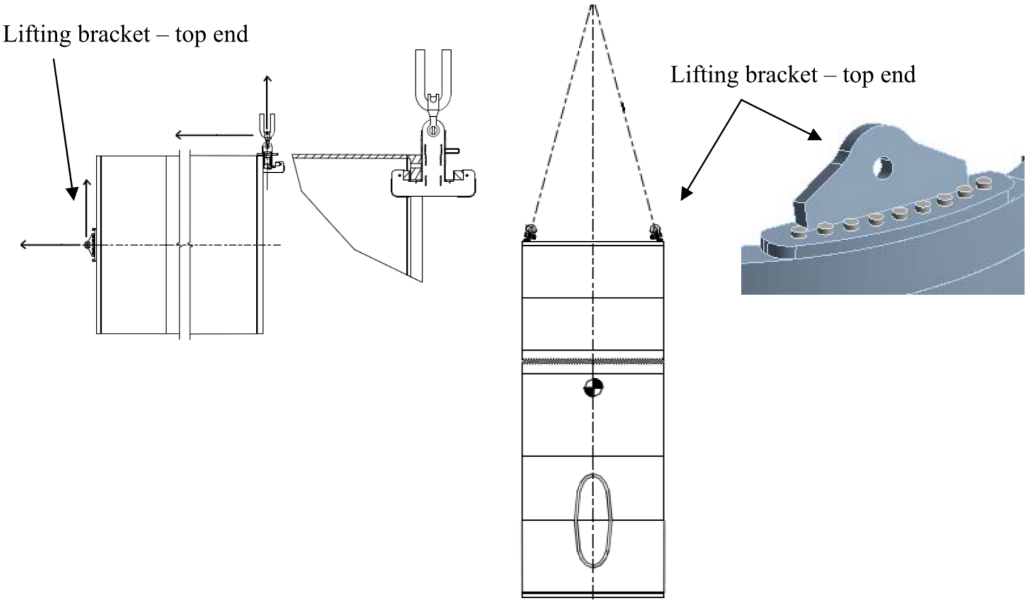

Figure 4.12: T-hook (left) and tower lifting bracket (right) [1].

Handling, lifting, transportation and sea fastening tools (Figure 4.9-Figure 4.12) have interactions with the flange in order to handle the tower section. These pieces of equipment are in general designed for a certain bolt pattern. Changing this pattern means that new equipment has to be designed and certified, resulting in high equipment costs. Besides this financial impact, a variation of equipment tools also enlarges the risk of damage of the tower sections, because different procedures have to be followed and the chance on a mistake is higher.

4.3.2 Tower internals

Flanges have many interfaces with other elements of a wind turbine. Flange design influences tower internals e.g. ladders, platforms and power units. Especially the inner diameter of the flange is of importance for these internals. Standardizing this parameter can lead to a standardized design of tower internals, with costs reductions as a result.

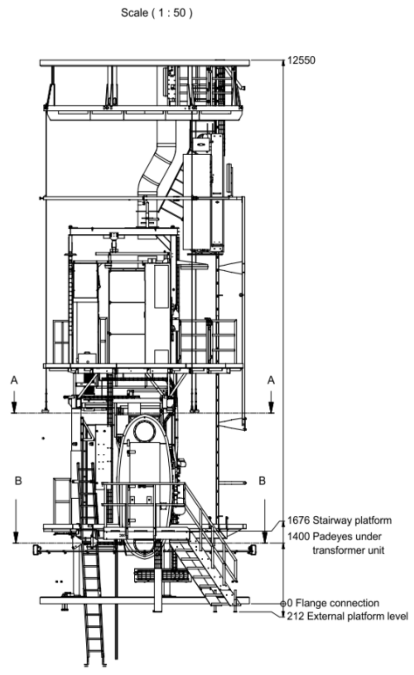

Figure 4.13: Drawing of tower internals [1].

4.3.3 Risk

A risk assessment must be made for the design of custom made equipment and lifting instructions. A risk management plan helps identify potential risks before they occur and prepares for a quick response if they do occur. A well thought-out and proactive risk management plan assist to:

- Reduce the likelihood that a risk factor will actually occur;
- Reduce the magnitude of loss if a risk occurs;
- Indentify the consequences of a risk.

Standardization of components in general will contribute to reduction of the risks. Standardization of the handling procedures will lead to a higher safety of the personnel.

4.3.4 Supply chain

Standardization is beneficial for the stock inventory, because less different flanges and tower internals have to be in stock. Besides that the procurement and logistics will be easier with less different components. Furthermore, the quality control of a standardized component is easier.

4.4 Proposal of standardization

Section 4.1.4 shows the variation of the geometrical values of the different flange designs of the 30 6MW-SWT reference projects. The variation of these geometrical values is not beneficial for many reasons, as explained in Section 4.3. Standardization could be desired. However, standardizing will cause the flange design to be less optimal. This section will investigate how much "less optimal" the standardized flanges will be in comparison with the optimized case.

The "optimized standardization procedure" will be done with use of the 30 6MW-SWT reference projects described in Section 4.1.4. For these projects, flanges will be designed according three different standardization cases (StaCa1, StaCa2 and StaCa3). The masses and costs of the standardized flanges will be compared with the optimized flanges designed according the improved optimization method (Imp. Opt.) as explained in Section 4.2. Table 4.8 gives an overview of the flange parameters which will be standardized and kept variable. The following sections will discuss the standardization cases.

Parameter	Imp. Opt.	StaCa1	StaCa2	Staca3
OD $[mm]$	Fixed	Variable	Variable	Variable
BCD $[mm]$	Variable	Fixed (avg)	Fixed (avg)	Fixed (avg)
WF $[mm]$	Variable	Variable	Fixed (max)	Fixed (avg)
TF $[mm]$	Variable	Variable	Variable	Variable
TS $[mm]$	Variable	Variable	Variable	Variable
NB $[-]$	Variable	Fixed (max)	Fixed (max)	Fixed (avg)
BT $[-]$	Variable	Fixed	Fixed	Fixed

Table 4.8: Flange design parameters.

4.4.1 Standardization case 1

In standardization case 1, the effects of standardizing the bolt circle diameter and the spacing of the bolts will be investigated. This means that per flange location (bottom, lower middle, or upper middle flange) the bolt circle diameter and number of bolts will be fixed. As standardized value for the bolt circle diameter, per flange location the average value of the considered projects will be taken. For the number of the bolts, the maximum amount per flange location is chosen.

	BF	LMF	UMF
$d_{bc}\ [mm]$	5750	5810	5830
$d_{out}\,[mm]$	Variable		
$NB\ [-]$	164	132	104
$BT\ [-]$	3 or 4		
$w_f\ [mm]$	Variable		

Table 4.9: Independent parameters standardization case 1.

4.4.2 Standardization case 2

Besides the standardized parameters as mentioned in case 1, in standardization case 2 the width of the flange will be standardized as well. The maximum value of the considered projects will be taken.

	BF	LMF	UMF
$d_{bc}\ [mm]$	5750	5810	5830
$d_{out}[mm]$	Variable		
$NB\ [-]$	164	132	104
$BT\ [-]$	3 or 4		
$w_f\ [mm]$	400		

Table 4.10: Independent parameters standardization case 2.

4.4.3 Standardization case 3

In standardization case 3, instead of the maximum width, the average flange width of the reference projects will be taken as standardized value. The standardized number of bolts will equal the average value. For standardization case 3, the standardized values for the number of bolts and flange width will in some projects be lower than the one of the optimized reference case. This means that the flange will fail if the other dimensions remain the same. The optimization program will choose a feasible design, if possible.

	BF	LMF	UMF
$d_{bc}\ [mm]$	5750	5810	5830
$d_{out}[mm]$	Variable		
$NB\ [-]$	164	132	104
$BT\ [-]$	3 or 4		
$w_f\ [mm]$	353	359	371

Table 4.11: Independent parameters standardization case 3.

4.5 Comparison of design cases

For the 30 6MW-SWT projects flange designs are made according the above mentioned standardization methods. This chapter will compare the mass and costs of these standardization cases with the values obtained under the improved optimization.

4.5.1 Mass

The average optimized flange masses (flange nose and bolt holes not taken into account) for the different design cases are listed in Table 4.12.

	Imp. Opt.	StaCa1	StaCa2	StaCa3
UMF mass $[kg]$	4423	4957	5296	5283
LMF mass $[kg]$	5106	5411	5723	-
BF mass $[kg]$	5768	6189	7003	-

Table 4.12: Average flange ring masses for the different flange design cases.

A flange design with standardization case 3 was not always possible because the width and/or number of bolts of the flange, which were standardized on the average values, were in some projects (in case of the lower middle and bottom flange) not sufficient enough to realize a feasible design. This standardization case is therefore not suitable for these flange connections.

	Imp. Opt.	StaCa1	StaCa2	StaCa3
UMF connection mass $[kg]$	8 846	9 914 (+12.1%)	10 592 (+19.8%)	10 566 (+19.5%)
LMF connection mass $[kg]$	10 212	10 822 (+6.0%)	11 446 (+12.1%)	-
BF connection mass $[kg]$	11 536	12 378 (+7.3%)	14 006 (+21.4%)	-
Total mass UMF, LMF, BF $[kg]$	30 594	33 114 (+8.2%)	36 044 (+17.8%)	-

Table 4.13: Average flange connection mass (two flange rings including bolts).

The mass differences when standardizing are listed in Table 4.13. Standardizing the bolt circle diameter, number of bolts and bolt type (standardization case 1) results in flanges which are up to 12.1% heavier. Additionally standardizing the flange width in the maximum width results in flanges which have up to 21.4% more mass (standardization case 2).

4.5.2 Costs

The flange costs calculated for the different flange design cases are listed in Table 4.14. These costs consist of one flange ring with all the number of bolts.

	Imp. Opt.	StaCa1	StaCa2	StaCa3
UMF costs [€]	25 102	25 753 (+2.6%)	26 713 (+6.4%)	26 334 (+4.9%)
LMF costs [€]	26 341	27 455 (+4.2%)	28 317 (+7.5%)	-
BF costs [€]	28 563	29 560 (+3.5%)	31 594 (+10.6%)	-

Table 4.14: Average flange costs of one flange ring including bolts.

Standardizing the bolt circle diameter, number of bolts and bolt type (standardization case 1) results in flanges which are up to 4.2 % more expensive. Additionally standardizing the flange width in the maximum width results in flanges which are up to 10.6 % more expensive (standardization case 2).

The total costs of flange connections within one wind turbine can now be calculated for the different design cases. A single wind turbine has one bottom flange ring, which is connected to the transition piece. The lower and middle flange connections consist both of two flange rings, which are bolted together. It should be noted that the prices of one middle flange connection cannot be calculated by multiplying the costs listed in Table 4.14 by two, because then the costs of the bolts are calculated twice. The average costs of the bolts of one flange connection should be subtracted.

	Imp. Opt.	StaCa1	StaCa2	StaCa3
UMF connection costs [€]	47 347	48 408	50 327	49 563
LMF connection costs [€]	49 678	50 950	52 682	-
BF connection costs [€]	28 563	29 560	31 594	-
Total costs UMF, LMF, BF [€]	125 588	128 917 (+2.7%)	134 604 (+7.2%)	-

Table 4.15: Average flange connection costs (two flange rings including bolts).

Standardization case 3 will not be investigated anymore, because it's not suitable for the lower middle flange and bottom flange. It could be an option to design only the upper middle flange according case 3, but due to the small cost difference with case 2, case 3 will be disregarded. Besides that, it's better all the flanges to have the same flange width, because of internals and handling equipment standardization reasons.

4.6 Knock on effects

A fixed outer diameter instead of a fixed bolt circle diameter influences the geometric properties of the tower shell. The values chosen for the standardized bolt circle diameters are the averaged value of the 30 6MW-SWT reference projects, see Section 4.4.2. If the wall thickness is lower than the average value, the outer diameter will be smaller than 6 m. This means that the original tower shell might not be able to meet all the tower shell requirements anymore and have to be designed thicker. However, this effect will be equaled out by the tower shells which could be designed less conservative because of outer diameter which will be a bit larger than 6 m.

4.7 Influence of transport load case

Typically the tower sections are transported by road, train or boat. There exists a plethora of transport equipment solutions; it does not seem realistic to design to all these cases. At SWP, for a start it is opted to look at the simple load case in which a tower section is lying statically on its side, supported only along a single line. The maximum stress for the load case can be found at the point where the line supports the tower.

A second load case that is investigated is when the tower section is lying on its side merely supported underneath its two flanges. The accelerations by ship transport do not appear to be as high as transport by road. Train transport on the other hand does show higher anticipated accelerations (2g), however, it is assumed here that this means of transportation is conducted with the tower flanges sufficiently supported/gripped by the transport equipment.

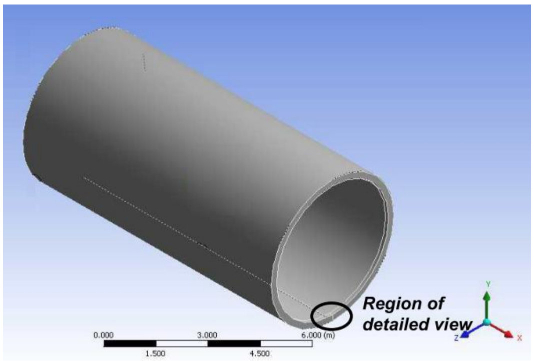

Figure 4.14: Transport load case 1 [1].

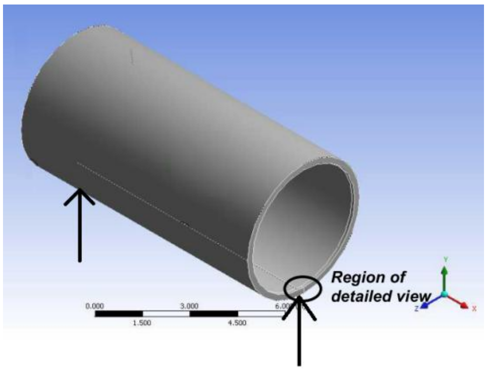

Figure 4.15: Transport load case 2 [1].

Two load cases were investigated. (1) The tower section lying on its side, supported along a line and loaded by gravity. (2) The tower section lying on its side, supported solely underneath the flanges and loaded by gravity. The latter load case is more demanding and therefore this load case is used to derive minimum flange dimensions.

Diameter	Flange height $[m]$	Flange width $[m]$	Section wall thickness $[m]$	Maximum stress outer point shell $[MPa]$	Maximum stress inner point shell $[MPa]$
4500-6500	80-160	120-320	30-80	100-700	100-700

Table 4.16: Investigated flange dimension transport load case.

A FEM analysis is done [1] for different flange designs to calculate the stresses due to the transportation load case, see Table 4.16. For a feasible flange design, these stresses, including a safety factor, should not exceed the yield stress.

The importance of the transportation load case is indicated by Table 4.18 and Table 4.18. For the 30 6MW-SWT reference projects mentioned before, new flange designs are made. But this time the transportation load case was disabled. The average mass of the flanges is up to 65% lower when this load case is not taken into account. This is due to the fact that the transportation load case is governing for the flange width. Disabling this load case dramatically reduces the flange width, see Table 4.18.

	SWP	**Imp. Opt.**	**StaCa1**	**StaCa2**	**StaCa3**
UMF width difference [%]	-56	-62	-52	0	0
LMF width difference [%]	-49	-49	-44	0	0
BF width difference [%]	-12	-13	-11	0	0

Table 4.17: Flange width difference when transportation load case is disabled.

	SWP	**Imp. Opt.**	**StaCa1**	**StaCa2**	**StaCa3**
UMF average mass difference [%]	-62	-66	-51	-1	-7
LMF average mass difference [%]	-48	-47	-44	-4	-
BF average mass difference [%]	-12	-13	-13	-2	-
Total average mass difference [%]	-39	-40	-35	-2.44	-

Table 4.18: Average mass difference when the transportation load case is disabled.

Above statements indicate that a closer look to the transportation load case will be justified.

The used FEM model might be too conservative by assuming the tower section to be point loaded at the flanges. Furthermore, the actual loads due to transportation can be reduced. One of the options might be the introduction of (internal or external) frames when transporting the tower sections. Crosses can be used for example to internally support the structure. Another option to reduce the loads in this load case is the use of cradles, so that the loads on the flanges are distributed more equally.

4.8 Alternative to standardization

An alternative to standardization could be the introduction of a versatile clamping mechanism to handle the tower sections. In this way the handling equipment doesn’t have to be redesigned from project to project. However, other benefits of flange standardization (internals, safety, stock inventory) are not exploited. Furthermore, a study within SWP showed that such a versatile clamping mechanism has the following drawbacks: higher investment costs, lower speed of operation and higher chances on flange damage [1].

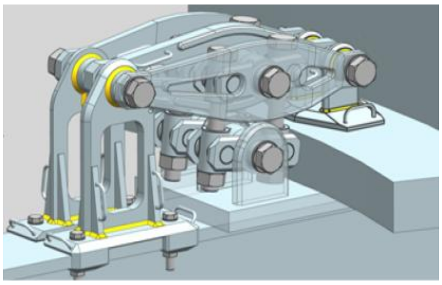

Figure 4.16: Versatile clamping mechanism [1].

Another alternative is the introduction of an unequal bolt pattern. Only at the places where the handling equipment has interfaces with, the distance between the bolts and the bolt diameter should be standardized. Between these places, the most optimal bolt hole configuration can be chosen. A drawback of this alternative is that the bolts are not spread equally over the circumference and hence the assumptions of equal uniform single bolt connections cannot be made anymore. FEM analyses should identify the influence of such a pattern on the failure modes of the flange as a whole.

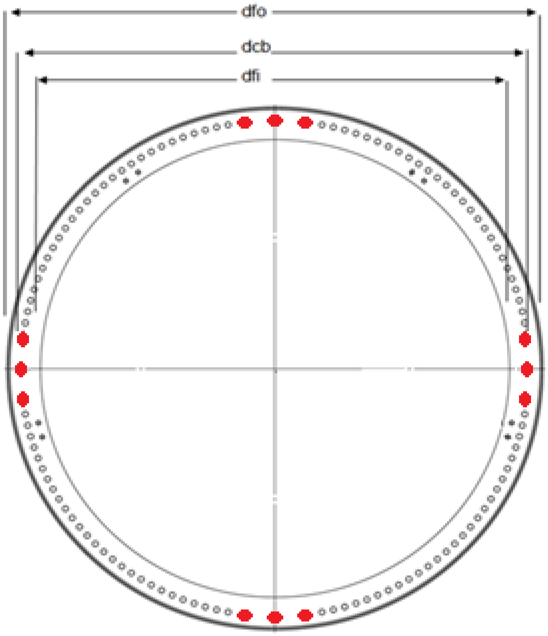

Figure 4.17: Example of flange with unequal bolt pattern [1].

4.9 Conclusions

By using the proposed improved optimization method instead of the SWP method, 2.5% cost savings can be realized on the flange connections. In this case the flanges are optimized per project and no standardization takes place. These savings are caused by the use of the cost performance function instead of the Pareto optimum performance function.

Three different standardization cases are considered, see Table 4.8. Standardizing the number of bolts, bolt diameter and bolt circle diameter (standardization case 1) of the flange connections yields additional costs of +2.7% per wind turbine in comparison with the improved optimization case. In standardization case 2, besides the case 1 parameters, also the flange width is standardized. The flange costs of standardization according case 2 are 7.2% higher than the flange costs according the improved optimization case. Standardization according case 3 is not always possible for the bottom flange and lower middle flange and will therefore be disregarded.

The costs of standardization are hereby quantified and listed in Table 4.19. The plenty benefits of standardization are identified and also listed in Table 4.19. Quantification of these benefits falls behind the scope of this project and is therefore not done.

Considered case	**Costs**	**Benefits**
Improved optimization	• Non	• -2.5% flange costs decrease
Standardization case 1	• Flange costs increase +2.7%	• handling equipment standardization on fixed bolt pattern • risk mitigation • stock inventory
Standardization case 2	• Flange costs increase +7.2% costs	additional benefits over benefits standardization case 1: • handling equipment standardization on fixed inner diameter flange • internals standardization

Table 4.19: Costs and benefits improved optimization and standardization.

It is notified that the transportation load case is often governing for the flange width. A reduction of the loads by the flange transportation will yield flange designs which flange width (and hence mass) can be reduced.

Chapter 5

5 Sector based fatigue design

This chapter briefly investigates the influence of the introduction of sector based fatigue loads in combination with sector based SN-curves and Stress Concentration Factors (SCFs). After explaining the SWP approach (Section 5.1), the use of SN-curves and SCF will be discussed (Section 5.2). An improved sector based design approach will be suggested in Section 5.3. Section 5.4 gives a brief discussion about the approach.

5.1 SWP approach

This first section will describe how within SWP the FLS loads for offshore tower design are calculated nowadays.

With use of the aeroelastic code BHawC (comparable with HAWC2, see Section 3.1), simulations are done for many different sea states. The data for the definition of these sea states are normally subtracted from measurements. The environmental loading in the simulations is coming from different directions, following the wind and wave roses according the measurements. BHawC is able to get the internal tower forces and moments as output for different locations in the tower (normally at the flange heights). These forces and moments can, with use of simple equations, be transformed into tower shell stresses (see Section 2.2.3).

For the fatigue calculations, the tower circumference is divided into 12 equal sectors of 30° each, see Figure 5.1. After all the simulations, a stress amplitude histogram for every single sector is made. This is often done at all the flange heights.

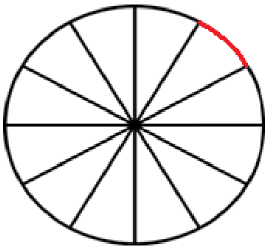

Figure 5.1: One sector at circumference of tower.

The stress histogram of the sector with the highest equivalent damage is chosen as FLS design driven. In theory, every sector can have a different SCF and SN-curve. However, within SWP, for the equivalent damage calculations the most conservative SCF and SN-curve of all the segments are chosen and are assumed to be present at the whole circumference.

5.2 SCFs and SN-curves

Irregularities (door frame, cable exit holes, etc.) will cause *local* stress concentrations and should therefore not be taken on the whole circumference but only at the sector(s) they act on.

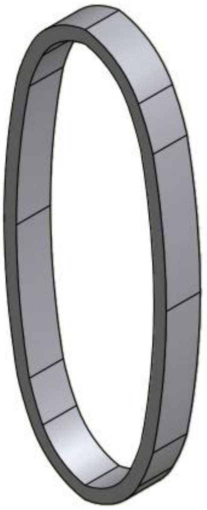

Figure 5.2: Door frame [1].

A typical bending SCF value for a door frame is between 1.5 and 2.0. It strongly depends on the wall thickness and door frame thickness. The SCFs for torsion are higher, although they are not important because the torsion stresses at the door location are normally much lower than the stresses due to bending. The SCFs can be determined with use of a finite element analysis. Because the SCFs at the door frame are relatively high, a post welding process called grinding is used to increase the detail category of the SN-curve. According the DNV design guide for fatigue design [67], a detail category of 112 can be used.

In a tower section can, the circumferential and longitudinal weld come together and a detail category of 90 has to be used. If a tower internal component is welded to the tower sections as well, a reduced detail category of 80 is adapted.

Above examples show that the appropriate SN-curves differ significantly for the different welds.

5.3 Improved approach

Improvements in fatigue design can be made if every sector on the circumference will have its own specific SN-curve and SCF, depending on the local geometry, instead of assuming the most conservative SN-curve and SCF on the whole circumference.

The door frame will cause the highest fatigue damage and hence should be directed in the direction with the lowest equivalent load. The direction of the door is nowadays determined by the orientation of the boat landing, which orientation is dependent on the most prevailing wave direction. The design of the transition piece platform decides the door orientation. The orientation of the door and the most prevailing wind directions is hence project specific. For the current fatigue calculations it is assumed that the door is directed in the most severe fatigue direction. The difference in fatigue damage between the current approach and the sector based approach (assuming the door frame is directed in the least loaded fatigue direction) can be calculated with use of five 6MW-SWT reference projects for which the fatigue calculations are done sector wise.

These projects show that the equivalent fatigue loads differ up to 12% between the different sectors on the circumference. Directing the door frame in the least loaded direction yields an equivalent load reduction of 12%. Table 5.1 shows the influence of the load reduction on the total tower mass. A total tower mass reduction up to 6% can be realized by an equivalent load reduction of 12%. It is important to note that this only the case for FLS driven designs. ULS driven designs don't have this benefit. Whether a tower is FLS or ULS driven differs from project to project. The considered projects were fatigue driven.

		Equivalent load reduction			
		0%	5%	10%	12%
Total tower mass $[tonnes]$	Project X	424.07	412.29	401.91	397.47 (-6%)
	Project Y	362.09	355.37	349.17	347.16 (-4%)

Table 5.1: Equivalent load reduction with sector based fatigue design calculated with two example reference projects.

5.4 Discussion

For a sound prediction of the sector based loads, detailed environmental data are of high importance. Wind turbines have a design life time of 25 years and it might be possible that the directions of the different types of loading (wind/wave/current) will change over the years. Climate changes could be a reason for this. Before applying a sector based fatigue design, it should be assured that an accurate prediction of the loads and its direction can be given. If this is the case, past projects show that up to 6% can be saved on the tower mass in case of fatigue governed tower designs.

Chapter 6

6 Multiaxial fatigue in tower design

Structures are always loaded in a multiaxial way, as explained in Section 2.1.6. In the GL guideline for the certification of offshore wind turbines [68], it's stated that a simplified fatigue analysis is only permissible in case of predominantly uniaxially loaded components. For predominantly multiaxially loaded components, this is not permissible and a multiaxial fatigue approach would be suited to get a more accurate fatigue life time prediction. The International Institute of Welding (IIW) code [21] states that this is the case when the shear stress amplitude is larger than 15% of the normal stress amplitude.

The shear stress is often not taken into account for tower welds within wind industry [1] because it's assumed that the used safety factors on the normal stress are sufficient to cover the extra damage caused by the shear stress. Safety factors vary between 1.1 and 1.4 depending on the design code. This chapter will investigate if these load safety factors are sufficient to cover the extra damage due to the shear loading according the multiaxial models introduced in this chapter.

Section 6.1 will explain for which sea states the normal and shear stresses in the tower welds will be considered. These stresses will be showed in graphs in Section 6.2. The damage due to combined in-phase loading will be considered in Section 6.3. Section 6.4 will explain the Effective Equivalent Stress Hypothesis (EESH), which will be used to indicate the damage effects of combined out-of-phase loading in tower welds. These results are presented in Section 6.5. The phase angle is an important parameter in this hypothesis. A method to determine the loading phase angle between the stress components on the fatigue life will be investigated in Section 6.6. Section 6.7 tries to place the EESH in perspective in comparison with other fatigue models. With use of this analysis and the assumption about the phase angle, Section 6.8 will discuss the obtained results. These results are discussed with the author of the article which describes the EESH, C.M. Sonsino. This is done in Section 6.9. The main outcome of this discussion is that in practical situations a simplified EESH is used. The results according this hypothesis are described in Section 6.10. The conclusions of this chapter are presented in Section 6.11.

6.1 Description simulations

The multiaxial fatigue calculations will be applied on the bottom flange weld and upper middle flange weld for two different wind turbines. These flanges are chosen to indicate the difference between the lowest and highest located tower specific flange connection (top flange connection is turbine specific, see Section 2.3). The considered turbines which are used as examples are the 5MW-NRELT [55] and the 6MW-SWT [1]. Their properties are described in Appendix D. The 6MW-SWT tower has a cylindrical shape from bottom flange till the upper middle flange and a conical shape from the upper middle flange till the top flange, while the 5MW-NRELT has a conical shape over the whole length of the tower. Aeroelastic simulations (with use of HAWC2 for the 5MW-NRELT and BHawC for the 6MW-SWT) are run for cut-in wind speed, rated wind speed and cut-out wind speed. The sea state that comes closest to the considered wind speed is chosen, see Appendix E. The wind and waves are assumed to come from the most prevailing direction. Simulations of 10 minutes are done with three different seeds and the values are averaged. The damages on the flange welds are calculated for the bottom flange and the upper middle flange and the 10-minute values are recalculated to 25 year life time values. It should be noted that the damage calculations are highly dependent for the tower geometry. Changing the wall thickness and/or diameter will change the results rapidly.

6.2 Motivation to consider multiaxiality in tower welds

With use of simple analytical calculations the stresses in a tower weld can be calculated. Consider the situation as depicted in Figure 6.1. The axes according HAWC2 are used, see Section 3.1. The stresses in the points A and B can be calculated in an analytical way. It will be investigated if the shear stresses due to the torque should be considered in the fatigue calculations. The following equations show how the normal stress due to the bending moment and the shear stress due to the torque and horizontal loading can be calculated.

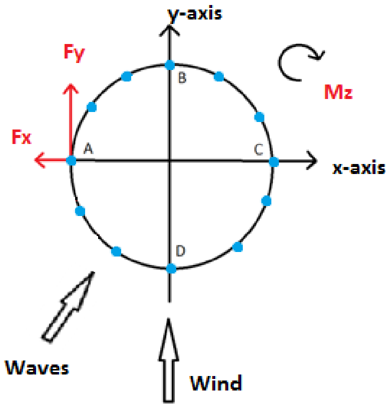

Figure 6.1: Top view tower can: loads on point A.

The normal stress in the tower shell at point A can be calculated as follows.

$$\sigma_z = \frac{M_y}{W} - \frac{F_z}{A_{shell}} \qquad \text{Equation 6.1}$$

The first term is called the flexure formula. It is used to determine the normal stress in a straight member. The section modulus W is calculated in Equation 2.12. F_z represents the loading due to the mass of the wind turbine. The shear stress in point A is expressed in Equation 6.2.

$$\tau_{zy} = \frac{F_y}{A_{sh}} + \frac{M_z}{W} \qquad \text{Equation 6.2}$$

The stresses in point B can be calculated in a similar way.

$$\sigma_z = \frac{M_x}{W} - \frac{F_z}{A_{sh}} \qquad \text{Equation 6.3}$$

$$\tau_{zx} = \frac{F_x}{A_{sh}} + \frac{M_z}{W} \qquad \text{Equation 6.4}$$

The stresses at the bottom flange and upper middle flange at the points A and B are displayed in the next figures for cut-in, rated and cut-out wind speeds of the considered wind turbines. Figure 6.2-Figure 6.4 show the tower stresses for the 5MW-NRELT. The plots of the 6MW-SWT are displayed in Figure 6.5-Figure 6.7.

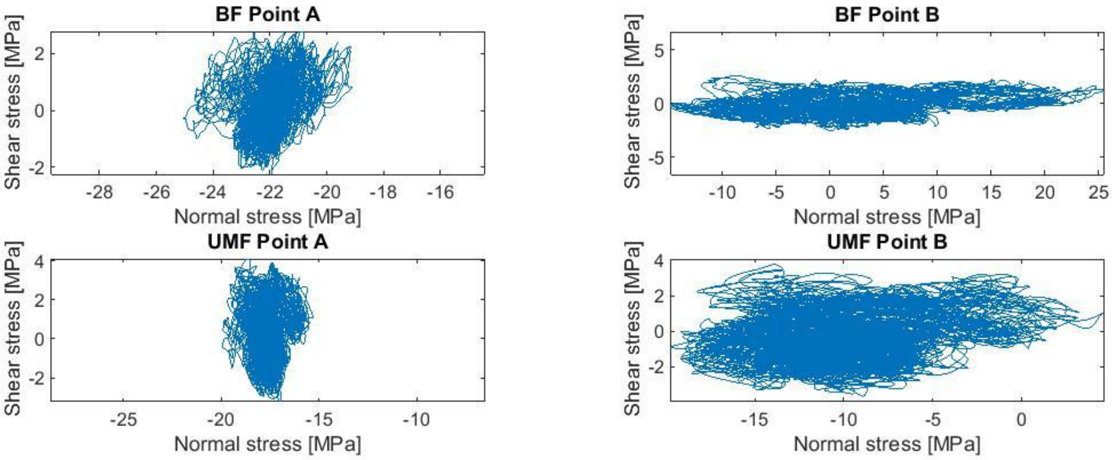

Figure 6.2: Stress components at cut-in wind speed 5MW-NRELT.

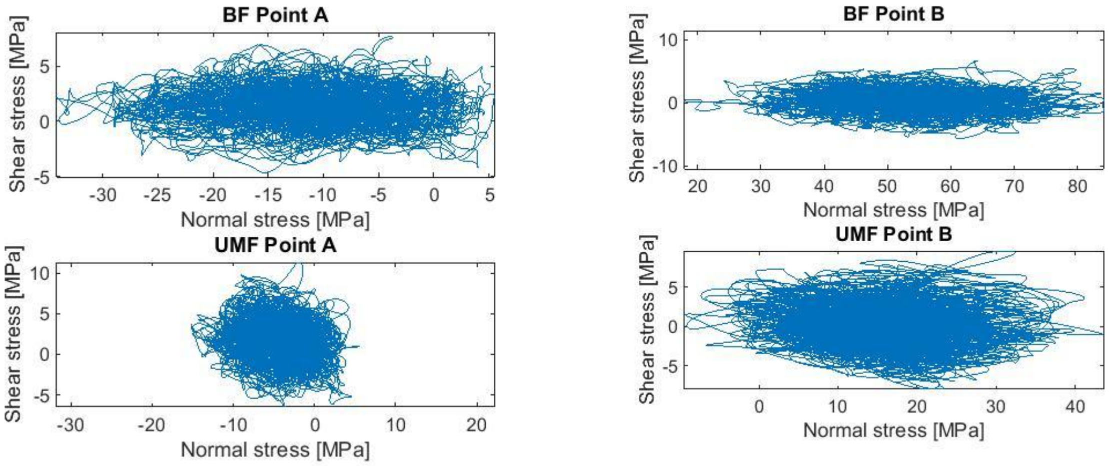

Figure 6.3: Stress components at rated wind speed 5MW-NRELT.

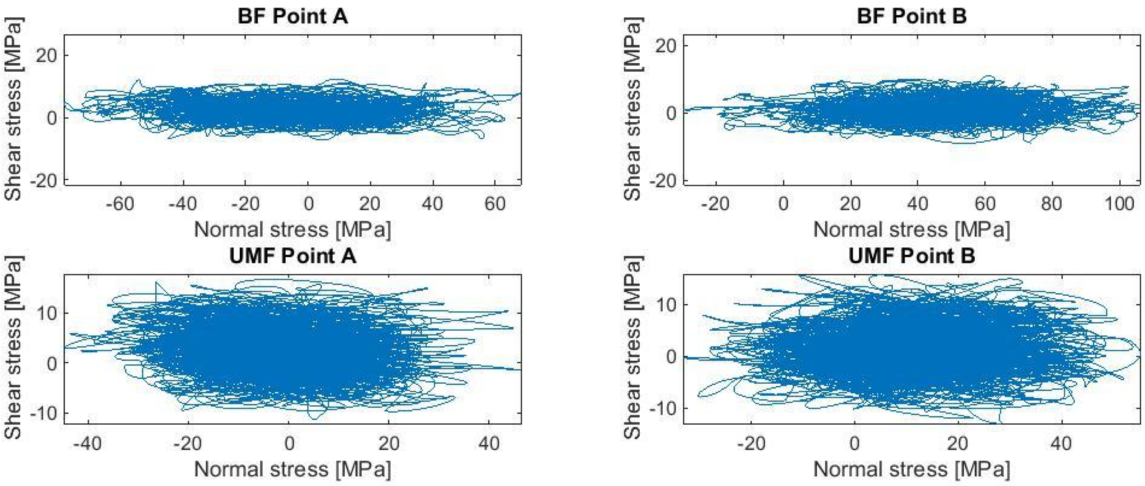

Figure 6.4: Stress components at cut-out wind speed 5MW-NRELT.

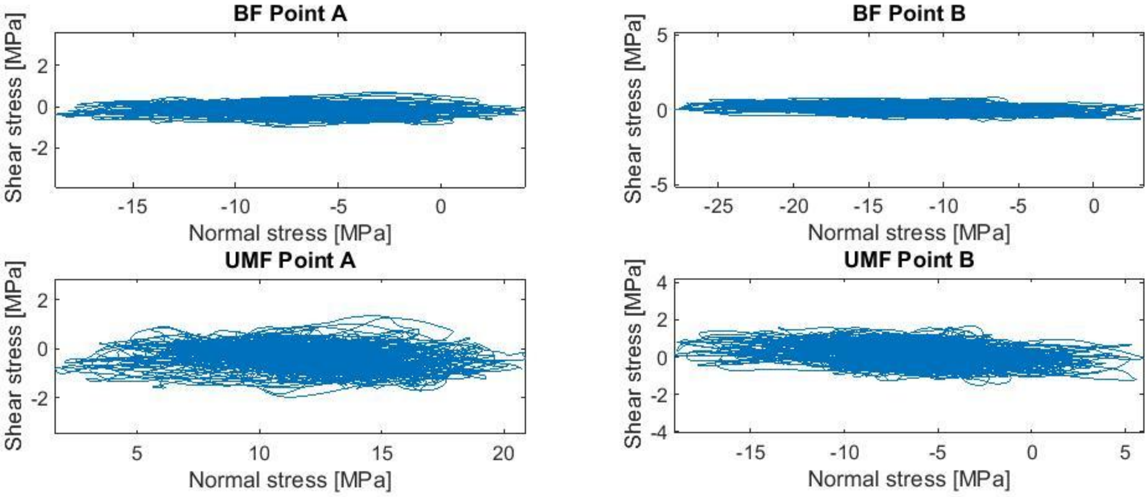

Figure 6.5: Stress components at cut-in wind speed 6MW-SWT.

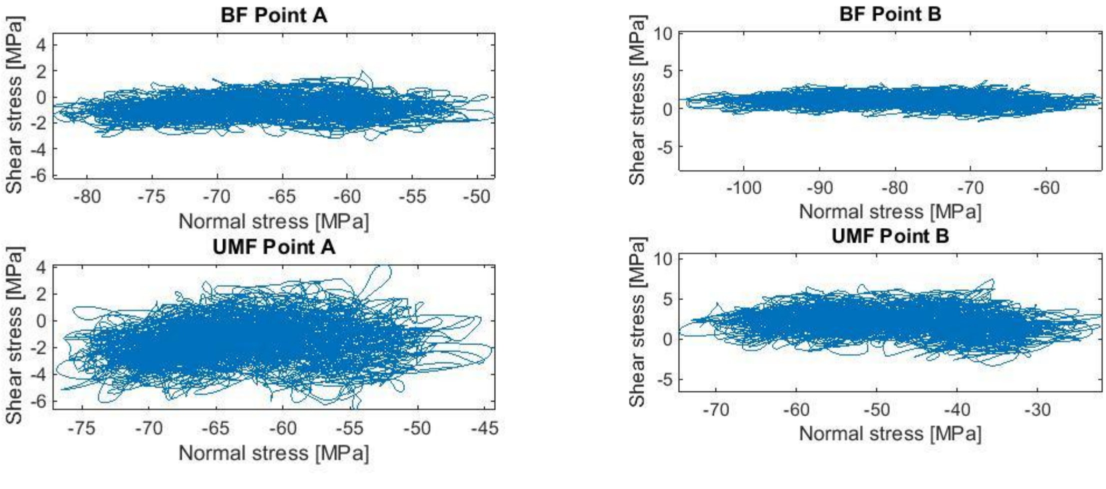

Figure 6.6: Stress components at rated wind speed 6MW-SWT.

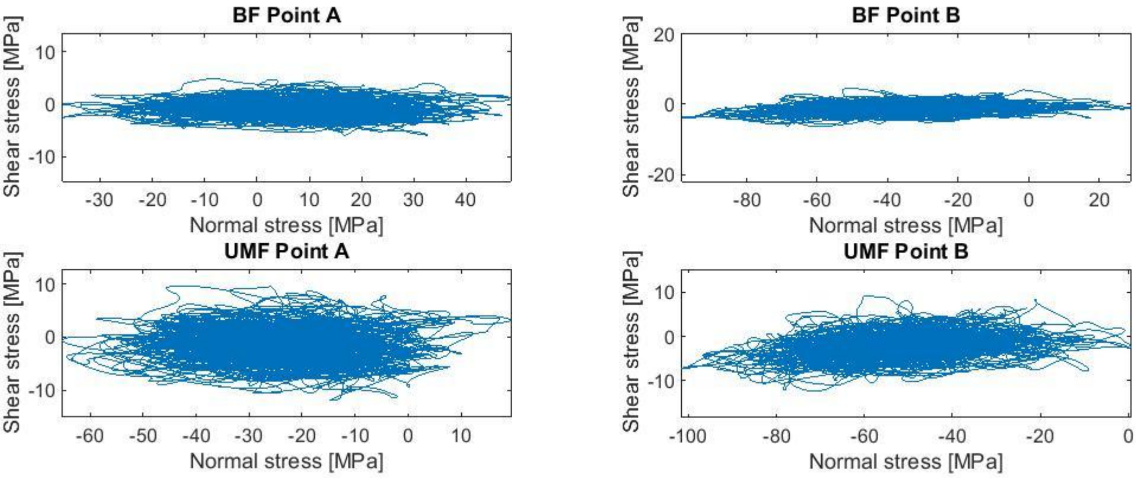

Figure 6.7: Stress components at cut-out wind speed 6MW-SWT.

From Figure 6.2-Figure 6.7 it can be concluded that in all three the wind speeds shear stresses contribute to the stress state. This is in case of the 5MW-NRELT more than for the 6MW-SWT; see Table 6.1-Table 6.2. The ratio of the shear stress amplitude and the normal stress amplitude depends on the tower geometry and control system, which is project and turbine specific.

Flange	Cut-in wind speed	Rated wind speed	Cut-out wind speed
BF	13%	18%	15%
UMF	30%	33%	32%

Table 6.1: Percentage max shear stress amplitude of max normal stress amplitude in point B 5MW-NRELT.

Flange	Cut-in wind speed	Rated wind speed	Cut-out wind speed
BF	3%	5%	4%
UMF	6%	11%	10%

Table 6.2: Percentage max shear stress amplitude of max normal stress amplitude in point B 6MW-SWT.

The amplitudes of both the shear stresses and normal stresses increase with higher wind speeds. The ratios between the shear stress amplitudes and normal stress amplitudes are higher for the upper middle flange than for the bottom flange, because the bending moments decreases over height while the torsion moments remain the same (see the figures in Appendix F). In point A, where the bending moment due to the wind has less influence on the normal stress than in point B, the shear stress range is even larger than the normal stress range at the upper middle flange for cut-in wind speeds. However, the fatigue design of the tower weld is governed by the loading in point B, because the normal stress ranges are much higher here due to the bending moment caused by the wind. Therefore, in point B the maximum shear stress amplitude is compared with the maximum normal stress amplitude, as listed in Table 6.1.

As can be concluded from Figure 6.2-Figure 6.7, stress components can be out-of-phase and the amplitude of the secondary component can be larger than 15% of the primary stress component amplitude (see Table 6.1). From the theoretical background (Section 2.1.6) it can be concluded that a multiaxial approach in the fatigue life calculations of the tower weld would be suited in order to get the most reliable fatigue life prediction. A better fatigue life prediction can reduce the safety factor used nowadays for welds (γ=1.1-1.4).

To indicate the increased damage due to in-phase combined loading in comparison with the conventional uniaxial nominal stress method, the Gough Pollard algorithm will be applied, see Section 6.3.

6.3 In-phase damage ratios according Gough-Pollard

The IIW [21] states that the effect of the combination of normal and shear stresses can be assessed on the basis of the criteria of Equation 6.5.

$$\left(\frac{\Delta\sigma_{eq}}{\Delta\sigma_R}\right)^2 + \left(\frac{\Delta\tau_{eq}}{\Delta\tau_R}\right)^2 \leq D \qquad \text{Equation 6.5}$$

This equation is called the Gough-Pollard algorithm. $\Delta\sigma_{eq}$ and $\Delta\tau_{eq}$ represent the calculated constant amplitude stresses ranges. They cause the same damage as the variable stress range history (for the same number of cycles). $\Delta\sigma_\mathrm{R}$ and $\Delta\tau_\mathrm{R}$ represent the design resistance normal and shear stress ranges respectively for the specified number of cycles and the appropriate detail category. According the IIW code, an allowable damage sum of 1 can be assumed for damage due to in-phase loading and 0.5 for damage due to out-of-phase loading. This means in this section the allowable damage sum is assumed to be 1. The influence of combined in-phase loading will be investigated with use of this algorithm.

The damage values according the conventional uniaxial nominal stress method used nowadays within SWP are listed in the third column of Table 6.3 and Table 6.4. The ratios of the damage according the combined in-phase loading (Gough-Pollard) and the damage according nominal stress situation are listed in the last column.

Wind speed	Flange	Nominal stress life time damage	Damage ratio combined in-phase loading
Cut-in (3m/s)	BF	0.039	1.16
	UMF	0.0042	1.40
Rated (11m/s)	BF	0.15	1.20
	UMF	0.028	1.44
Cut-out (25m/s)	BF	18.5	1.16
	UMF	0.9	1.36

Table 6.3: Damage values 5MW-NRELT [55].

Wind speed	Flange	Nominal stress life time damage	Damage ratio combined in-phase loading
Cut-in (3m/s)	BF	0.005	1.06
	UMF	0.0016	1.10
Rated (11m/s)	BF	0.018	1.11
	UMF	0.013	1.18
Cut-out (25m/s)	BF	4.45	1.09
	UMF	1.85	1.12

Table 6.4: Damage values 6MW-SWT [1].

The following points can be concluded from the Table 6.3 and Table 6.4:

- The higher the wind speed, the higher the fatigue damage.
- The bottom flange welds are more prone to fatigue than the top flange welds.

These conclusions match the fatigue conclusions from Section 3.4. Furthermore it can be concluded that taking the in-phase shear stress into account causes damage up to 1.5 times higher than calculated with the nominal method. The influence of the combined out-of-phase loading in comparison with the combined in-phase loading will be calculated with use of the EESH in Section 6.5. First, an explanation of the EESH will be given in Section 6.4.

6.4 The Effective Equivalent Stress Hypothesis

The effect of out-of-phase shear loading will be investigated with the EESH by Prof. C.M. Sonsino [24]. C.M. Sonsino is an expert researcher with almost 40 years of experience in multiaxial fatigue. He is co-author of many IIW documents and nowadays working at the Fraunhofer Institute in Darmstadt, Germany. The EESH is a local stress-based modification of the von Mises hypothesis and is developed to overcome the deficiencies of the conventional von Mises hypothesis, which is not able to take into account the fatigue life reducing effects of non-proportional loading. The EESH assumes that failure of ductile materials under multiaxial stress states is initiated by shear stresses. The hypothesis considers the fatigue-life-reducing influence of out-of-phase loading by taking into account the interaction of local shear stresses acting in different surface planes of the material [69].

The method in the article [24] is described with use of harmonic signals. However, the multiaxial stress components in a tower weld have a stochastic character. Research showed that there is no difference between constant amplitude and spectrum loading; in both cases out-of-phase loading reduces the fatigue life. Some assumptions/simplifications and modifications of the stress components are needed to apply the EESH. The following section is written in consultation with C.M. Sonsino and will describe how the EESH can be applied on multiaxial fatigue calculations of tower welds. A simplified 2D approach is used.

6.4.1 EESH procedure in short

This section will shortly discuss the steps to be taken to apply the EESH. The following parameters have to be calculated:

- Shear stress spectrum
- Effective damage sums
- Effective equivalent stress
- Cumulative multiaxial fatigue life

The procedure will shortly be discussed point by point in the next section. These points will be explained in more detail in Section 6.4.2.

6.4.1.1 Shear stress spectrum

For simplicity, assume a component to be loaded harmonically by tension and torsion stresses. The phase angle difference between the tension and torsion stresses is called δ. Shear stresses $\tau_n(\phi,\delta)$ acting in various interference planes ϕ of a surface element in a weld have to be calculated. The shear stresses in a butt weld are displayed in Figure 6.8. A 2D stress situations is assumed.

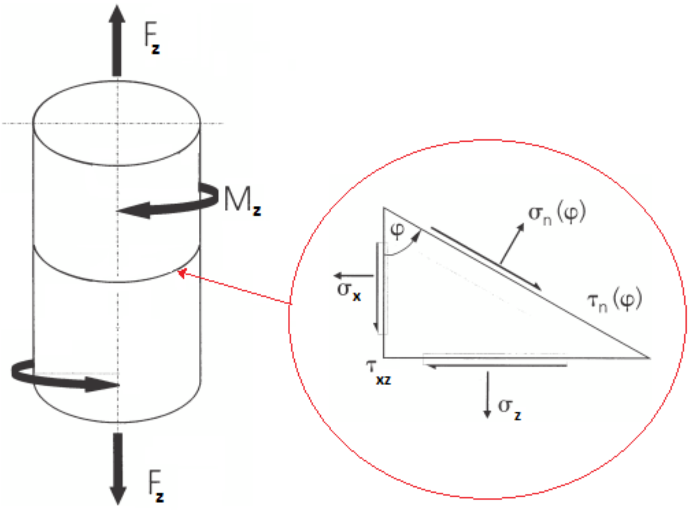

Figure 6.8: Interference planes in a tower section weld [24].

By using the rainflow counting the shear stress spectra for each interference plane can be calculated.

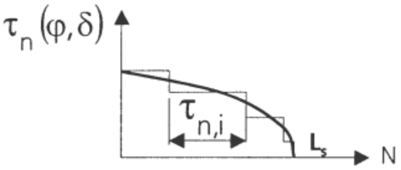

Figure 6.9: Example of shear stress spectrum [24].

The arithmetic mean values of shear stress amplitudes have to be calculated with use of the spectrum length L_s, see Equation 6.6.

$$AMV(\phi) = \frac{1}{L_s} \cdot \sum_{i=1}^{L_s} \tau_{n,i}\ (\phi) \qquad \text{Equation 6.6}$$

6.4.1.2 *Effective damage sums*

With this value, the effective damage sum (EDS) of the arithmetic mean values of shear stress amplitudes in an interference plane can be calculated as showed in Equation 6.7.

$$EDS(\delta) = \frac{1}{\pi} \cdot \int_0^{\pi} AMV(\phi) d\phi \qquad \text{Equation 6.7}$$

This effective value represents the interaction of shear stresses in various interference planes ϕ which initiate corresponding dislocations. A decrease of fatigue life can be observed when principal stress directions vary. The effective damage sum will be used in the calculation of the effective equivalent stress.

6.4.1.3 *Effective equivalent stress*

The effective equivalent stress range, which is the governing for fatigue damage calculations, can be calculated with Equation 6.8.

$$\Delta\bar{\sigma}_{eq}(\delta) = \Delta\bar{\sigma}_{eq}(\delta = 0°) \cdot \frac{EDS(\delta)}{EDS(\delta = 0°\,)} \cdot \sqrt{\left(SM \exp\left(1 - \left(\frac{\delta - 90°}{90°}\right)^2\right)\right)} \qquad \text{Equation 6.8}$$

With the in-phase equivalent stress as stated in Equation 6.9.

$$\Delta\bar{\sigma}_{eq}(\delta = 0°) = \sqrt{\Delta\bar{\sigma}_x^2 + \Delta\bar{\sigma}_z^2 - \Delta\bar{\sigma}_x \cdot \Delta\bar{\sigma}_z + \kappa^2 \cdot 3\Delta\bar{\tau}^2} \qquad \text{Equation 6.9}$$

The maximum value of the effective equivalent spectrum of amplitudes $\Delta\bar{\sigma}_{eq}(\delta)$ is calculated using the maximum values of the normal ($\Delta\bar{\sigma}_z$) and shear stresses ($\Delta\bar{\tau}$) ranges. The sliding modulus SM from Equation 6.8 can be computed with use of the stress concentrations factors for bending and torsion (SCF_{be} and SCF_{to}), see Equation 6.10.

$$SM = \frac{1 + SCF_{be}}{1 + SCF_{to}} \qquad \text{Equation 6.10}$$

The size effect factor can be computed as shown in Equation 6.11.

$$\kappa = \frac{\sigma_{eq\,(pure\ axial\ or\ bending\ load)}}{\sigma_{eq\,(pure\ torsion)}} \qquad \text{Equation 6.11}$$

This size effect factor is determined by comparing the SN-curve for pure axial or bending stress with that for pure torsion on the basis of local supportable stresses. The factor reflects the influence of the maximum stressed material volume on the supportable local stress [24].

The effective equivalent stress spectrum of amplitudes is determined whereas for the shape of this effective spectrum the shape of the stronger load component is taken, in the case of a tower weld the normal stress. This practically means that the normal stress is multiplied with the EESH amplification factor $\frac{\Delta\bar{\sigma}_{eq}(\delta)}{\Delta\bar{\sigma}_z}$, see Equation 6.12.

$$\sigma_{eq}(t, \delta) = \frac{\Delta\bar{\sigma}_{eq}(\delta)}{\Delta\bar{\sigma}_z} \cdot \sigma_z(t) \qquad \text{Equation 6.12}$$

6.4.1.4 Calculation of the cumulative multiaxial fatigue life

With use of the equivalent stress from Equation 6.12 the cumulative fatigue life calculations can be performed.

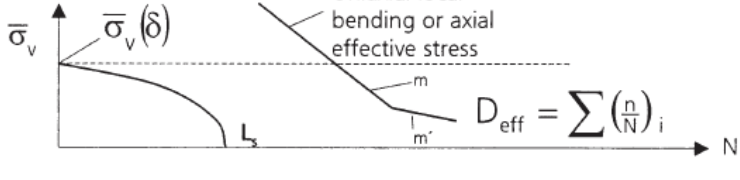

Figure 6.10: Cumulative fatigue calculation [24].

The SN-curve to use is dependent on whether combined in-phase or out-of-phase loading is considered, the stress concept, and the weld category. Details in case of a tower weld can be found in section 6.4.3.

6.4.2 EESH results according the articles

C.M. Sonsino investigated the EESH theory for a tube-plate and tube-tube specimen [24] [70]. The results were obtained under constant amplitude loading with combined bending and torsion. It was showed that both for constant amplitude and spectrum loading (tower weld) the life time is reduced by combined out-of-phase loading in comparison with combined in-phase loading. The experiments are conducted with a constant normal stress to shear stress amplitude ratio of $\sqrt{3}$. Tests were conducted on machined and unmachined specimen. In all cases, out-of-phase loading results in a decrease of fatigue life up to a factor 4 in comparison with in-phase loading.

6.4.3 EESH application tower weld

This section will discuss in detail how the aforementioned EESH steps can be applied for a tower weld. It is important to note that in case of environmental loaded structures the torsional and bending stress components are no harmonic functions anymore but have a stochastic character. This means that the phase difference, which is important in the EESH, is not easy to identify. The following procedure has to be followed to calculate the damage of the combined out-of-phase loading according the EESH:

- Calculate shear stress spectrum of $\tau_n(\phi)$ for different planes to determine the most damaging plane
- Calculate real out-of-phase effective damage sum $EDS\,(\delta)$
- Calculate in-phase effective damage sum $EDS(\delta = 0°)$ for fictional in-phase situation:
    - Create single frequency signal of most damaging stress (normal stress)
    - Create single frequency signal of secondary stress (shear stress)
- Calculate equivalent stress spectrum
- Calculate cumulative damage

6.4.3.1 Shear stress spectrum

The critical plane calculation method is clearly explained in an article from Susmel [71] and by the book Mechanics of Materials from Hibbeler [72]. The probability of having the crack initiation phenomenon reaches its maximum at the critical plane. Consider a body subjected to a complex system of time-variable forces resulting in a tri-axial stress state. The stress state can be expressed as:

$$[\sigma(t)] = \begin{bmatrix} \sigma_x(t) & \tau_{xy}(t) & \tau_{xz}(t) \\ \tau_{xy}(t) & \sigma_y(t) & \tau_{yz}(t) \\ \tau_{xz}(t) & \tau_{yz}(t) & \sigma_z(t) \end{bmatrix} \qquad \text{Equation 6.13}$$

Assume a loading situation with uniaxial and torsional loading, as in a tower section weld. It is assumed that the stress produced in the weld can be analyzed in a single plane. The material is said to be subjected to plane stress. The general state of plane stress at a point is represented by a combination of two normal-stress components and one shear stress component. In this loading situation, the normal stress component σ_y can assumed to be zero.

Under the considered biaxial loading path the stress state $[\sigma(t)]$ at a generic instant t of the load cycle can be expressed as:

$$[\sigma(t)] = \begin{bmatrix} 0 & 0 & \tau_{xz}(t) \\ 0 & 0 & 0 \\ \tau_{xz}(t) & 0 & \sigma_z(t) \end{bmatrix} \qquad \text{Equation 6.14}$$

The transformed shear stress components can be expressed as [24]:

$$\tau_n(t,\phi) = \tau_{xz}(t) \cdot (cos^2(\phi) - sin^2(\phi)) - \sigma_z(t)\, cos(\phi)\, sin(\phi) \qquad \text{Equation 6.15}$$

6.4.3.2 The effective damage sums

The out-of-phase and in-phase effective damage sums have to be calculated to get the ratio $\frac{EDS\ (\delta)}{EDS\ (\delta=0°)}$, which is part of the equivalent stress calculations (Equation 6.8).

Out-of-phase effective damage sums

The shear stress spectrum of τ_n (Equation 6.15) is used to calculate the arithmetic mean value of all shear stress amplitudes (Equation 6.6). This value is used to calculate the real out-of-phase effective damage sum $EDS(\delta)$ (Equation 6.7). Note that the normal stress $\sigma_z(t)$ and shear stress $\tau_{xz}(t)$ are stochastic signals which have a phase difference that is varying over time. As described above, the effective damage sum $EDS\ (\delta)$ for these signals can be calculated without knowing the value of the phase difference δ.

To be able to calculate the ratio $\frac{EDS\ (\delta)}{EDS\ (\delta=0°)}$ from Equation 6.8, the effective damage sum for a phase difference of 0°, $EDS\ (\delta = 0°)$, should also be calculated. The best practice how to do this is described in the next section.

In-phase effective damage sums

The following steps can be taken in order to calculate the in-phase effective damage sums for random out-of-phase stress signals (in agreement with C.M. Sonsino):

1. Determine most damaging stress component
2. Create fictional single frequency signal of most damaging signal with use of rainflow counting
3. Create out-of-phase single frequency fictional secondary signal so that the combination of the fictional signals give the same critical plane and effective damage sums as the original signals
4. Compare in-phase and out-of phase effective damage sums

Step 1: Determine most damaging stress component

The damage of each of the signals can be calculated with use of the rainflow counting method and applying the appertaining SN-curve and Miner's rule (see Section 2.1.2). In the example situation of Figure 6.11, the most damaging stress component is the normal stress σ_z and the shear stress τ_{xz} is the secondary stress component.

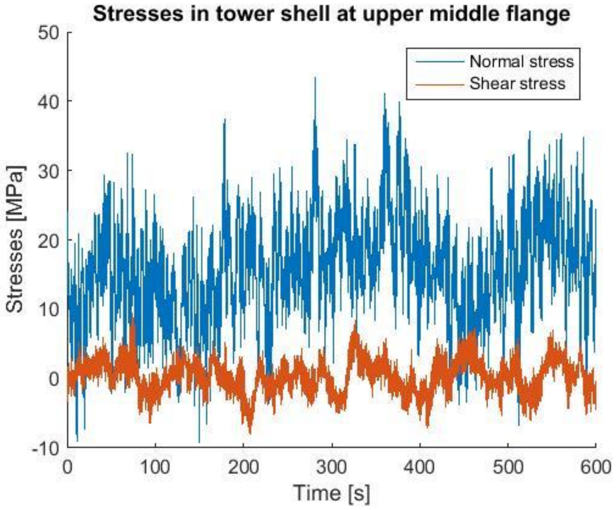

Figure 6.11: Stresses in the tower shell of an example simulation.

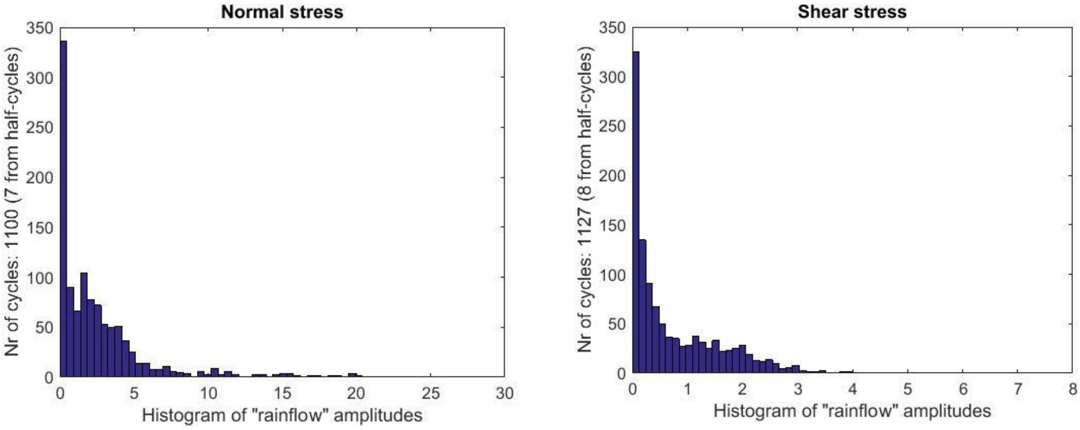

Figure 6.12: Rainflow histogram of normal stress.

Figure 6.13: Rainflow histogram of shear stress.

Step 2: Create fictional most damaging component

The histogram obtained by rainflow counting (Figure 6.12) of the most damaging stress component σ_z has to be used as a basis to create a fictional single frequency signal which generates the same damage as the original most damaging signal. The frequency of the fictional signal is determined by dividing the number of cycles by the simulation time. The amplitudes of the fictional signal are subtracted from the rainflow histogram. In this example the amplitude increases over time, see Figure 6.14. The mean of the original stress component is subtracted for comparison reasons.

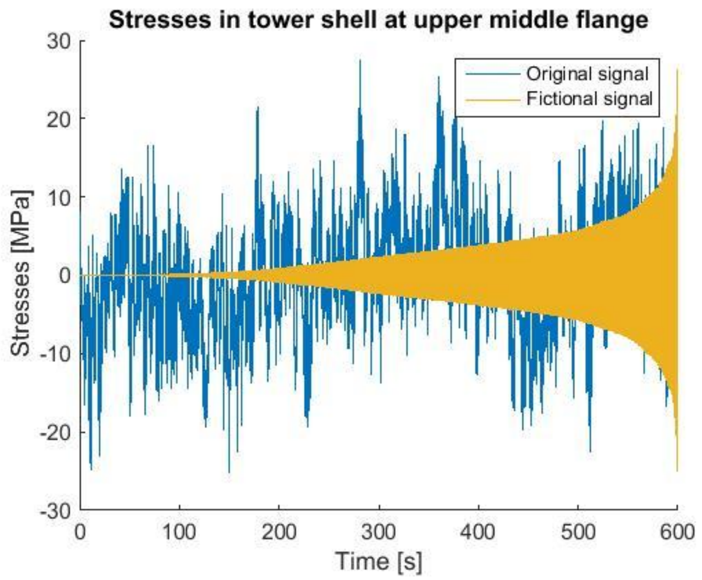

Figure 6.14: Original most damaging stress signal and the fictional one frequency one.

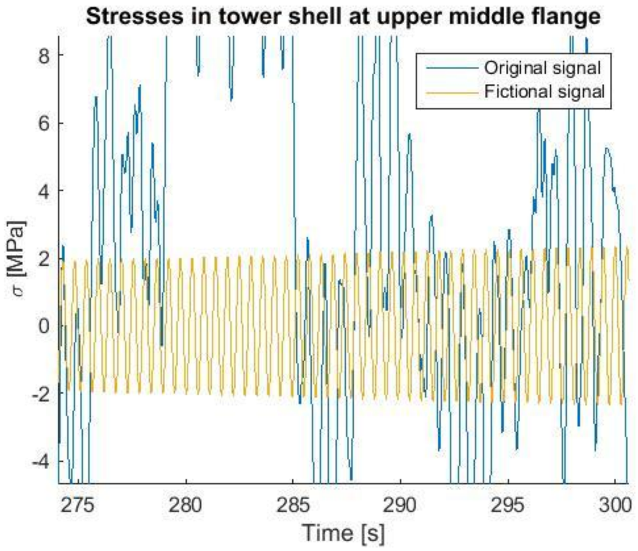

Figure 6.15: Zoom of Figure 6.14.

Step 3: Create fictional secondary component

A fictional 90° out-of-phase single frequency secondary stress component has to be created which represents the shear stress τ_{xz}. The signal has to be tweaked in such a way that both the effective damage sum and critical plane of the fictional signals equal the values of the original signals. The secondary stress component can be changed by playing with the fullness of the amplitude spectrum. This is an iterative process.

The distribution of the amplitudes of the secondary component has the same shape as the distribution of the amplitudes of the most damaging stress (see Figure 6.12 and Figure 6.13). Furthermore, a secondary fictional signal will be suggested that, like the most damaging fictional signal, will increase over time. With this assumption, more stress interaction takes place and the resemblance with the original situation is larger. The calculated influence of the phase shift will therefore be more realistic.

As a starting point for a suggestion for the secondary out-of-phase amplitudes magnitudes, the amplitudes of the most damaging stress component (Amp_{md}) will be scaled with parameter SP_1. In this way it will be tried to realize the same damage and critical plane as the original signal.

$$Amp_{\mathrm{sec}_1}(t) = SP_1 \cdot Amp_{md}(t) \qquad \text{Equation 6.16}$$

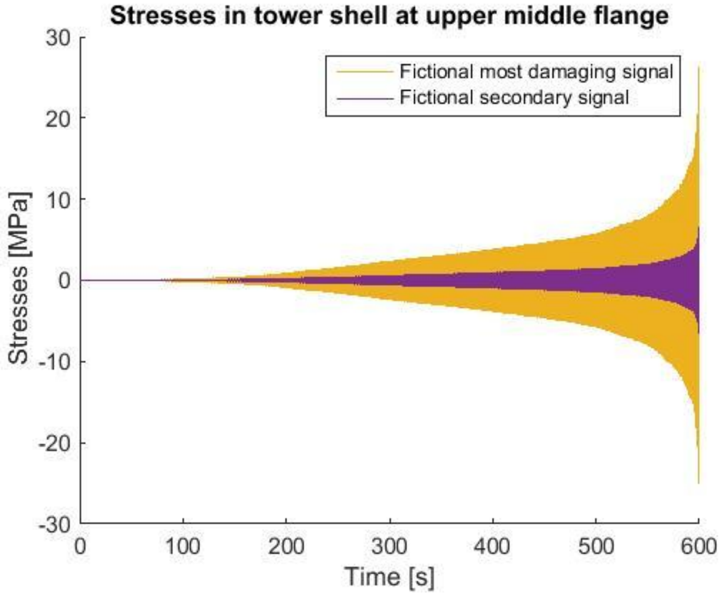

Figure 6.16: Fictional signal following distribution of original signal.

Analyses showed that with this approach it is not always possible to obtain the same critical plane with the fictional signals as with the original.

A new suggestion is made for the amplitude distribution of the secondary signal: a Weibull distribution. This distribution is known to give a good approximation of the load spectrum of environmentally loaded structures in general.

$$Amp_{\mathrm{sec}_2}(t) = SP_2 \cdot \left(\frac{\log n(t)}{\log n_{tot}}\right)^{\zeta} \qquad \text{Equation 6.17}$$

n_{tot} represents the total number of cycles, n the number of cycles that is exceeded (in this case decreasing over time) and ζ the shape parameter, determining the fullness of the amplitude distribution. SP_2 represents again a scaling parameter.

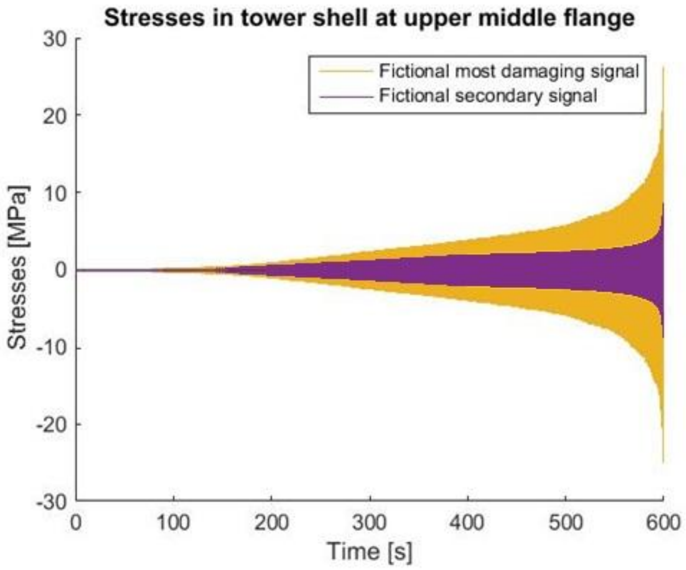

Figure 6.17: Fictional signal following Weibull distribution.

For some loading simulations and certain Weibull parameters the rainflow count algorithm of Matlab was not able to cope with the complex Weibull distribution and it consequently crashed. To overcome this problem, another amplitude distribution is suggested. This last amplitude distribution suggestion for the secondary signal increases linear over time with use of the parameters a and b.

$$Amp_{\mathrm{sec}_3}(t) = (at + b) \qquad \text{Equation 6.18}$$

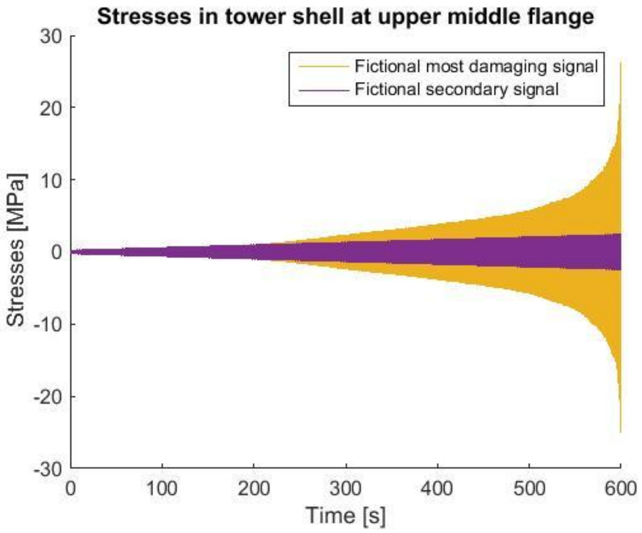

Figure 6.18: Fictional signal following linear distribution.

With a combination of the above suggestions for the amplitude distribution of the secondary fictional signal, in all considered simulations a secondary fictional signal could be created which, in combination with the most damaging fictional signal, gives the same effective damage sum and critical plane as the original signals. The critical plane angels are calculated with steps of 5°. Most of the critical planes were under an angle of 45°.

Step 4: Compare effective damage sums

The fictional secondary signal (δ=90°) has to be shifted in phase with the fictional most damaging component (δ=0°) in order to calculate the ratio between the out-of-phase and in-phase effective damage sums $\frac{EDS\ (\delta)}{EDS\ (\delta=0^\circ)}$. This ratio is in the example situation 1.08.

6.4.3.3 Effective equivalent stress

The effective damage ratio can now be used to calculate the out-of-phase equivalent effective stress. The size effect factor κ (Equation 6.11) is assumed to be 1.13. This value is calculated by comparing the SN-curve for the normal stress (detail category 90) and shear stress SN-curve (detail category 80) [21] [73].

The value for the sliding modulus SM (1.15) is calculated with SCF_{be}(1.35) and SCF_{to} (1.70). These SCFs are the averages of the values used for machined and unmachined tube-tube connections described in an article by C.M. Sonsino [70].

6.4.3.4 Cumulative damage

The design codes DNV-C203 [67], Eurocode 3-1-9 [73], and IIW [21] suggest taking the nominal, hot spot, or structural stress for the fatigue calculations.

IIW suggests taking a damage sum of 0.5, because research showed that 1.0 was non-conservative. Furthermore it has been observed that for spectra with high mean stress fluctuations, the damage sum may be even lower, possibly down to 0.2. This is not the case for a tower weld, so an allowable damage sum 0.5 should be assumed.

Within SWP, tower sections are welded together with use of a transverse butt weld made in the work shop. They are welded from both sides and the misalignment is smaller than 5% of the plate thickness. According the International Institute of Welding [21], the fatigue detail category 90 should be applied. The fatigue resistance values in this guide are based on the nominal stresses, which are also used in the stress calculations in this report.

$\boldsymbol{m_1}$	$\boldsymbol{\Delta\sigma_C}$	$\boldsymbol{k_1 = (2\cdot 10^6 \cdot \Delta\sigma_C^{m1})}$	$\boldsymbol{m_2}$	$\boldsymbol{\Delta\sigma_2 = \left(\frac{k_1}{5\cdot 10^6}\right)^{\frac{1}{m_1}}}$	$\boldsymbol{k_2 = (5\cdot 10^6 \cdot \Delta\sigma_2^5)}$
3	90	$1.458\cdot 10^{12}$	5	66.31	$6.41\cdot 10^{15}$

Table 6.5: SN-curve parameters tower weld.

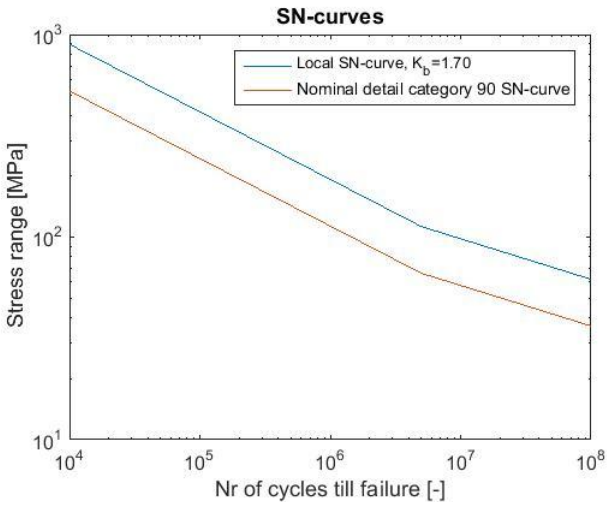

Figure 6.19: SN-curve detail category 90.

The purpose of strength hypotheses in general is converting a multiaxial stress into an equivalent stress, a transformation equivalent to a uniaxial state.

SN-curve combined out-of-phase loading

Regarding the SN-curves for assessing the equivalent combined out-of-phase stresses of the EESH, the basis is the local stress lines obtained under uniaxial loading, so the line of detail 90 category should be recalculated into a local stress line with use of the SCF for bending: SCF_{be}, see Figure 6.19.

SN-curve combined in-phase loading

For assessing the equivalent combined in-phase stress the global SN-curve has to be used (detail 90 category).

Relative damage values

Different SN-curves have to be used for comparing the combined in-phase (local SN-curve) and combined out-of-phase loading (global SN-curve). It's important to note that the obtained damage values can only be used to indicate the damage ratio between the two loading situations.

The absolute damage values for the EESH are hard to obtain because experimental SN-curves have to be determined for combined loading. These were not available in case of a tower weld. Therefore the Gough-Pollard algorithm is used to calculate the ratio of damage according combined in-phase loading to damage according the conventional uniaxial method. Subsequently, the EESH can be used to calculate the ratio of damage according combined out-of-phase loading to damage according combined in-phase loading.

6.5 Out-of-phase damage ratios according EESH

The fatigue damage ratios according the EESH are calculated. The values listed in the next tables are the ratios of damage according combined out-of-phase loading (45° and 90°) to damage according combined in-phase loading.

Wind speed	**Flange**	$\frac{\boldsymbol{EDS\ (\delta)}}{\boldsymbol{EDS\ (\delta = 0^\circ)}}$	**Damage ratio combined 45° out-of-phase loading**	**Damage ratio combined 90° out-of-phase loading**
Cut-in (3m/s)	BF	1.08	1.33	1.74
	UMF	1.13	1.42	1.92
Rated (11m/s)	BF	1.10	1.93	2.42
	UMF	1.15	2.95	3.08
Cut-out (25m/s)	BF	1.08	1.15	1.55
	UMF	1.10	1.34	1.99

Table 6.6: EESH damage parameters 6MW-SWT [1].

Wind speed	**Flange**	$\frac{\boldsymbol{EDS\ (\delta)}}{\boldsymbol{EDS\ (\delta = 0^\circ)}}$	**Damage ratio combined 45° out-of-phase loading**	**Damage ratio combined 90° out-of-phase loading**
Cut-in (3m/s)	BF	1.08	1.62	1.92
	UMF	1.14	2.29	3.15
Rated (12m/s)	BF	1.11	1.85	2.09
	UMF	1.17	3.15	3.46
Cut-out (28m/s)	BF	1.09	1.05	1.34
	UMF	1.11	1.42	2.27

Table 6.7: EESH damage parameters 5MW-NRELT [55].

The results will first be compared with the results from the articles by C.M. Sonsino [24] [70], see Section 2.2. These results were obtained from a tube-tube and tube-plate specimen under constant amplitude loading with combined bending and torsion. The experiments have a constant shear stress-normal stress amplitude ratio of $1/\sqrt{3}$. In case of the considered tower welds, this ratio varies and is lower, as can be seen in Table 6.1 and Table 6.2. The experiments in the article show for 90° out-of-phase loading a decrease in fatigue life with a factor 2-4.5.

For the 90° out-of-phase loading, the applied EESH method predicts fatigue life reductions by a factor between 1.34 and 3.46 (see Table 6.6 and Table 6.7). This range is slightly lower than the experiments in the article show, however this can be explained by the lower ratio shear stress to normal stress and hence a smaller influence of the combined out-of-phase loading.

From Table 6.6 and Table 6.7 it can be concluded that the phase differences between the signals is important in order to get a good estimation of the fatigue life. However, for stochastic signal the phase angle varies over time. Section 6.6 tries to find a method to indicate the appropriate phase angle.

6.6 Phase angle difference analysis

The phase difference between the normal stress and shear stress changes over time and is hard to predict by only considering the signals in the time domain. With two different methods it is tried to obtain the phase difference of the stochastic signals. Use is made of the tower weld stresses in the 5MW-NRELT at the most loaded point (point B, see Figure 6.1) for the bottom flange and upper middle flange.

For the first method, the most governing frequency is determined by analyzing the signals in the frequency domain. The phase angles as a function of the frequency are plot for the separate signals. The phase angles of the two signals corresponding to the most governing frequency (highest peak in frequency spectrum) can be subtracted and assumed to be the phase angle between the stress components. However, after analysis of the phase angles of the stochastic signals, it can be concluded that they are so randomly distributed that it is not a suitable method to find the phase angle between the two stochastic stress components. This method will not be considered furthermore.

The second method to estimate the phase angle between the two stress signals is described in a report by the National Renewable Energy Laboratory (NREL [74]). This method will be discussed in more detail in the next sections.

6.6.1 NREL phase angle approach

The NREL describes how to calculate the phase angle between the peaks of the flap and lead-lag bending moments (out-of-plane and in-plane respectively). The simulated bending moment time series are chopped into single rotor revolution length segments. Since most of the fatigue damage is likely to occur at or near the maximum stress response, the phase angle should be described by using the relationship between normal stress and shear stress peaks [74], as is depicted in Figure 6.20.

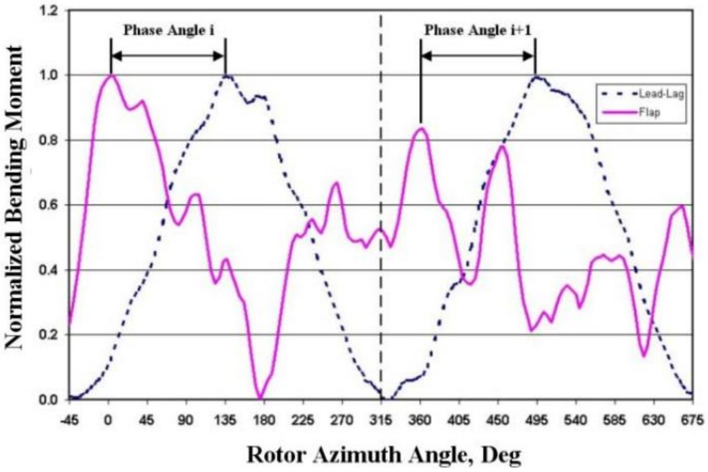

Figure 6.20: Phase angle calculation [74].

Outcomes from the NREL research described in the report [74] show the following:

- The phase angle between flap and lead-lag loading varies widely during turbine operation and can be represented by a Gaussian distribution.
- Constant phase angle simplifications used for blade testing and fatigue analysis are non-conservative with respect to damage accumulation.
- Constant phase angle approximations may conceal blade defects that are introduced by design, manufacturing or material deficiencies.

So not only the phase difference, but also its time fluctuating character decreases fatigue life. The latter can for example be represented by taking the standard deviation of the phase angle variation into account.

6.6.2 Approach to be taken

In above mentioned approach it is clear what time segment to choose for the phase angle calculation: the time of one rotor rotation. Choosing the right time segment is however more complicated by considering combined out-of-phase loading in a tower weld. To determine this time segment, a frequency analysis should be performed. The time series of the stress signals can be represented in the frequency domain with use of a Fast Fourier Transformation. The normal stress frequency with the highest energy will be chosen to determine the time segment length. The time series of the stresses tend to follow harmonic trends and produce clear peaks and valleys. However, both the signals have a strong stochastic character. The resultant stress vector is continual shifting. The phase angle will be determined by the phase angle between the peaks. It's assumed that one segment represents 360 degrees.

6.6.3 Frequency analysis stress signals

The amplitude spectrums of the stresses in the frequency domains for the cut-in, rated and cut-out wind speeds are given in the next graphs.

Cut-in wind speed

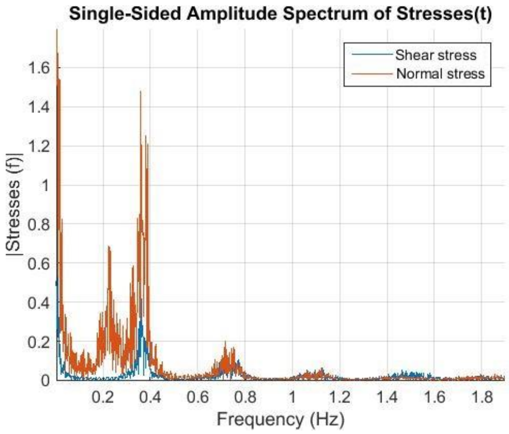

Figure 6.21: BF stresses at cut-in wind speed (3.0m/s).

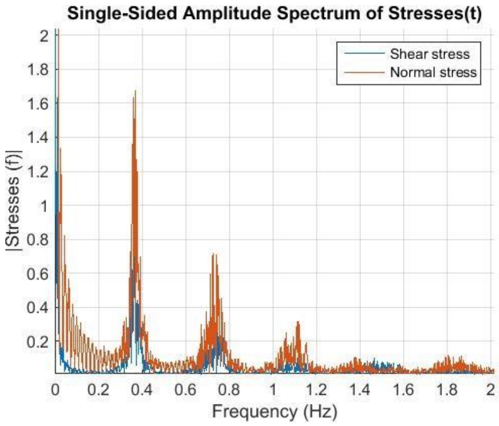

Figure 6.22: UMF stresses at cut-in wind speed (3.0m/s).

At the bottom flange, a peak can be noticed around the first eigenfrequency (0.22 Hz). This makes sense because this peak is caused by the fore-aft moments, which cause the normal stresses in the shell. A peak cannot be seen at the upper middle flange at this frequency, because the normal stresses due to these moments are much smaller here. Both flange positions have peaks around 0.36 Hz, 0.72 Hz and 1.1 Hz in the frequency spectrum. These frequencies represent the 3P, 6P and 9P frequencies (see Section 2.2.2 for an explanation) at cut-in wind speed (6.9 rpm). The peaks at very low frequencies can be explained by the wind loading.

Rated wind speed

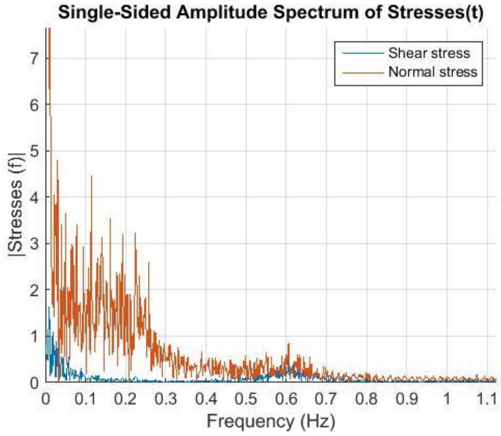

Figure 6.23: BF stresses at rated wind speed (11.4 m/s).

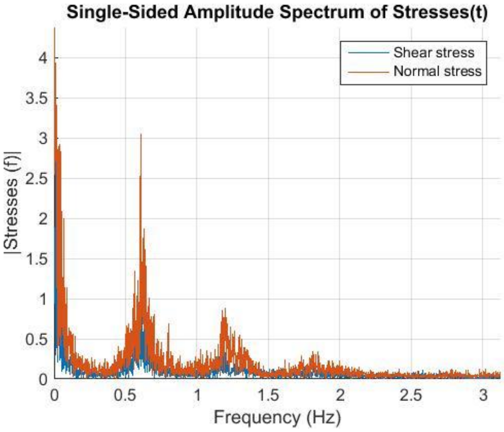

Figure 6.24: UMF stresses at rated wind speed (11.4 m/s).

Rated wind speed is assumed. With 12.1 rpm for rated wind speed, the peaks at the upper middle flange frequency spectrum represent the 3P, 6P and 9P frequencies (0.6 Hz, 1.2 Hz and 1.8 Hz). For the bottom flange, the frequency spectrum is more spread. Peaks around the very low frequencies and the 1P frequency can be noticed.

Cut-out wind speed

Especially excitations around the first frequency can be seen at the bottom flange. The upper middle flange peaks are located at the same locations as for the rated wind speed simulations.

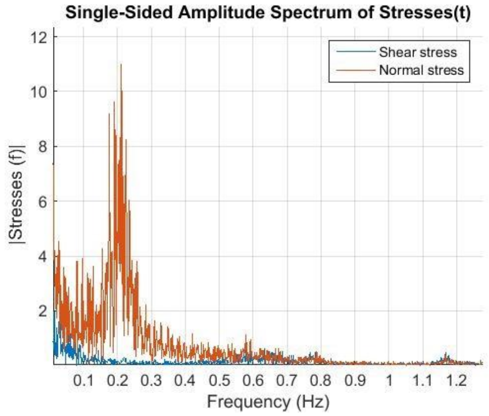

Figure 6.25: BF stresses at cut-out wind speed (25m/s).

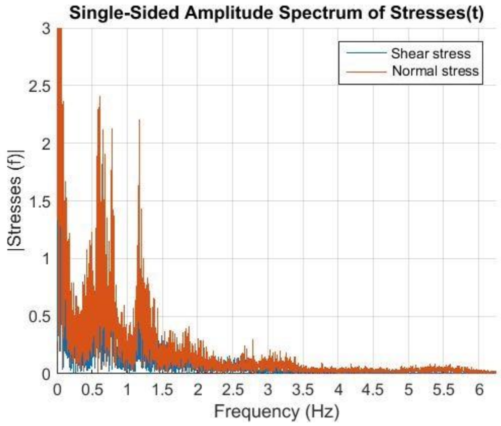

Figure 6.26: UMF stresses at cut-out wind speed (25m/s).

6.6.4 Phase angle

Figure 6.27 shows an example of how the phase differences are calculated in case of a bottom flange in a high wind speed sea state. The time segment is determined by the highest peak in the frequency amplitude spectrum (0.2 Hz, see Figure 6.25). The phase angle will be determined by the phase angle between the peaks. It's assumed that one segment represents 360 degrees.

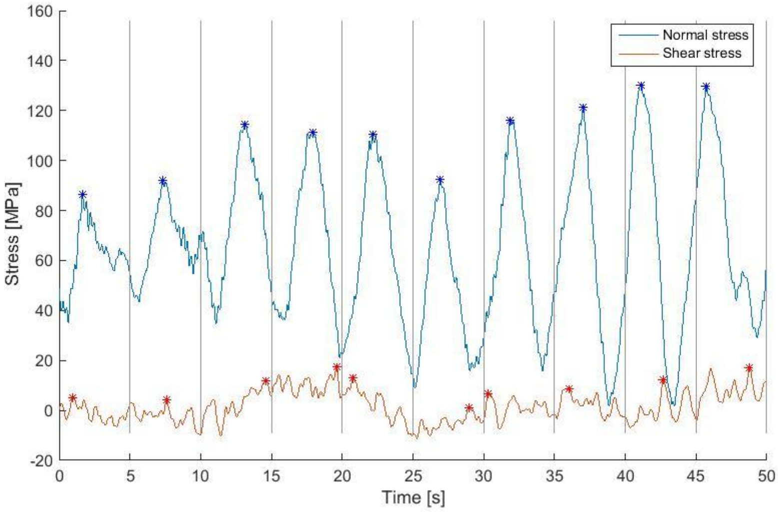

Figure 6.27: Example phase angle calculation normal stress and shear stress.

The figure shows that it's a rough method to establish the phase difference, because the peaks of the shear stresses look quite random. The phase differences will be analyzed in the next sections.

Mean phase angle

A research by Carpinteri [75] suggested taking weight functions into account by calculating the average phase angle. If the principal stress is below a defined fatigue limit, than this weight function becomes 0. When the principal stress is above the fatigue limit, the weight function becomes 1. Furthermore, a second weight function is involved, depending on the slope of the SN-curve. However, in this analysis it's assumed that the total weight function is a constant of 1 because no fatigue limit is defined. Furthermore, the way to determine the phase angle for every time step is quite rough and involving such a detailed weight function would make no sense. The mean phase angle is calculated by just taking the arithmetic average. For the 5MW-NRELT the phase angles are determined for the three considered wind speeds and displayed in histograms in Figure 6.28-Figure 6.29.

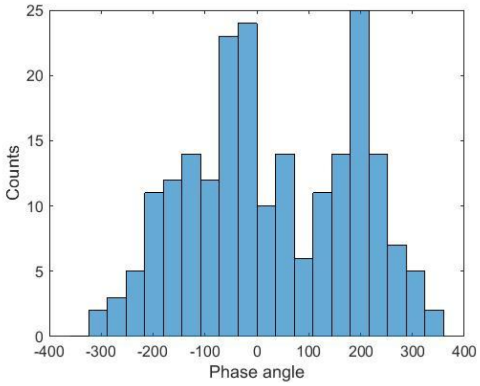

Figure 6.28: Load phase angles at cut-in wind speed (mean=28, freq=0.36 Hz, UMF).

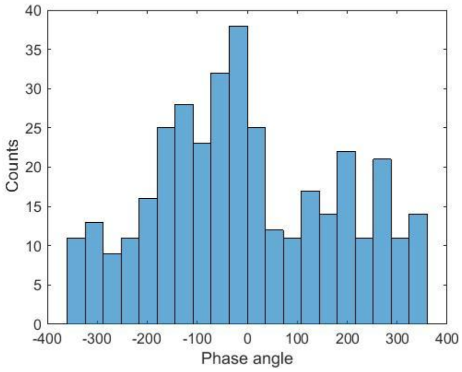

Figure 6.29: Load phase angles at rated wind speed (mean=-2.4, freq=0.61 Hz, UMF)

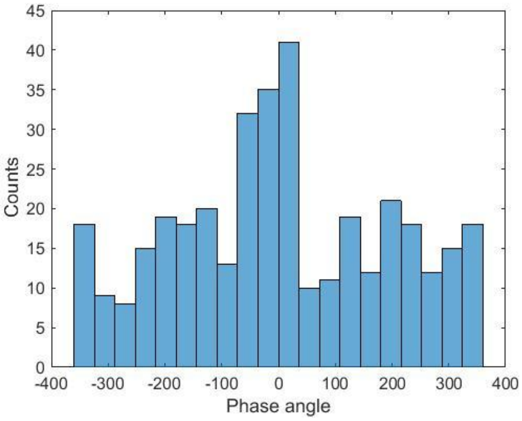

Figure 6.30: Load phase angles at cut-out wind speed (mean=3.0, freq=0.61 Hz, UMF).

The NREL report showed that the phase angle between flap and lead-lag can be represented by a Gaussian distribution. However, in case of a tower weld, Figure 6.28 - Figure 6.30 show that the distributions of the phase angles are quite spread out. This can be explained by the fact that many frequencies are present in the stress signals and hence not one specific frequency is governing. Therefore it's hard to find any relations between the signals.

Influence varying phase angle

Research on wind turbine blades showed [74] that when a phase angle varies over time, up to twice as must damage can take place. This should be taken into account when choosing an appropriate out-of-phase angle.

Conclusion

The EESH results indicate that the out-of-phase angle of the loading is important in fatigue calculation. Analyses showed that it's hard to indicate a governing constant phase angle between the stochastic stress signals in a tower weld. Furthermore, the fatigue life reducing influence of a varying phase angle is not incorporated in the EESH. Therefore, the best guess is to take this implicitly into account by assuming a conservative out-of-phase angle of 90°. This is also recommended by C.M. Sonsino. Therefore, further in this thesis, it's assumed that combined out-of-phase loading has a phase angle of 90°.

6.7 The EESH in perspective

The EESH is explained and damage calculations are done. The purpose of this section is to place the hypothesis in perspective, before discussing the final results. A short view will be given on how the EESH handles with the fatigue aspects described in the theoretical background:

- Fatigue scales
- Fracture mechanics
- Proportional vs. non-proportional loading
- Fatigue models
- Damage accumulation
- Time domain vs. frequency domain fatigue calculations

Furthermore, some suggestions will be made on how these aspects possibly can be incorporated in improved future fatigue models.

Fatigue scales

The used EESH is based only on the macro scale. The ideal fatigue life prediction model links the parameters from the different scales with each other and takes the phenomena from different scales into account. It is important to find a balance in taking as much relevant parameters as possible into account and computational efforts.

Fracture mechanics

Fracture mechanics gives a good insight how cracks develop. The insights of the fatigue stage 1 phase is incorporated in the EESH model with use of the effective damage sum, which represents the interaction of shear stresses in various interference planes which initiate dislocations.

Proportional vs. non-proportional loading

Future fatigue models should incorporate a correction factor for non-proportional loading and additional hardening, as suggested by [30] (F_{cor}, Section 2.1.6.3). This factor can be compared with the factors which are applied on the in-phase equivalent stress of the EESH (effective damage sum ratio and the square root term of Equation 6.8), in order to get the out-of-phase stress. Including material sensitivity of the influence of combined out-of-phase loading would be an improvement for the EESH.

Fatigue models

The key problem in evaluating fatigue damage is the necessity of using multiaxial fatigue damage criteria which are based on the loading history and material [22]. Different models are proposed, but yet there is no universally accepted method[76][77][78]. Non-proportionality cannot be described by strain based models. This makes clear that a future fatigue model should include more than only strains. Critical plane models, which are physics based and consider specific planes with maximum fatigue damage, have been found to be generally more accurate and applicable to both proportional and non-proportional loadings. Those critical plane models can be based on maximum principal strain/stress plane or maximum shear strains/stress [79]. Non-proportional hardening is reflected by additional stress responses, so stress components should always be used in the prediction of the fatigue life in multiaxial loading situations. The EESH is a stress and critical plane based fatigue model.

Damage accumulation models

Miner's rule is most used damage accumulations model because of its simplicity. It's also used by the EESH. However, this model has some disadvantages:

- The critical damage that causes failures is not a fixed value. It follows a certain distribution which is not included in Miner's rule.
- A simple linear life-stress relationship is assumed. This may not be true in many real-world applications [80].
- A uniaxial stress state is assumed.

First drawbacks of Miner's rule can be overcome by using probabilistic models. The Inverse Power Law-Weibull Model [80] is an example. In this way the probabilistic nature that is required for the proper analysis of many fatigue failures can be included.

The second drawback can be overcome by using a non-linear accumulation model.

$$D = \sum_i (\frac{n_i}{N_i})^k \quad \text{Equation 6.19}$$

However, to determine the appropriate factor k is difficult and material and loading dependent.

The last drawback can be compensated by incorporating the interaction between normal stresses and shear stresses. This can for example be done with the so called Modified Gough-Pollard algorithm of Equation 6.5. The hypothesis comprises a physically found consideration of shear and normal stress interaction.

Frequency domain fatigue calculations

Fatigue calculations in the frequency domain for monopile foundations within SWP show 3-7% difference in comparison with the time domain calculations in BHawC. The frequency method has shown the significant beneficial effects in terms of computational efforts. It is convenient to use for application in the conceptual design phase, however for detailed calculation the non-linearities should be included, which is until now only possible in time domain calculations. The EESH is based on the time domain.

Conclusion

Many parameters play a role within the fatigue life analysis of structures. The following tables give a summary of important fatigue-life prediction parameters. A suitable fatigue model should consider many of these parameters. The parameters which are taken into account by the EESH are marked with an asterisk*.

Scale
Micro
Meso
Macro*

Table 6.8: Different scales to consider.

Loading
Stress amplitudes*
Mean stresses
Strain amplitude
Loading phase angle*
Variable loading phase angle
Type of stress/strain (nominal*, hot-spot, structural, local)
Difference between compressive and tensional stresses
Amplitude ratios
Equivalent stress/strain (Nominal, Von Mises, Tresca, EESH*)

Table 6.9: Different loading parameters to consider.

Material parameters
Shear modulus
Elasticity modulus
Ductility
Endurance limit of the material
Fracture stress
Corrosion effect
Hardening effect*

Table 6.10: Different material parameters to consider.

Weld geometry
Weld shape*
Effect of misalignment
Thickness effect

Table 6.11: Different weld geometry parameters to consider.

Damage accumulation
Loading cycle counting method (peak, level crossing, range, rainflow counting*)
Damage model (Miner's rule*, probabilistic model, Gough-Pollard algorithm)
Critical plane (highest damage*, highest variance)
SN-curve (normal*, modified)

Table 6.12: Different damage accumulation parameter to consider.

Domain
Time*
Frequency

Table 6.13: Domain possibilities.

The ideal situation will be to develop one uniform model which covers all materials and loading situations. However, by taking all relevant fatigue parameters (at different scales) into account, the model will become complicated and computational demanding. For engineering purposes this is not desired; such a complicated model is not to be expected in the near future.

However, fatigue life prediction software is in development. The commercial software FEMFAT [81] (Finite Element Method Fatigue) performs fatigue analyses in combination with finite element systems considering a multitude of fatigue influences including stress gradient, mean stress and various influences from production processes. With increasing computational power, such software can become more and more of interest. However, this software still makes use of assumptions and theoretical models taking the different scales on which fatigue can be considered should be taken into account. This can be done by multiscale modeling.

Fracture mechanics analysis is useful for calculation of residual life when cracks have already developed. However, for practical engineering purposes of large structures, fatigue calculations rely on empirical SN-curves. Research showed that the out-of-phase angle of the loading decreases the fatigue life. New fatigue models try to incorporate this angle with use of modification of the stresses by a non-proportionality and additional hardening factor. However, for stochastic signals, a load angle has to be assumed since it is hard to obtain. Tests should be performed how to deal with this matter. A combination of critical plane based and stress based models have been found to be generally most successful in prediction fatigue. They are physics based and are able to consider the effect of out-of-phase loading. Therefore, an extension of these models is expected to be successful.

The frequency based fatigue models are not expected to give accurate fatigue life predictions in near future. The non-linerarities and out-of-phase loading cannot be represented well enough in the frequency domain. However, these methods can be used to give an initial estimate for the fatigue loads.

The EESH incorporates the out-of-phase angle, but as can be seen from above tables, many parameters are not included. The current version of the EESH is only valid for specific loading conditions and materials. A generalization of the hypothesis can only be done with use of more experiments. Many research attempts are done on the multiaxial fatigue problem nowadays and progress in understanding the problem is expected with improved experimental equipment (Section 2.1.6).

6.8 Results damage calculations

The EESH is tried to be placed in perspective in the previous section in order to be better be able to discuss the results obtained under the EESH model. Table 6.14 and Table 6.15 present the following ratios:

- The ratio of the damage according combined in-phase loading to the damage according uniaxial nominal stress loading

- The ratio of the damage according combined 90° out-of-phase loading to the damage according uniaxial nominal stress loading

Wind speed	**Flange**	**Damage ratio combined in-phase loading (Gough-Pollard)**	**Damage ratio 90° combined out-of-phase loading (EESH)**
Cut-in (3m/s)	BF	1.16	2.20
	UMF	1.50	4.72
Rated (11m/s)	BF	1.20	2.51
	UMF	1.54	5.33
Cut-out (25m/s)	BF	1.16	1.26
	UMF	1.36	3.09

Table 6.14: 5MW-NRELT damage ratios.

Wind speed	**Flange**	**Damage ratio combined in-phase loading (Gough-Pollard)**	**Damage ratio 90° combined out-of-phase loading (EESH)**
Cut-in (3m/s)	BF	1.06	1.84
	UMF	1.10	2.11
Rated (11m/s)	BF	1.11	2.69
	UMF	1.18	3.63
Cut-out (25m/s)	BF	1.09	1.69
	UMF	1.12	2.23

Table 6.15: 6MW-SWT damage ratios.

Damage - flange dependent

The EESH damage ratios for the upper middle flange are higher than the damage ratios for the bottom flange, i.e. the shear loading has a larger influence on the fatigue damage at the upper middle flange welds than on the bottom flange welds. This is caused by the fact that the ratio of the shear stress range to the normal stress range is higher for the upper middle flange than for the bottom flange, see Table 6.1 and Table 6.2.

Damage – load situation dependent

At rated wind speed the EESH damage ratios are the highest; i.e. the influence of the combined loading is most severe at this wind speed.

Damage- tower geometry dependent

The influence of the shear stress on the upper middle flange is less severe for the 6MW-SWT than for the 5MW-NRELT. For the latter, the diameter of the tower decreases from the bottom flange till the upper flange, which is not the case for the 6MW-SWT as can be seen Appendix D. The torque remains constant over height (see Appendix E) and hence the influence of shear stress, caused by the torque, becomes larger. Therefore, for the same wind speed simulations, the damage ratios for the upper middle flanges are higher for the 5MW-NRELT than for the 6MW-SWT.

Damage-effective damage sum ratio dependent

The effective damage sum ratio $\frac{EDS\,(\delta)}{EDS\,(\delta=0°)}$ varies between 1.08 and 1.17. The influence of shifting the in-phase fictional stress into an out-of-phase stress is larger (higher ratio) for the upper middle flange than for the bottom flange at the same wind speed. This is to be expected when analyzing Table 6.1 and Table 6.2, the amplitude ratio of the shear stress to the normal stress is lower at the bottom flange than at the upper middle flange.

Damage-out of phase angle dependent

The more out-of-phase the shear stress loading (till 90°), the more severe the calculated damage according the EESH. The combined out-of-phase loading according the EESH causes an increase of damage with a factor up to 3.5 in comparison with the damage calculated with combined in-phase loading (Table 6.7). The square root factor in the equivalent stress calculation from Equation 6.10 is strongly dependent on the phase angle δ, see Table 6.16.

$\boldsymbol{\delta}$	$\mathbf{45°}$	$\mathbf{90°}$
$\sqrt{\left(SM \exp\left(1-\left(\frac{\delta-90°}{90°}\right)^2\right)\right)}$	1.56	1.77

Table 6.16: Dependency of the square root factor on the phase angle δ in tower weld (SM=1.15).

The equivalent stress is amplified with the square root factor as indicated in Table 6.16, independent of the magnitude of the shear stress. This cannot be correct in reality, because when very little shear stress is involved, no extra damage will take place and no amplification should be applied. However, this is not the case for the EESH. This suggests that the EESH should only be applied when the shear stress amplitude is relatively large enough to contribute to the fatigue damage. This matter is discussed with C.M. Sonsino and the result of the correspondence with him indicates that the EESH as presented in the aforementioned paper cannot be generalized at all, see Section 6.9.

6.9 Results discussion with C.M. Sonsino

C.M. Sonsino was so kind to discuss some of the obtained results. Especially the square root factor in the EESH equivalent stress of Equation 6.8 was a point of discussion. I indicated that I found it remarkable that the square root factor amplifies the equivalent stress independent of the shear stress amplitude. He explained that "the root factor was a nice idea for a very difficult phenomenon (volume effect), nice for research but difficult for practice. Therefore, today, when I make calculations, I apply a simplification, I consider only the effective damage sum ratio $\frac{EDS\,(\delta=90°)}{EDS\,(\delta=0°)}$. I apply the same SN-curves for all the multiaxial cases".

In an earlier phase of my research, I received from C.M. Sonsino a more recent (2010) publication of the Fraunhofer Institute [82] in which the EESH is presented without the square root factor. Omitting this square root factor was back then explained by the author with "this is a simplified alternative for practioners" [83]. I wrongly concluded from this that the original EESH would be a more complicated but more accurate method.

However, now it's clear that the original EESH (with square root factor) as presented in this thesis is not believed to be workable for practical fatigue calculations.

The conclusion is that instead of the presented EESH, a simplification is used by omitting the square root factor and assuming the same SN-curve for both the combined in-phase loading and combined out-of-phase loading. Because the global SN-curve is used, the calculated values are also the real damage values. In this way the calculation according the Gough-Pollard algorithm can be avoided. Calculations according the simplified EESH will be presented in Section 6.10. The difference in the results of the different considered models (Gough-Pollard, original EESH and simplified EESH) and the advantages and disadvantages of the considered models are discussed in Section 6.11.

6.10 Out-of-phase damage ratios according simplified EESH

The simplified EESH, as discussed in Section 6.9, is presented in Equation 6.20.

$$\Delta\bar{\sigma}_{eq}(\delta) = \Delta\bar{\sigma}_{eq}(\delta = 0°) \cdot \frac{EDS\ (\delta)}{EDS\ (\delta = 0°\ )} \qquad \text{Equation 6.20}$$

The damage ratios are presented in Table 6.17 and Table 6.18. The same SN-curves are assumed for the combined in-phase and out-of-phase loading. The ratios will be discussed in Section 6.11.

Wind speed	**Flange**	**Damage ratio combined 90° out-of-phase loading simplified EESH**
Cut-in (3m/s)	BF	1.64
	UMF	2.07
Rated (11m/s)	BF	1.73
	UMF	3.33
Cut-out (25m/s)	BF	1.34
	UMF	1.78

Table 6.17: Simplified EESH damage ratios 6MW-SWT.

Wind speed	**Flange**	**Damage ratio combined 90° out-of-phase loading simplified EESH**
Cut-in (3m/s)	BF	1.65
	UMF	3.56
Rated (12m/s)	BF	2.07
	UMF	4.38
Cut-out (28m/s)	BF	1.47
	UMF	2.56

Table 6.18: Simplified EESH damage ratios 5MW-NRELT.

6.11 Conclusions

Damage ratios

Simulations show that in tower welds out-of-phase shear stresses are present with amplitudes larger than 15% of the normal stress amplitude. Therefore, according the IIW [21], shear stresses should be taken into account.

The ratios of the damages calculated with the discussed models to the damages calculated with the conventional uniaxial normal stress method are summarized in Table 6.19 and Table 6.20. For the combined out-of-phase loaded situations the phase angle is assumed to be 90°. In this way the fatigue life reducing influence of varying phase angle is tried to be incorporated.

Wind speed	Flange	Damage ratio combined in-phase loading (Gough-Pollard)	Damage ratio combined 90° out-of-phase loading (original EESH)	Damage ratio combined 90° out-of-phase loading (simplified EESH)
Cut-in (3m/s)	BF	1.06	1.84	1.64
	UMF	1.10	2.11	2.07
Rated (11m/s)	BF	1.11	2.69	1.73
	UMF	1.18	3.63	3.33
Cut-out (25m/s)	BF	1.09	1.69	1.34
	UMF	1.12	2.23	1.78

Table 6.19: Damage ratios considered fatigue models 6MW-SWT.

Wind speed	Flange	Damage ratio combined in-phase loading (Gough-Pollard)	Damage ratio combined 90° out-of-phase loading (original EESH)	Damage ratio combined 90° out-of-phase loading (simplified EESH)
Cut-in (3m/s)	BF	1.16	2.20	1.65
	UMF	1.50	4.72	3.56
Rated (11m/s)	BF	1.20	2.51	2.07
	UMF	1.54	5.33	4.38
Cut-out (25m/s)	BF	1.16	1.26	1.47
	UMF	1.36	3.09	2.56

Table 6.20: Damage ratios considered fatigue models 5MW-NRELT.

The calculated damages are dependent on the considered flange location, wind speed and wind turbine type. Combined out-of-phase loading causes more damage than in-phase loading. The upper middle flange is more influenced by combined loading than the bottom flange. Out of the considered simulations, the simulation at rated wind speed shows the highest damage increase due to taking the shear stress into account. The ratio of maximum shear stress amplitude and maximum normal stress amplitude is for this simulation the highest. A comparison between the considered wind turbines with different tower geometries and control systems show significant differences in the influence of the shear stress on the damage.

Safety factors

This section shows what safety factor should be applied on the normal stress in the uniaxial nominal stress fatigue calculations in order to cover the calculated additional damage due to combined out-of-phase loading according the considered multiaxial fatigue models. The calculations of the required safety factors are done with the damage ratio values of Table 6.19 and Table 6.20. A SN-curve with a slope of 5 is assumed, so the safety factor can be calculated with the damage ratio value to the power 1/5. It is concluded that the combined loading in tower welds is out-of-phase. Therefore an allowable damage sum of 0.5 should be assumed for the Gough-Pollard algorithm (instead of 1.0 for combined in-phase loading), as described in Section 6.3. This means that the Gough–Pollard damage ratios of the combined in-phase loading as stated in Table 6.19 and Table 6.20 have to be multiplied with a factor 2 to incorporate the out-of-phase influence. Table 6.21 and Table 6.22 show the required safety factors according the considered models.

Wind speed	**Flange**	**Safety factor combined out-of-phase loading (Gough-Pollard)**	**Safety factor combined 90° out-of-phase loading (original EESH)**	**Safety factor combined 90° out-of-phase loading (simplified EESH)**
Cut-in (3m/s)	BF	1.16	1.13	1.10
	UMF	1.17	1.16	1.16
Rated (11m/s)	BF	1.17	1.22	1.12
	UMF	1.19	1.29	1.27
Cut-out (25m/s)	BF	1.17	1.11	1.06
	UMF	1.18	1.17	1.12

Table 6.21: Required safety factors 6MW-SWT.

Wind speed	**Flange**	**Safety factor combined out-of-phase loading (Gough-Pollard)**	**Safety factor combined 90° out-of-phase loading (original EESH)**	**Safety factor combined 90° out-of-phase loading (simplified EESH)**
Cut-in (3m/s)	BF	1.18	1.17	1.10
	UMF	1.25	1.36	1.29
Rated (11m/s)	BF	1.19	1.20	1.16
	UMF	1.25	1.40	1.35
Cut-out (25m/s)	BF	1.18	1.04	1.08
	UMF	1.22	1.25	1.21

Table 6.22: Required safety factors 5MW-NRELT.

The load safety factors used nowadays lay between 1.1 and 1.4, depending on the design code to apply. Table 6.21 and Table 6.22 show that the required safety factors vary between 1.16 and 1.40.

This means that according these models the application of a load safety factor lower than 1.4 may result in unsafe fatigue design.

Gough-Pollard algorithm

The combined in-phase loading damage calculation according the Gough-Pollard algorithm is simple to perform. Different SN-curves are used for the normal stress and shear stress. In this way the algorithm can distinct between damage caused by the shear stresses and normal stress. According the IIW, the algorithm can also be used for combined out-of-phase loaded situations by assuming half the allowable damage sum in comparison with the in-phase situation. An improvement suggestion would be to let the allowable damage sum of the Gough-Pollard algorithm depend on the out-of-phase angle, as both the EESH models suggest

Original EESH

The EESH is a stress hypothesis that takes the amplitudes of the shear loading into account and its out-of-phase angle with the normal stress component. This is done by amplification of the in-phase equivalent stress by the so called square root factor and the effective damage sum ratio.

The EESH applied on the tower welds shows similar results regarding the fatigue decreasing influence out-of-phase loading as presented in the paper by C.M. Sonsino [24].

The hypothesis has the potential to be applicable on many different situations because of the stress concentrations factors involved. Furthermore, the interaction between the shear stresses in the different planes is represented by the effective damage sum ratio. In this way the hardening of the material due to activation of different slip planes can be represented. However, the original EESH has its drawbacks.

The first amplification factor of the EESH, the square root factor, is strongly dependent on the phase angle. The value of this angle is hard to determine for the stochastic stress signals in a tower weld. Furthermore, this factor is independent of the magnitude of the shear stress. This cannot be correct in reality, because when there is very little shear stress, no amplification due to shear stress will take place.

The second amplification factor of the EESH, the effective damage sum ratio, represents the shear stress interaction in different planes. It is dependent on the shear stress magnitude and does not amplify the in-phase equivalent stress in case no shear stress is present. However, the effective damage sum ratio is hard to obtain for two stochastic signals. Two fictional one-frequency signals have to be created with use of a time consuming iterative process. Besides that, it’s questionable how accurate this ratio is, since it’s assumed that the secondary stress component has the same frequency as the primary stress, which differs in case of the considered simulations up to 40%. An improvement suggestion is to apply a frequency correction when the real frequency of the secondary signal differs a lot from the most damaging signal. Furthermore, a certain distribution for amplitudes of the secondary signal has to be assumed to create the single frequency fictional signals which generate the same effective damage sum and critical plane as the original signals. This can be realized with different distributions of the secondary fictional signal, giving different effective damage sum ratios.

Above drawbacks summarize why the EESH is not suitable for practical fatigue calculations of tower welds.

Simplified EESH

To overcome the difficulties with the square root factor, a simplified EESH version is introduced that does not include this factor anymore.

The simplified version of the EESH has some advantages over the original version. The same SN-curves can be used for combined in-phase and out-of-phase loading. This is the same SN-curve as used for the conventional uniaxial method for normal stresses. Therefore, the damage values can directly be compared with the damages according the conventional uniaxial method. No empirical SN-curve for combined loading is necessary. The shear stress interaction is still included by the effective damage sum ratio. However, calculating the effective damage sum ratio has still the same disadvantages as mentioned before. Furthermore, the simplified EESH does not have the initial main advantage of the original EESH: the phase angle is not included anymore. Besides that, the SCF's are omitted.

Final conclusion

It can be concluded that shear stresses should be taken into account in the fatigue calculations of tower welds. If one is willing to take shear stress and its phase angle into account for practical fatigue calculations, of the considered methods it is recommended to use the Gough-Pollard algorithm with an allowable damage sum depending on the phase angle. Experiments should be performed in order to show how this relation will look like. For now it's assumed that allowing a damage sum of 0.5 is sufficient to incorporate the out-of-phase influence of the shear stress, as stated in the IIW document [21]. Therefore, the calculated required load safety factors according the Gough-Pollard method will be assumed to be most reliable.

The highest required safety factor according this algorithm is 1.25 for the upper middle flange at rated wind speed for the 5MW-NRELT. A load safety factor of 1.19 is required in case of a bottom flange weld. These safety factors should be used when one is trying to incorporate the additional damage due to combined out-of-phase loading in the conventional uniaxial method. However, usage of correct multiaxial fatigue models instead of safety factors increases the accuracy of fatigue life predictions.

Chapter 7

7 Conclusions and recommendations

This thesis suggests different state-of-the-art design methods for wind turbine towers in order to reduce the costs of offshore wind energy. The conclusions and recommendations are ordered by chapter, as each chapter in this thesis represents a different tower design aspect.

7.1 Conclusions

Chapter 1: Introduction

Wind energy plays an important role for the European renewable energy targets for 2020. Offshore wind energy has many advantage, however the costs per MWh should be reduced in order to be competitive with conventional energy generation. The tower contributes significantly to the cost of a wind turbine (15%), which means that improved tower design can lead to noteworthy cost reductions.

Chapter 2: Theoretical background

As wind turbine components are subjected to highly dynamical loading, fatigue of materials is important to consider in the design. Many parameters play a role in fatigue design of structures. The ideal situation is to develop one uniform fatigue model that covers all material types and loading situations. However, by taking all relevant fatigue parameters (at different scales) into account, the model will become unnecessarily complicated and computational demanding. For engineering purposes this is not desired; such a complicated model for practical calculations is not to be expected in the near future. Fracture mechanics analyses are useful for calculation of residual life when cracks have already developed. However, for practical engineering purposes of large structures, fatigue calculations are done with empirical SN-curves. A combination of critical plane based and stress based models is found to be generally most successful in predicting fatigue life. These models are physics based and are able to take the effect of out-of-phase loading into account. Therefore, an extension of these models is expected to be most successful. Frequency based fatigue models have much potential, but are expected to be only used for initial designs in the near future.

For tower design, different design constraints should be taken into account: local and global buckling, modal frequencies, and fatigue damage.

Flange connections can be analyzed by dividing the flange into single bolt segments. Generally accepted analytical models exist to perform ULS and FLS calculations for flange connections.

Chapter 3: Flange loading and influence of flange design on global dynamical behavior

In the considered ULS simulations of the 5MW-NRELT, the bottom flange has to withstand the highest moments (6 times higher than the top flange) and forces (4 times higher than the top flange). The loading decreases with higher flange locations. Therefore, the maximum fatigue damage occurs at the bottom of the tower. The tower top flange has an expected fatigue life that is more than 60 times larger than the bottom flange.

Modeling the flanges (mass, geometry and stiffness) will lower the first two eigenfrequencies (bending mode) by less than 1%. The mode shapes do not change and the differences in loads (+0.5%) and displacements (+2.5%) are found to be insignificant. The effect of geometry and stiffness is not contributing as much as modeling the mass. Modeling the flanges as point masses is therefore sufficient to represent the flanges in aeroelastic codes.

A constraint damping layer is proposed to increase the tower damping. In this way the fatigue loads on the tower can be reduced. The layer should only be laid partly between the flanges; otherwise the bolt share of load becomes too high and consequently the fatigue loads on the bolts.

Chapter 4: Improvements in flange design

With use of 30 6MW-SWT projects optimization and standardization cases are considered. The improved flange design optimization method (with cost performance function) realizes a reduction in flange costs of more than 2.5% in comparison with the optimization method used nowadays within SWP.

Flange standardization is beneficial for the costs of handling equipment and tower internals, as project specific design and certification of these components can be omitted. Other advantages of flange standardization are risk mitigation and supply chain benefits. The cost benefits of flange standardization are obvious, however not quantified.

Standardization of the flanges with a fixed bolt pattern causes a costs increase of almost 3% for the flanges. Additionally standardizing the flange width (on the maximum value of the considered projects) yields a cost increase of 7% in comparison with the optimized case.

Chapter 5: Sector based fatigue design

A more detailed fatigue design of tower welds is possible if every sector on the circumference will have its own specific SN-curve and SCF, depending on the local geometry, instead of assuming the most conservative SN-curve and SCF on the whole circumference. Five SWP projects show that the equivalent fatigue loads differ up to 12% between the different sectors on the circumference. This means that by directing the door frame in the least loaded direction and taking these loads as governing (instead of the highest equivalent loads) load reduction of 12% can be realized. Consequently, for fatigue driven designs, the total tower mass can be reduced up to 6%.

Chapter 6: Multiaxial fatigue in tower design

Simulations show that shear stresses contribute significantly to the stress state within tower welds. For the upper middle flange is the amplitude ratio shear stress to normal stress higher than for the bottom flange. Shear stresses should be taken into account for accurate fatigue calculations.

A multiaxial fatigue model, the EESH, is applied on the tower welds and shows similar results concerning the fatigue decreasing influence of out-of-phase loading (up to a factor 4 in comparison with combined in-phase loading) as presented by C.M. Sonsino [24]. The EESH calculates the highest increase in damage for higher located flanges and at rated wind speed simulations. The EESH makes use of the effective damage sum ratio, which is a factor to incorporate the influence of the shear stresses interaction in different planes. Another factor within the EESH, the square root factor, incorporates the phase angle and SCFs for bending and torsion.

The original EESH is found to be a promising model to use for fatigue calculations since it takes SCFs, the phase angle and shear stress interaction into account. However, the EESH is not as practical as presented in literature. The square root factor amplifies the equivalent stress independent of the shear stress magnitude, which cannot be the case in reality. Furthermore, for stochastic stresses the calculation of the effective damage sum ratio is computational demanding and does not give a unique solution. Different SN-curves have to be used to compare the combined in-phase and out-of-phase situation. The absolute damage values have to be determined with SN-curves based on combined loading, which are to be determined experimentally.

In the simplified EESH, the successor of the original EESH, the square root factor is omitted. The model does not amplify the equivalent stress if no shear stress is involved. However, the SCFs and phase angle are not included in the model anymore, which is the main added value of the original EESH model in comparison with other multiaxial fatigue models.

Another considered fatigue model that takes shear stress into account is the Gough-Pollard algorithm recommended by the International Institute of Welding [21]. An improvement suggestion would be to let the allowable damage sum of the Gough-Pollard algorithm depend on the out-of-phase angle. Besides that the Gough-Pollard algorithm is easier to apply than the simplified EESH, another advantage of the algorithm is that it can distinct between damage caused by the shear stress and normal stress due to the different SN-curves to use. The Gough-Pollard algorithm is recommended over the EESH models for multiaxial fatigue calculations.

According to the above multiaxial fatigue models, load safety factors between 1.16 and 1.40 are required when evaluating fatigue life in tower welds with the conventional uniaxial method. In this way the additional damage due to combined out-of-phase loading is incorporated in the fatigue life prediction. However, usage of correct multiaxial fatigue models instead of safety factors increases the accuracy of fatigue life predictions.

7.2 Recommendations

Chapter 1: Introduction

- More research on the costs aspects of offshore wind energy should be performed in order to reduce the costs per MWh offshore wind energy.

Chapter 2: Theoretical background

- More research should be performed on investigating the influence of combined out-of-phase loading and how to incorporate it in practical fatigue models.

Chapter 3: Flange loading and influence of flange design on global dynamical behavior

- The influence of a damping layer on the failure modes should be investigated. Furthermore, the effect on the relation between bolt stress and shell stress should be validated. The damping influence of different kind of materials can be investigated with FEM. This model can be used to identify the damping influence of the layer to the total damping of the tower. The costs of such a layer and extra machining of the flanges should be considered when introducing a constraint damping layer between flanges. It can also be of interest to investigate whether such a constraint damping layer is able to compensate flange imperfections.

Chapter 4: Improvements in flange design

- The mentioned benefits of flange standardization (standardization of handling equipment and tower internals, supply chain benefits, risk mitigation) should be quantified in order to evaluate if standardization is financially beneficial.
- The transport load case is often design driving in flange design within SWP and currently assessed conservatively. This load case should be assessed in more detail.
- Flange load reduction during the transport load case should be investigated (usage of transport frames or cradles).
- The influence of an unequal bolt pattern on the flange and tower loading should be investigated as it could be an alternative for flange standardization.

Chapter 5: Sector based fatigue design

- A study should be performed if the applied environmental prediction models are accurate enough to predict the direction of the loads over a lifetime of 25 years.

Chapter 6: Multiaxial fatigue in tower design

- Multiaxial tests (for example with use of multiaxial high frequency equipment) should be performed to generalize multiaxial models. Research should be done on finding a possible relation between the shear stress-normal stress ratio, phase angle and allowable damage.

Bibliography

[1] Siemens, "Internal information from Siemens Wind Power," 2015.

[2] EWEA, "European Wind Energy Association: Wind in power, 2014 European statistics," 2013.

[3] EWEA, "European Wind Energy Association: The economics of wind energy," 2009.

[4] UKRAB, "UK Renewables Advisory Board: Value breakdown for the offshore wind sector," 2010.

[5] R. Haghi, T. Ashuri, P. van der Valk and D. Molenaar, "Integrated Multidisciplinary Optimization of Offshore Support Structures," *Journal of Physics,* vol. Conference Series 555, p. 11, 2012.

[6] M. Kuehn, "Dynamics and design optimisation of offshore wind energy conversion systems," DUWIND Delft University Wind Energy Research Institute , 2001.

[7] L. Fingersh, "Wind Turbine Design Cost and Scaling Model," National Renewable Energy Laboratory, 2006.

[8] X. Chen, Q. Gao and X. Sun, "Low-cycle fatigue under non-proportional loading," *Fatigue fracture Engineering Material Structures,* 1996.

[9] T. Anderson, Fracture Mechanics; fundamentals and applications (third edition), Taylor and Francis, 2005.

[10] E. Haibach, The Welding Institute Conference on fatigue of welded structures, Brighton, 1970.

[11] M. O. Hansen, "Aerodynamics of wind turbines," *Earthscan ,* 2008.

[12] S. Berge, "Material from course TMR4200 "Fatigue of materials"," NTNU, Trondheim, 2000.

[13] Papadopoulos and Ioannis, "A comparative study of multiaxial high-cycle fatigue criteria for metals," *Elsevier,* vol. 19, no. 3, 2006.

[14] P. Gumbsch, "An atomistic study of brittle fracture: Towards explicit failure criteria from atomistic modeling," *Journal of material research,* vol. 10, no. 11, pp. 2897-2907, 1995.

[15] J. Ge and Y. Sun, "Fatigue life estimation under multiaxial random loading by means of the equivalent Lemaitre stress and multiaxial S–N curve methods.," *International Journal of Fatigue,* vol. 79, pp. 65-74, 2015.

[16] H.-J. Shen and W.-L. Guo, "Relations between the SN eN and da/dan curves of materials," *The open Mechanical Engineering Journal,* p. 2009.

[17] C. Thorwald and G. Tipple, "Using the Failure Assessment Diagram Method with Fatgiue Crack Growth to Determine Leak-before-Rupture," in *SIMULIA customer Conference*, 2012.

[18] J. William and D. Callister, Materials science and engineering, Wiley, 2011.

[19] Y. Jiang, O. Hertel and M. Vormwald, "An experimental evaluation of three critical plane multiaxial fatigue criteria," *International journal of fatigue,* vol. 29, pp. 1490-1502, 2007.

[20] J. Yung, "Predicting the fatigue life of welds under combined bending and torsion," *Mechanical Engineering Publications,* pp. 53-69, 1989.

[21] IIW, "International Institute of Welding: Recommendations for fatigue design of welded joints and components," 2008.

[22] J. Li and Z.-p. Zhang, "Multiaxial fatigue life prediction for various metallic materials based on the critcal plane approach," *International journal of fatigue,* 2011.

[23] M. Kaminski, "Material from course OE4631 "Fatigue and Fracture in Marine Structures"," Techinical University of Delft, Delft, 2014.

[24] C. Sonsino and M. Kueppers, "Multiaxial fatigue of welded joints under constant and variable amplitude loadings," *Fatigue Fract Engng Mater Struct,* vol. 24, pp. 309-327, 2001.

[25] R. Mott, Applied Strength of Materials, New Jersey, USA: Person Prentice Hall, 2008.

[26] A. Fatemi, "Multiaxial fatigue," *University of Toledo.*

[27] Benasciutti, "Basic principles of spectral multiaxial fatigue analysis," *Elsevier,* vol. 34, no. 42, 2015.

[28] M. Kaminski and P. van Lieshout, "4D Fatigue, presentation about the hexapod, initial design," TUDelft, 2014.

[29] T. Itoh, M. Sakane, M. Ohnami and D. Socie, "Non-proportional low cycle fatigue criterion for

type 304 stainless steel.," *J. Eng Mater Technol,* 1995.

[30] Li and Jiang, "A new approach of fatigue life prediciition for metallic materials under multiaxial loading," 2015.

[31] M. Zaaijer, "Material from course OE5662 "Offshore Wind Farm Design"," Technical University of Delft, Delft, 2008.

[32] J. van der Tempel, "Design of support structures for offshore wind turbines," 2006.

[33] D. Benasciutti, "Spectral methods for lifetime prediction under wide-band stationary random processes," *International journal of fatigue,* vol. 27, pp. 867-877, 2005.

[34] R. Tovo, "Cycle distribution and fatigue damage under broad-band random loading," *International Journal of Fatigue,* vol. 24, no. 11, pp. 1137-1147, 2002.

[35] T. Dirlik, "Application of computers in fatigue analysis," Warwick University, 1985.

[36] W. H. Hu and S. Thoens, "Vibration-based structural health monitoring of a wind turbine system," *Engineering structures,* pp. 273-290, 2015.

[37] L. Wenyi and T. Baoping, "Status and problems of wind turbine structural health monitoring techniques in China," *Renewable Energy,* vol. 35, no. 7, pp. 1414-1418, 2010.

[38] Chiang and Chen, "Structural health monitoring for a wind turbine system," *Measurement Science and Technology,* vol. 19, no. 12, 2008.

[39] W. Husson, "Friction connections with slotted holes for wind towers," PhD Thesis, Sweden, 2008.

[40] D. Molenaar and J. v. d. Tempel, "Wind turbine structural dynamics-A review of the principles for modern power generation, onshore and offshore.," *Wind Engineering,* vol. 26, no. 4, 2002.

[41] T. Burton, N. Jenkins and D. Sharpe, Wind Energy Handbook (second edition), Wiley, 2012.

[42] E. Lourens, "Material from course OE5665 "Offshore Wind Support Structures"," Technical University of Delft, Delft, 2014.

[43] C. Heistermann, W. Husson and M. Veljikovic, "Flange connections vs. friction connections in tower for wind turbines," *Lulea University of Technology, Sweden,* 2009.

[44] Northstarwind, "www.northstarwind.com," 2015. [Online].

[45] C. Petersen, Stahlbau: Grundlager der Berechnung und baulichen Ausbildung von Stahlbauten, Springer, 2008.

[46] DIBt, Deutsches Institut fuer Bautechnik: Richtlinie fuer Windenergieanlagen., 2012.

[47] DNV, " Det Norske Veritas: OS-J101 Offshore Standard; Design of offshore wind turbine structures," 2011.

[48] A. Schaffarczyk, Understanding wind power technology: theory, deployment and optimization, Wiley, 2014.

[49] GL, Germanischer Lloyd: Tragverhalten imperfekter Ringflanschverbindungen von Windenergieanlagen, 2004.

[50] VDI, Verein Deutscher Ingenieure 2230: Systematische Berechnung hochbeanspruchter Schraubenverbindungen Zyllindrische einschraubenverbindungen, 2003.

[51] P.Schaumann and M.Seidel, "Experimentelle und numerische Untersuchungen von Ringflanschverbindungen," vol. Commemorative volume for Prof. Valtinat, 2001.

[52] J. Soerensen, Wind energy systems: optimizing design and construction for safe and reliable operation, Woodhead publishing, 2011.

[53] E. Standard, EN 1993-1-9. Eurocode 3: Design of steel structures-Part 1-8: Fatigue., 2004.

[54] GL, Germanischer Lloyd: Richtlinie für die Zertifizierung von Windenergieanlagen., 2010.

[55] J. Jonkman, S. Butterfield, W. Musial and G. Scott, Definiton of a 5MW Reference Wind Turbine for Offshore System Development, USA: NREL, 2009.

[56] K. Branner, "Anisotropic beam model for analysis and design of passive controlled wind turbine blades," *DTU Wind Energy report E-0001 (EN),* p. 41, February 2012.

[57] J. Larsen and A. Hansen, How 2 HAWC2, Risoe, Denmark: DTU, 2012.

[58] IEC, "International European Code 61400-3: Wind turbines part 3: Design requirements for offshore wind turbines," 2007.

[59] T. Irvine, "The damping characteristics of bolted and welded joints," AOL, 2010.

[60] W. Chen and X. Deng, "Structural damping caused by micro-slip along frictional interfaces," *International Journal of Mechanical Sciences,* vol. 47, 2004.

[61] D. Pilkey, "Computation of a Damping Matrix for Finite Element Model Updating," Virginia Polytechnic Institute and State University, 1998.

[62] B. Nanda, "Study on damping in layered and jointed structures with uniform pressure distribution at the interfaces," *Journal of sound and vibration,* vol. 226(4), pp. 607-624, 1999.

[63] S. Bograd, A. Schmidt and L. Gaul, "Joint damping prediction by thin layer elements," Instituet fuer Angewandte und Experimentelle Mechanik, Stuttgart, 2008.

[64] Xu and Weiwei, "Effect of bolted joint preload on structural damping," Scholar Commons Citation: Graduate Theses and Dissertations, 2013.

[65] J. Renninger, "Understanding damping techniques for noise and vibration control," EAR specialty composites, Indianapolis US.

[66] "www.matlab.com," MathWorks, 2015. [Online].

[67] DNV, Det Norske Veritas: RP-C203 Fatigue Design of Offshore Steel Structures, 2011.

[68] GL, "Guideline for the certification of offshore wind turbines," 2012.

[69] F. Yousefi, "Fatigue strength of welded joints under multiaxial loading: experiments and calculations.," *Fatigue Fract Engng Mater Struct ,* vol. 24, pp. 339-355, 2001.

[70] C. Sonsino, "Multiaxial fatigue of welded joints under in-phase and out-of-phase local strains and stresses," *International Journal of Fatigue,* vol. 17, no. 0, pp. 55-70, 1995.

[71] Susmel, Tovo and Benasciutti, "A nover engineering method based on the critical plane concept to estimate the lifetime of weldments subjected to variable amplitude multiaxial fatigue loading.," *Fatigue and Fracture of Engineering Materials and Structures,* 2009.

[72] R. C. Hibbeler, Mechanics of Materials, Pearson, 2012.

[73] EC, "Eurocode 3: Design of steel structures- Part 1-9: Fatigue," European Standard, 2005.

[74] D. White and W. Musial, "The Effect of Load Phase Angle on Wind Turbine Blade Fatigue Damage (NREL)," in *AIAA Aerospace Sciences Meeting and Exhibit*, Reno, Nevada, USA, 2004.

[75] A. Carpinteri, "Expected principal stress directions under multiaxial random loading through weight function method," in *5th international conference on biaxial/multiaxial fatigue and fracture*, Cracow, Poland, 1997.

[76] W. Bedkowski, B. Kenmeugne and E. Macha, "On the prediction of the fracture plane orientation," in *International Conference on Biaxial/Multiaxial Fatigue and Fracture*, Cracow Poland, 1997.

[77] S. Babaei, G. Ghalebahman and Ahmad, "Damage-based modification for fatigue life prediction under non-proportional loading," *International journal of fatigue,* 2015.

[78] V. Anes and L. Reis, "Multiaxial fatigue damage accumulation under variable amplitude loading conditions," in *3rd International Converence on Material and Component Performance under Variable Amplitude Loading, VAL2015*, Lisabon, Portugal, 2015.

[79] N. Shamsael and A. Fatermi, "Effect of harness on multiaxial fatigue behaviour and some simple approscimations for steels," *Fatigue and fracture of engineering material structures,* 2009.

[80] Reliasoft, Accelerated life testing reference, Tucson, AZ: ReliaSoft Publishing, 2007.

[81] FEMFAT, "www.femfat.com," FEMFAT, 2015. [Online].

[82] C. Sonsino and J. Wiebesiek, "Assessment of multiaxial spectrum loading of welded steel and aluminium joints by modified equivalent stress and Gough-Pollard algorithms," Fraunhofer-Institute for structural durability and system reliability, Darmstadt, Germany, 2010.

[83] C. Sonsino, "Mail contact with Sonsino between 02-04-2015 and 28-06-2015.," 2015.

[84] "www.google.nl/maps," Google, 2015. [Online].

[85] IEC, International European Code 61400-1: Wind turbines part 1: Design requirements, 2006.

[86] DTU, "DTU Wind Energy: NREL 5MW Reference Values," DTU, 2009.

Appendix A

A. Resiliences

In this appendix, the following resiliencies will be discussed:

Plate resilience

a) Concentrically clamped and loaded
b) Eccentrically clamped
    i) Concentrically loaded
    ii) Eccentrically loaded

Bolt resilience

a) Concentrically clamped and loaded
b) Eccentrically clamped
    i) Concentrically loaded
    ii) Eccentrically loaded

Concentric clamped and loaded plate resilience

If the diameter of the basic solid at the interface is larger than the maximum diameter of the deformation cone, the clamp solid only consist of cones and Equation A.1 should be used to calculate the resilience of the concentrically clamped parts.

$$If\ D_A \geq D_{A,Gr}$$

$$\delta_P^Z = \frac{2 \cdot \ln\left(\frac{(d_w + d_h) \cdot (d_w + w \cdot l_k \cdot tan(\varphi - d_h))}{(d_w - d_h) \cdot (d_w + w \cdot l_k \cdot tan(\varphi + d_h))}\right)}{w \cdot E_p \cdot \pi \cdot d_h \cdot \tan(\varphi)} \qquad \text{Equation A.1}$$

As a result of a large clamp length, the deformation cones can reach the outer edge of the cylindrical components and therefore allowance has to be made for a deformation sleeve lying in between, see figure A.1.

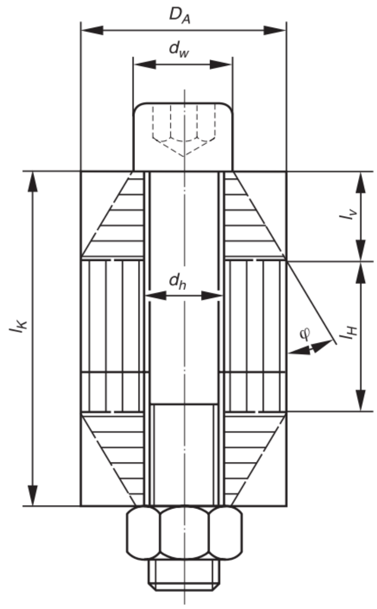

Figure A.1: Deformation sleeves lying in between the cones [50].

In this situation Equation A.2 should be used to calculate the resilience of the concentrically clamped parts.

$$If\ d_w < D_A < D_{A,Gr}$$

$$\delta_P^Z = \frac{\frac{2}{w \cdot d_h \cdot \tan(\varphi)} \cdot \ln\left(\frac{(d_w + d_h) \cdot (D_A - d_h)}{(d_w - d_h) \cdot (D_A + d_h)}\right) + \frac{4}{D_A^2 - d_h^2}\ (l_K - \frac{(D_A - d_w)}{w \cdot \tan(\varphi)}}{E_p \cdot \pi} \qquad \text{Equation A.2}$$

Eccentrically clamped plate resilience

With use of the resiliences for *concentrically clamped* joints and with taking the bending resilience into account, the resilience of *eccentrically clamped* joints can be calculated with Equation A.3 and Equation A.4, respectively.

For *concentrically loaded* flanges:

$$\delta_p^* = \delta_p + s_{sym}^2 \cdot \beta_P \qquad \text{Equation A.3}$$

For *eccentrically loaded* flanges:

$$\delta_p^{**} = \delta_p + a \cdot s_{sym} \cdot \beta_P \qquad \text{Equation A.4}$$

As you can see is a bending resilience included in these formulas. This resilience can be calculated with Equation A.5.

$$\beta_{S,P} = \frac{l_K}{E_{S,P} \cdot I_{Bers}}$$ Equation A.5

With

$$I_{Bers} = \frac{l_k}{\frac{2}{w}\left(\frac{l_v}{I_{Bers}^{Ve}} + \frac{l_h}{I_{Bers}^{H}}\right)}$$ Equation A.6

$$I_{Bers}^{Ve} = 0.147 \cdot \frac{(D_A - d_w) \cdot d_W^3 \cdot D_A^3}{D_A^3 - d_w^3} + S_{Sym}^2 \cdot \frac{\pi}{4} D_A^2$$ Equation A.7

$$I_{Bers}^{H} = b \cdot \frac{c_T^3}{12}$$ Equation A.8

Abb.	Description
$\boldsymbol{\beta}$	Bending resilience
$\boldsymbol{I_{Bers}}$	Substitutional moment of gyration of the deformation solid
$\boldsymbol{I_{Bers}^{Ve}}$	Substitutional moment of gyration of the deformation cone
$\boldsymbol{I_{Bers}^{H}}$	Substitutional moment of gyration of the deformation sleeve
$\boldsymbol{c_T}$	Measurement of the interface area perpendicular to the width b

Table A.1: Parameters in bending resilience calculations.

Concentric bolt resilience

The total elastic resilience (stiffness) of the bolt is determined by adding the resiliences of the individual cylindrical elements within the clamp length and the further deformations regions.

$$\delta_s = \delta_{SK} + \delta_w + \delta_{be} + \delta_{shaft} + \delta_{ibt} + \delta_{abt} + \delta_n$$ Equation A.9

Eccentrically clamped bolt resilience

A bending resilience β_s of the bolt, which is required when bending moments are acting in order to calculate the additional stress resulting from the bending load, can be defined in a manner similar to the axial resilience.

$$\beta = \frac{l}{E \cdot I}$$ Equation A.10

For concentrically loaded bolts:

$$\delta_s^* = \delta_s + s_{sym}^2 \cdot \beta_s$$ Equation A.11

For *eccentrically loaded* flanges:

$$\delta_s^{**} = \delta_s + a \cdot s_{sym} \cdot \beta_s$$ Equation A.12

The eccentric bolt resilience is disregarded in most cases because hence the bolt calculations will be more conservative. Ignoring the bending resilience, decreases the total resilience of the bolt, making the bolt share of the load higher and the flange share of the load lower, see Section 2.3.5.

Appendix B

B. Flange failure modes

$M'_{Pl,2} = \frac{c' \cdot t^2}{4} \cdot f_{yd}$	is the reduced bending resistance of the flange at the bolt axis,
$M_{Pl,2} = \frac{c \cdot t^2}{4} \cdot f_{yd}$	is the full bending resistance of the flange,
$\Delta M_{Pl,2} = \frac{F_{t,Rd}}{2} \cdot \frac{d_S + d_B}{4}$	is the additional resistive moment introduced by the eccentricity of the bolt force,
$M_{Pl,3}$	is the bending resistance of the shell or of the flange, considering the M-N and M-V interaction respectively. It is iteratively derived from:

$$M_{Pl,3} = \min \begin{cases} M_{Pl,N,Shell} = \left[1 - \left(\frac{N}{N_{Pl,Shell}}\right)^2\right] \cdot M_{Pl,Shell} = \left[1 - \left(\frac{F_U}{c \cdot s \cdot f_{yd,Shell}}\right)^2\right] \cdot \frac{c \cdot s^2}{4} \cdot f_{yd,Shell} \\ M_{Pl,V,Flange} = \left[\sqrt{1 - \left(\frac{V}{V_{Pl,Flange}}\right)^2}\right] \cdot M_{Pl,Flange} = \left[\sqrt{1 - \left(\frac{F_U}{c \cdot t \cdot f_{yd,Flange}}\right)^2}\right] \cdot \frac{c \cdot t^2}{4} \cdot f_{yd,Flan} \end{cases}$$

R	is the reaction force at the flange edge,
a	is the distance from the bolt axis to the flange edge,
b	is the distance from the bolt axis to the shell mid plane,
t	is the flange thickness,
s	is the shell thickness,
c	is the segment width,
$c' = c - d_B$	is the segment width reduced by the bolt hole diameter,
d_H	is the bolt hole diameter,
d_W	is the washer diameter,
b'_D	is the distance between bolt axis and plastic hinge in the shell or flange,
b'_E	is the distance between mid-washer and plastic hinge in the shell or flange,

Failure mode	Resistance	Conditions of validity
A	$F_U = F_{t,Rd}$	The bending resistance of the shell is not exceeded: $F_U \cdot b \le M_{Pl,3}$
B	$F_U = \dfrac{F_{t,Rd} \cdot a + M_{Pl,3}}{a + b'}$	The minimum bending resistance of the flange, at the bolt axis, is not exceeded: $R.a \le M'_{Pl,2}$
D	$F_U = \dfrac{M'_{Pl,2} + \Delta M_{Pl,2} + M_{Pl,3}}{b'_D}$	The full bending moment of the flange is not exceeded at mid-washer: $\left(\dfrac{F_{t,Rd}}{2} - F_{U,D}\right)\left(\dfrac{d_W + d_H}{4}\right) \le M_{Pl,2} - M'_{Pl,2}$ The reaction force, R, must act on the flange: $r = \dfrac{M'_{Pl,2} + \Delta M_{Pl,2}}{F_{t,Rd} - F_U} \le a$
E	$F_U = \dfrac{M_{Pl,2} + M_{Pl,3}}{b'_E}$	The minimum bending moment of the flange is not exceeded at the bolt axis: $\left(\dfrac{F_{t,Rd}}{2} - F_{U,E}\right)\left(\dfrac{d_W + d_H}{4}\right) \ge M_{Pl,2} - M'_{Pl,2}$ The reaction force, R, must act on the flange: $M'_{Pl,2} + 2 \cdot \Delta M_{Pl,2} = R \cdot \left(r + \dfrac{d_W + d_H}{4}\right)$ $r = \dfrac{M'_{Pl,2} + 2 \cdot \Delta M_{Pl,2}}{F_{t,Rd} - F_U} - \dfrac{d_W + d_H}{4} \le a$

Table B.1: Failure mode checks [39].

Appendix C

C. Bolt load calculations

Petersen [45] suggests the following procedure to calculate the axial working force F_A from the force in the shell F_{sh}.

$$F_A = \alpha \cdot \frac{EI}{b^2}$$ Equation C.1

The parameters β, γ, δ and ε (Equation C.2-Equation C.6) are used to define the parameter α from Equation C.1.

$$\alpha = \frac{\left(\frac{1}{2} + \frac{1}{\varepsilon} + \left(1 + \frac{1}{\varepsilon} + \frac{\gamma}{3}\right) \cdot \gamma\right) \cdot \Gamma}{1 + \left(1 + \frac{1}{\varepsilon} + \frac{\gamma}{3}\right) \cdot \gamma \cdot \Gamma} \cdot \beta$$ Equation C.2

$$\beta = \frac{F_{sh} \cdot b^2}{E\,I_f}$$ Equation C.3

$$\gamma = \frac{a}{b}$$ Equation C.4

$$\Gamma = \frac{2 \cdot C \cdot a \cdot b^2}{EI_f}$$ Equation C.5

$$\varepsilon = \frac{K \cdot b}{EI_f}$$ Equation C.6

As can be seen in above equations, the axial working force F_A is proportional with the shell force F_{sh}.

Table 3.2 gives an overview of the parameters used in the above equations.

Abb.	Description	Explanation
$\boldsymbol{a}$	Distance between bolt hole and flange inner diameter	Figure 2.29
$\boldsymbol{b}$	Distance between bolt hole and flange outer diameter	Figure 2.29
$\boldsymbol{C}$	Combined stiffness of flange and bolt	$\frac{1}{\delta_{tot}}$
$\boldsymbol{\delta_{tot}}$	Total stiffness resilience of bolt and flange	$\delta_{tot} = \delta_{bolt} + \delta_{flange}$
$\boldsymbol{EI_f}$	Flange bending stiffness = Young's modulus of steel · moment of inertia of flange	$E \cdot \frac{1}{12} \cdot w_l \cdot {t_f}^3$
$\boldsymbol{w_l}$	Load application width = arc distance between 2 bolts	d_{cb}/N_{bolts} (Figure 2.20)
$\boldsymbol{t_f}$	Flange thickness	Figure 2.20
$\boldsymbol{K}$	Cylinder wall stiffness	$E \cdot 4 \cdot \frac{1}{12 \cdot d_h} \cdot w_l \cdot {t_f}^3$
$\boldsymbol{z_t}$	Vertical distance from nacelle to investigated flange	

Table C.1: Parameters used in the bolt stress calculations according Petersen.

The VDI guideline makes use of the Petersen model and extends this by taking the bending moments in the bolts also into account. This means that in addition to the elastic axial resiliences δ_s and δ_p of the bolts and plates, the bending resiliences β_s and β_p of these parts also have to be taken into account.

$$\delta_p^{**} = \delta_p + a \cdot s_{sym} \cdot \beta_P \qquad \text{Equation C.7}$$

$$\delta_S^{**} = \delta_s + a \cdot s_{sym} \cdot \beta_s \qquad \text{Equation C.8}$$

Appendix D

D. Wind turbine data

In the report two different wind turbines are used as a reference. The 5MW-NRELT (5MW reference turbine designed by the National Renewable Energy Laboratory) is used for analyzing the influence of flange design on the global dynamical behavior of wind turbines (Chapter 3) and for the EESH calculations (Chapter 6). The 6MW-SWT (6MW Siemens Wind Turbine) also used for the EESH calculations. Furthermore the flange standardization research is based on this wind turbine (Chapter 4).

5MW-NRELT specifications

Rotor		**Generator-Drive train**	
Diameter	126 m	Rated output	5 MW
Area swept	12469 m^2	Drivetrain	High speed
Cut-in, Rated Rotor Speed	6.9-12.1 rpm	Gearbox	Multiple-Stage
Number of blades	3		
Power regulation	Variable speed, Pitch		
Rated tip speed	80 m/s		
Tower		**Operational data**	
Hub height	90 m	Cut-in wind speed	3 m/s
Base-top diameter	6.00-3.87 m	Rated wind speed	11.4 m/s
Base-top wall thickness	35-25 mm	Cut-out wind speed	25 m/s
Shape	Conical		
Mass			
Nacelle-Rotor	350 t		

Table D.1: 5MW-NRELT specifications.

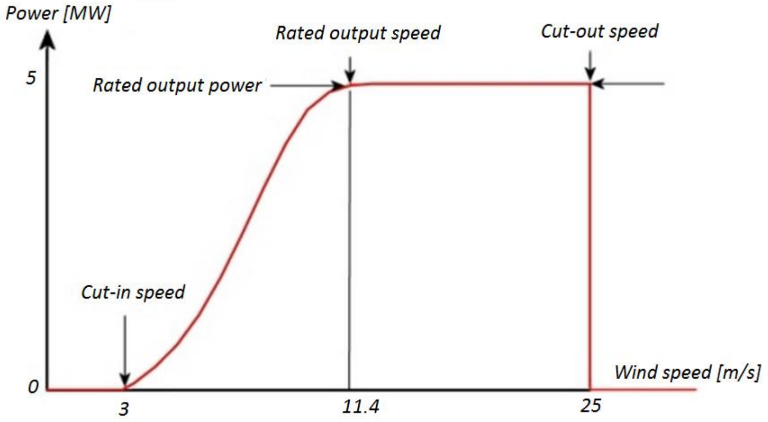

Figure D.1: Power curve 5MW-NRELT [74].

6MW-SWT specifications

Rotor		**Generator-Drive train**	
Diameter	154 m	Rated output	6 MW
Area swept	18600 m^2	Drivetrain	High speed
Cut-in, Rated Rotor Speed	5-11 rpm	Gearbox	No
Number of blades	3		
Power regulation	Variable speed, Pitch		
Rated tip speed	80 m/s		
Tower		**Operational data**	
Hub height	105 m	Cut-in wind speed	3 m/s
Base-top diameter	6.00-4.15 m	Rated wind speed	13m/s
Base-top wall thickness	45-19mm	Cut-out wind speed	28 m/s
Shape	Cylindrical-conical		
Mass			
Nacelle-Rotor	350 t		

Table D.2: 6MW-SWT wind turbine specifications.

The 6MW-SWT power curve has the same shape as the NRELT curve, see Figure D.1. The wind speeds are however different, see Table D.2.

Appendix E

E. Environmental data

A data package [1] is used from the location located at 53° 17’ N and 04° 01’ E as marked in Figure E.1. The environmental conditions at the wind turbine location should be deduced from the given data pack. It will be used to run realistic HAWC2 simulations. Furthermore, these conditions influence the height of the support structure, which has to be designed specifically for the considered location.

Figure E.1: Site location from where the data is retrieved [84].

Water depth

The given water depth is 25m.

Water levels

Figure E.2 - Figure E.5 show the sorted measure points of the given data about the sea level elevation due to tide and surge. The data is from the period 1979-2001. The cumulative density functions are constructed for both the yearly minima and maxima. The values that correspond to a cumulative probability of 98% (50 years maximum) will be used as reference values for our design.

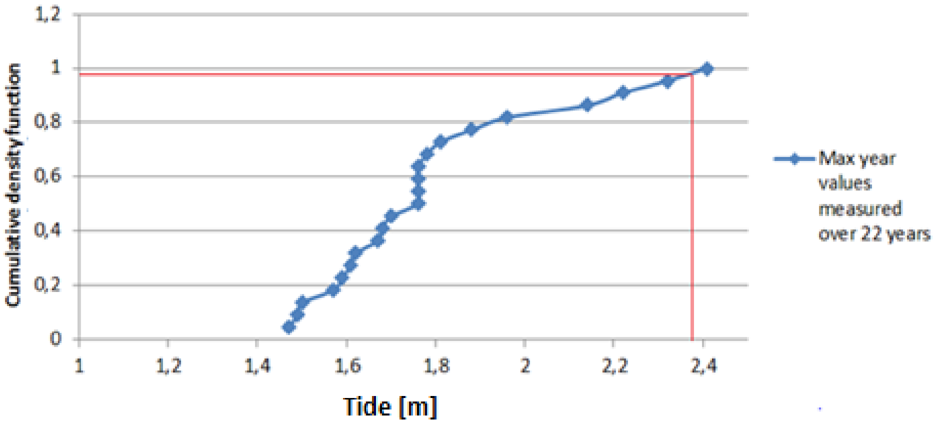

Figure E.2: Cumulative density function tide maxima (50 years value = 2.37 m).

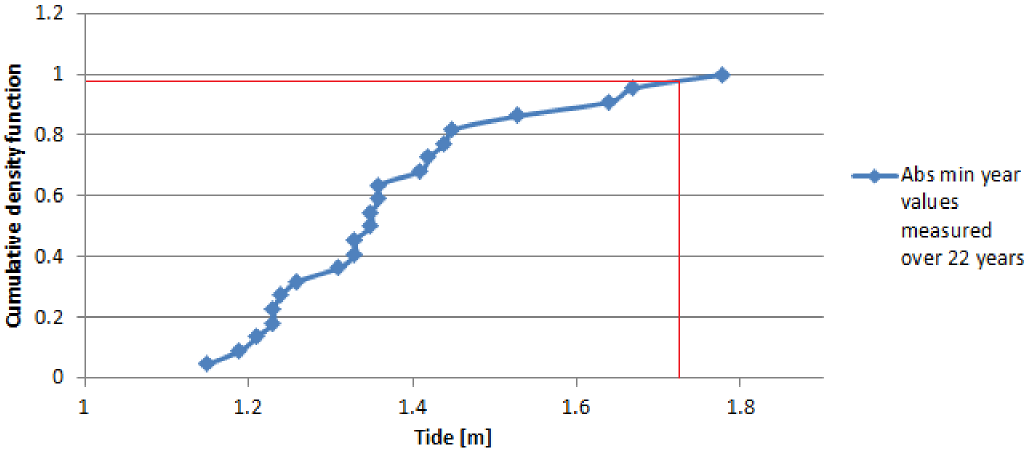

Figure E.3: Cumulative density function tide minima (50 years value = -1.73 m).

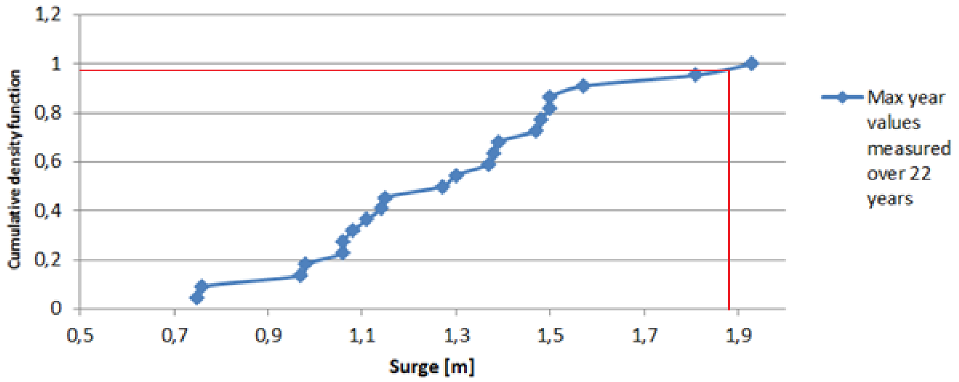

Figure E.4: Cumulative density function surge maxima (50 years value = 1.88 m).

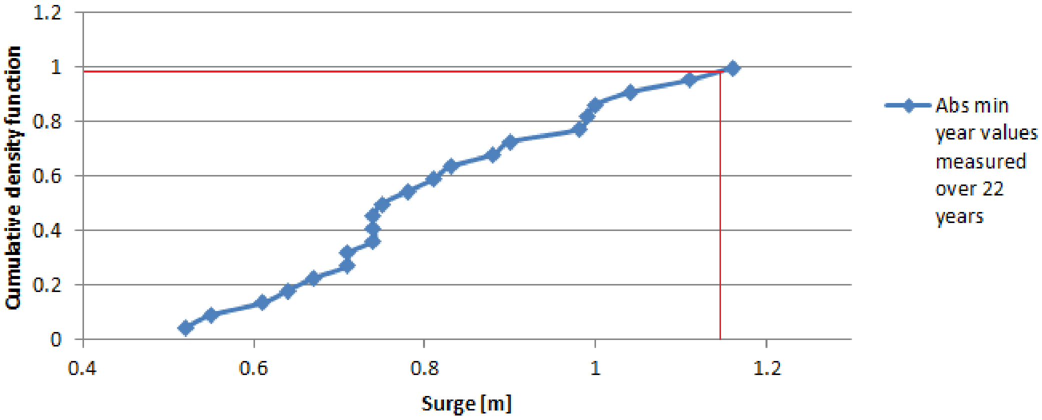

Figure E.5: Cumulative density function surge minima (50 years value = -1.14 m).

The 50 years maximum tide and maximum surge are 2.37 m and 1.88 m, respectively. The 50 years minimum tide and surge are -1.73 m and -1.14 m, respectively.

Highest surge water level	+4.25 m MSL
Highest astronomical tide	+2.37 m MSL
Mean sea level	25 m
Lowest astronomical tide	-1.73 m MSL
Lowest surge water level	-2.87 m MSL

Table E.1 Water level elevations.

Current

The current data from the data pack gives the direction and speed of the current every hour in a period of 13.3 years. With these data a cumulative density function is constructed.

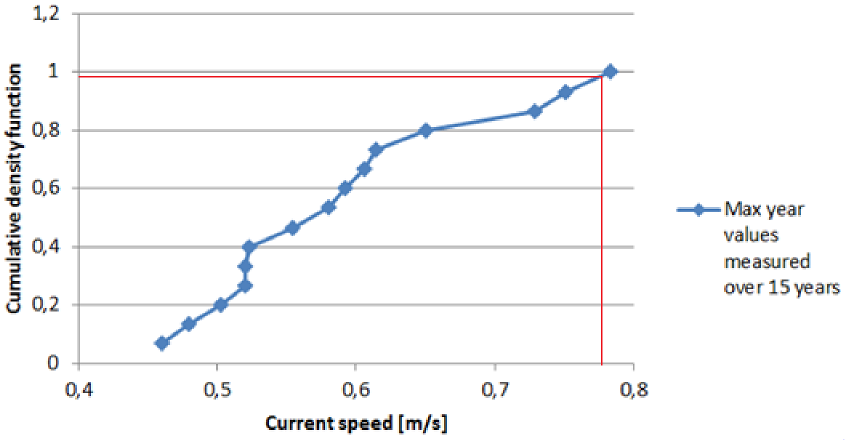

Figure E.6: cumulative probability function current speeds (50 years value = 0.76 m).

Table E.2 summarizes the current data. In addition, the directional data shows that there is no prevailing current direction. For the design load cases an average current is assumed.

Average current speed	0.19 m/s
50 years maximum current speed	0.76 m/s
Average direction current	184 degrees
Standard deviation current	104 degrees

Table E.2: Current data.

Wave parameters

Extreme values

The extreme wave heights are determined by fitting a Weibull distribution to the measured data as shown below.

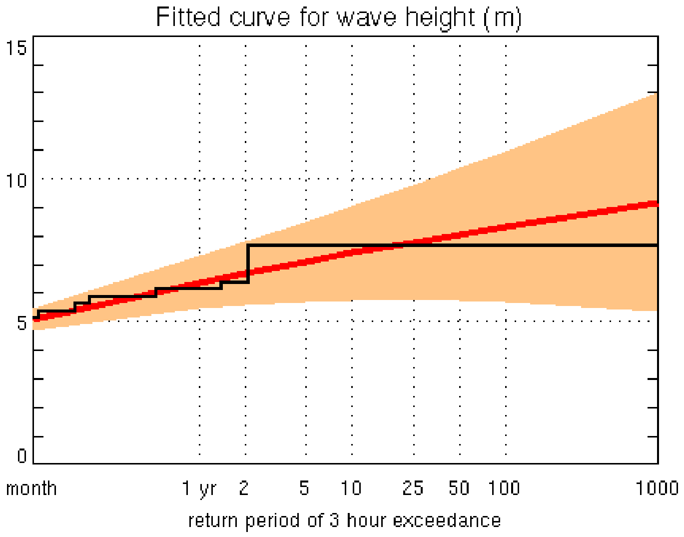

Figure E.7: Wave height return period.

Furthermore, the maximum wave height is calculated as a function of the significant wave height [58] [85], see Equation E.1.

$$H_{max} = 1.86 \cdot H_{sig} \qquad \text{Equation E.1}$$

Table E.3 summarizes the relevant design values.

Return period $[years]$	$H_{sig}\,[m]$	$H_{max}\,[m]$
5	8.5	15.81
50	10.4	19.34

Table E.3: Extreme wave heights.

Wave directions

The wave rose in Figure E.8 shows the spreading of the wave directions per wave height bin of 0.5 m. The different colors in Figure E.8 indicate different wave heights. The dominant wave direction is north north west (≈330˚) and south west (≈210˚-240˚) which also depends on the wave height.

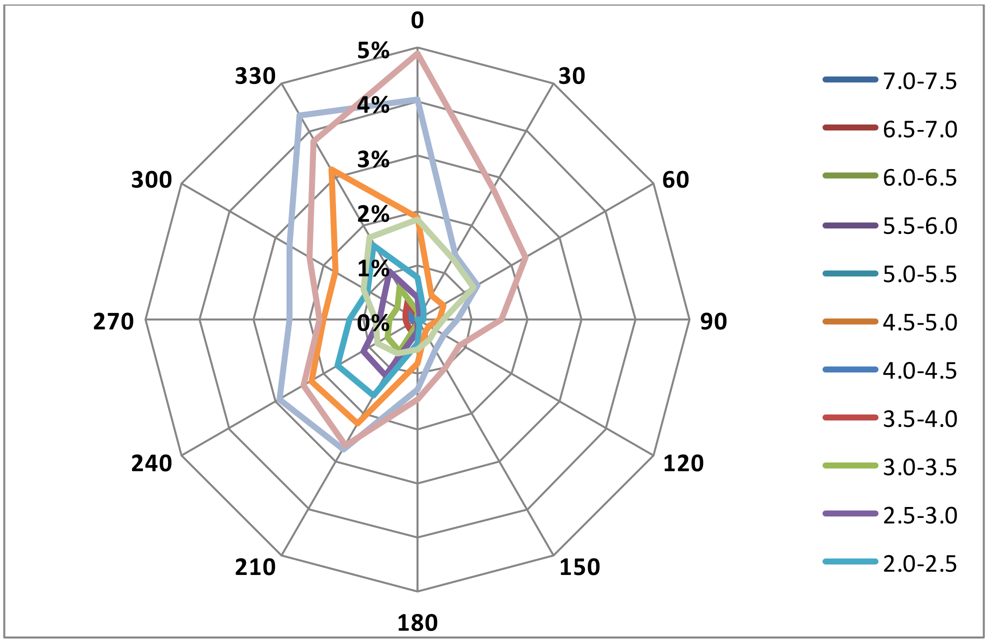

Figure E.8: Wave direction rose for different wave heights. Wave height given in [m].

Wind parameters

Mean wind

A wind turbine shall be designed to safely withstand the wind conditions occurring at a certain location. An exponential vertical shear is assumed. The vertical wind shear exponent (power law exponent), α, shall be assumed to be 0.14, as defined in IEC 61400-3 for standard wind turbine classes.

First the wind speeds measured at a height of 10 meter has to be transferred to the wind speeds at hub height. According to IEC 61400-3, this can be done with use of the power law of the normal wind profile model, see Equation E.2.

$$V_{hub}=\frac{V(z)}{\frac{z}{z_{hub}}^{\alpha}} \qquad \text{Equation E.2}$$

For the wind load calculations a 10 minute average wind speed is needed. Since the data is given as a 1-hour average wind speed, a conversion factor of 0.95 is used [58]. According to the wind speed distribution in Figure E.9, the annual mean wind speed is 7.6m/s at 10m above MSL which leads to an average wind speed of 10.05 m/s at a hub height of 106m above MSL.

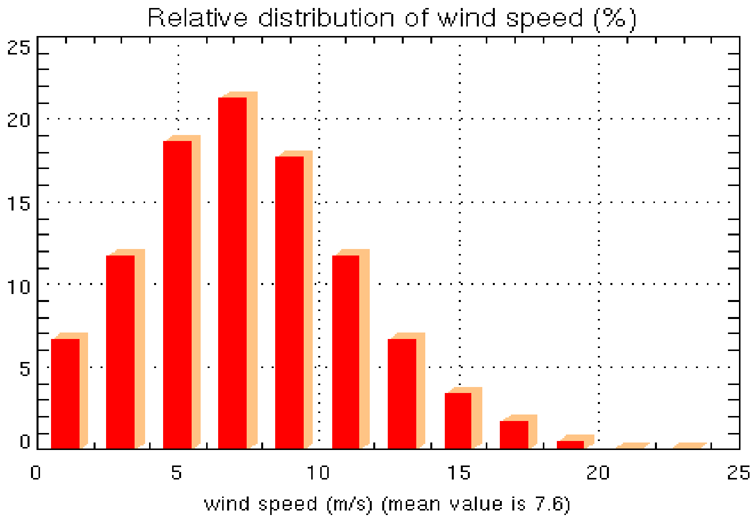

Figure E.9: Wind speed distribution.

Turbulence

Turbulence denotes random variations in the wind velocity from 10 min. averages. To define turbulence, the turbulence intensity should be calculated. The turbulence intensity is defined as the variance divided by the wind speed at hub height.

The 5MW-NRELT has wind turbine class 1B [58] and therefore for the reference turbulence intensity, which is used to calculate the turbulence intensity, the value 0.14 has to be chosen [58].

Extreme values

The extreme wind heights are determined by fitting a Weibull distribution to the measured data as is shown below.

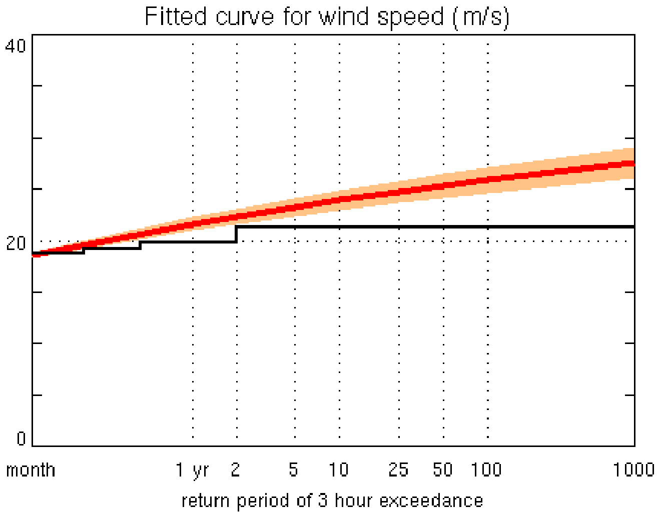

Figure E.10: Wind speed return periods.

Furthermore, the obtained 3-hour values are converted to 10-minute average by use of the conversion factor of 0.95. The wind speeds are calculated at a hub height of 106m according to formula 4.2. Table 4.5 summarizes the resulting extreme wind speeds.

Return period [years]	**Vw [m/s] 10m/3hour**	**Vw [m/s] 10m/10min**	**Vw [m/s] 106m/3hour**	**Vw [m/s] 106m/10min**
5	23.3	21.20	30.81	29.27
50	25.3	22.77	33.45	31.78

E.4: Extreme wind speeds.

Wind directions

The wind rose in Figure E.11 shows the spreading of the wind directions per wind speed bin of 2m/s. The dominant wave direction is west south west (≈240˚) which also depends on the wind speed. The main wind direction agrees with one of the main wave directions (≈210˚-240˚).

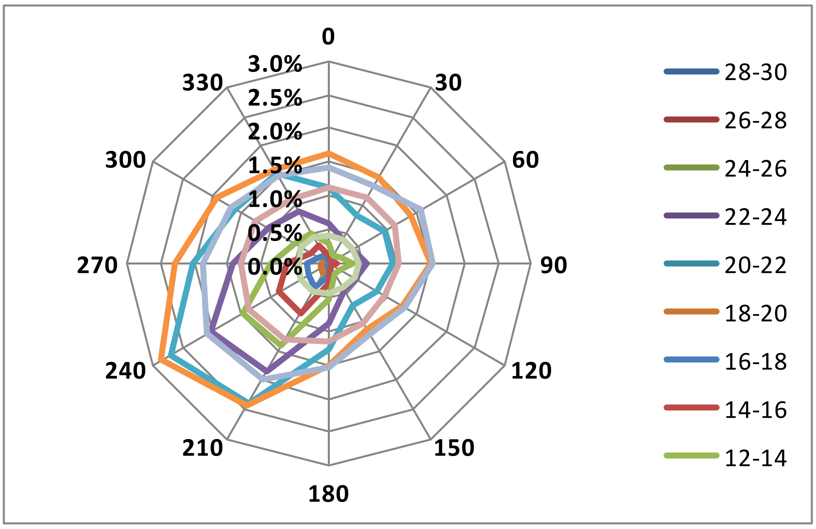

Figure E.11: Wind rose.

Lumped sea states

The sea states from the given 3D scatter diagram in the data package are grouped into 18 typical sea states according to Table E.5. The environmental parameters of a lumped sea state are selected in such a manner that they will result in approximately the same damage that accumulates considering all elementary sea states with spread environmental parameters [6].

Sea State	Vw 10 m [m/s]	Vw HH [m/s]	Hs [m]	Tz [s]	Tp [s]	TI NTM [%]	TI ETM [%]	Occur. [%]
1	16.72	21.07	4.93	7.30	9.34	13.5	16.3	0.98
2	14.77	18.53	3.75	6.22	7.96	14.5	19.1	1.45
3	13.43	17.76	3.25	5.74	7.35	14.9	20.2	3.19
4	12.42	16.42	2.75	5.61	7.18	15.3	21.2	5.51
5	12.19	16.12	2.25	5.25	6.72	15.4	21.4	5.77
6	7.69	10.17	2.25	5.39	6.90	18.2	29.3	3.13
7	11.64	15.39	1.75	4.58	5.86	15.6	22.1	5.57
8	8.20	10.84	1.75	4.87	6.23	17.7	27.9	8.18
9	8.37	11.07	1.75	5.50	7.04	17.6	27.5	1.97
10	9.56	12.64	1.25	4.40	5.63	16.7	25.1	9.33
11	6.25	8.26	1.25	4.49	5.75	20.0	34.1	10.13
12	4.24	5.61	1.25	5.56	7.12	24.5	46.5	5.40
13	7.45	9.85	0.75	3.84	4.92	18.5	29.9	10.65
14	3.86	5.10	0.75	4.69	6.00	25.9	50.3	17.33
15	2.37	3.13	0.25	4.38	5.61	35.5	76.8	6.70
16	2.42	3.20	0.25	6.17	7.90	35.0	75.4	0.91
17	5.28	6.98	0.25	3.98	5.09	21.7	38.9	3.66
18	18.06	24.88	5.85	7.46	9.55	13.2	15.5	0.14
							Tot occ:	100.00

Table E.5: Lumped sea states.

Soil

The soil is modeled with use of the coupled springs model, see Figure E.12. A linear translational spring and a rotational spring, which are coupled, represent the soil characteristics. The standard values from the HAWC2 NREL 5MW reference wind turbine model are taken.

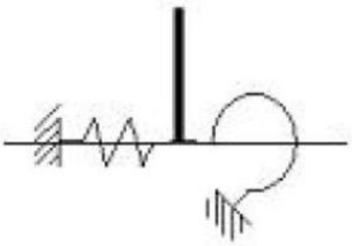

Figure E.12: Coupled spring model [57].

Appendix F

F. HAWC2 simulations

This appendix displays the graphs of the total moments for the simulations that yield the largest moments of the first ULS load case (1.3d) and the second ULS load case (1.4b). The moments are given for the four flange locations.

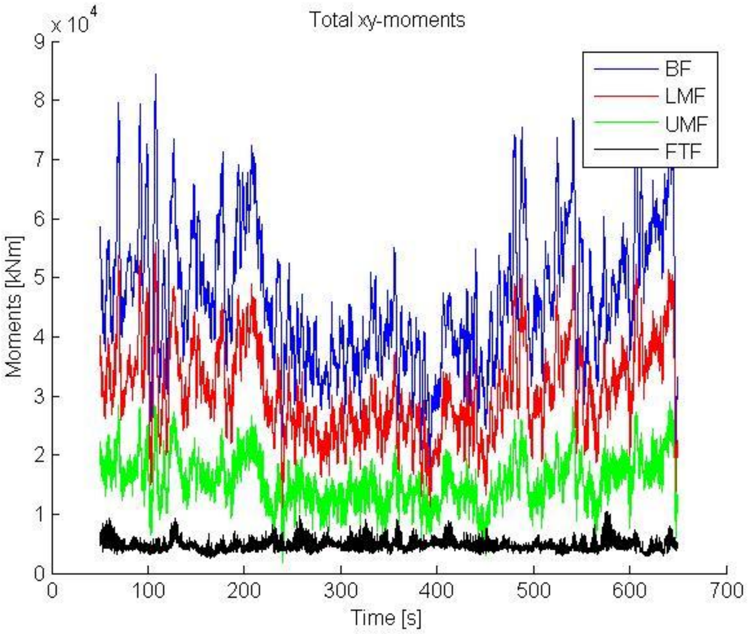

Figure F.1: Total moment DLC 1.3d $\left(\sqrt{M_x^2 + M_y^2}\right)$.

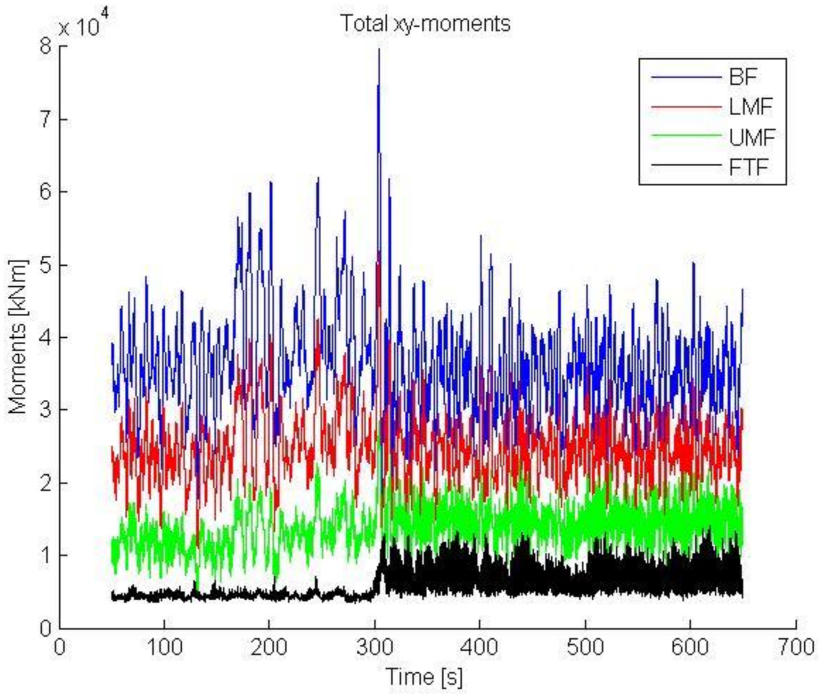

Figure F.2: Total moment DLC 1.4b ($\sqrt{M_x^2 + M_y^2}$).

The fore-aft moment, side-to-side moment, and yaw moment for simulations 1.3d will also be shown to exemplify the ratios between the moments.

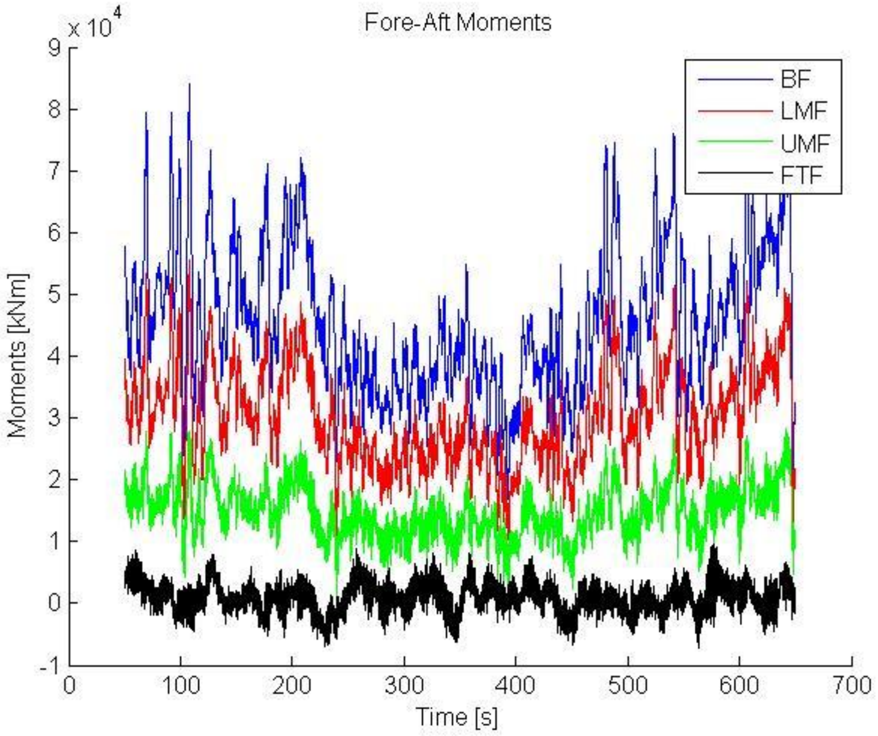

Figure F.3: Fore-Aft moments DLC 1.3d.

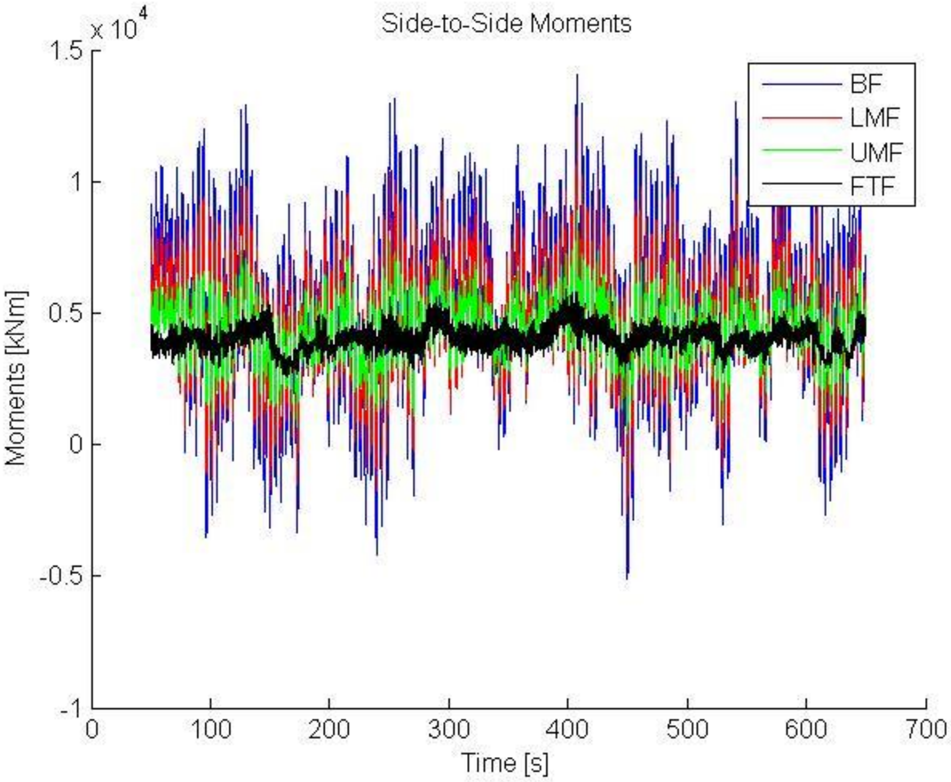

Figure F.4: Side-to-side moments DLC 1.3d.

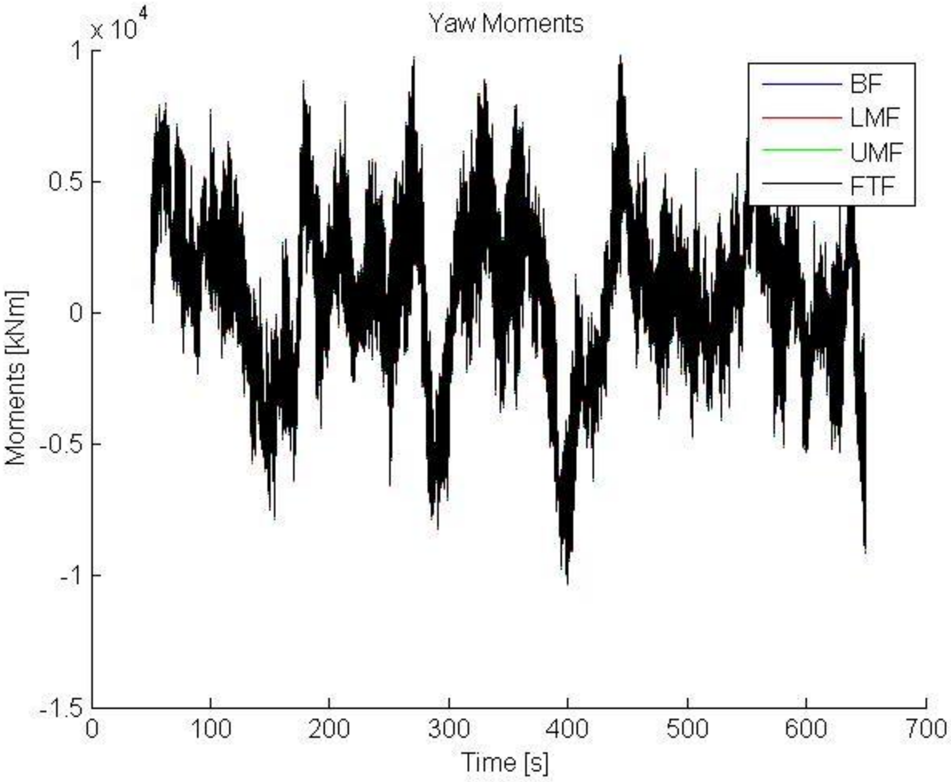

Figure F.5: Yaw-moment DLC 1.3d.

Appendix G

G. Support structure design

Interface level

Figure G.1 shows the different interface levels.

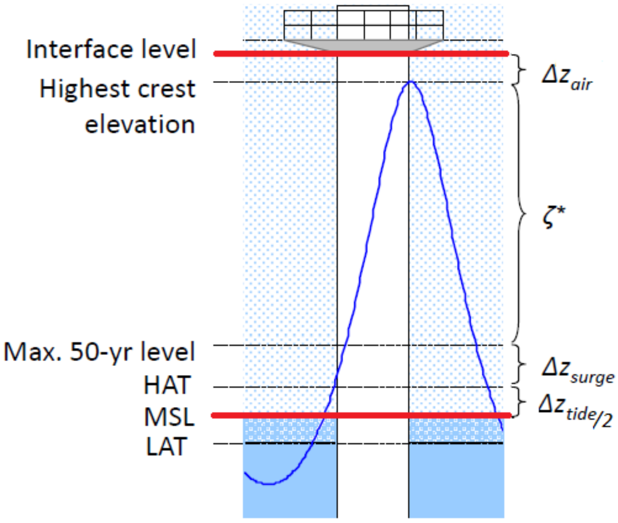

Figure G.1: Elevation levels [42].

The interface level is based on environmental data, as Equation G.1 shows.

$$z_{interface} = \frac{z_{tide}}{2} + \mathrm{z_{surge}} + \mathrm{z_{air}} + \eta_* \qquad \text{Equation G.1}$$

with $\eta_* = 0.65 * H_{max}$ and $H_{max} = 1.86 * H_{s,50}$

Abb.	Description
z_{tide}	tidal range [m]
H_{max}	maximum wave height [m]
D_{rotor}	Rotor diameter [m]
z_{surge}	storm surge [m]
z_{air}	air gap [m]
η_*	highest wave elevation above SWL [m]
$H_{s,50}$	50-year significant wave height [m]

Table G.1: Used abbreviation in the interface level calculations.

Table G.2 shows the values of the elevations.

Parameter	Value
z_{Tide}	2.37 [m]
$0.5 * z_{Surge}$	0.94 [m]
$\eta *$	12.57 [m]
z_{Air}	1.50 [m]
$z_{Interface}$	MSL+17.4 [m]

Table G.2: Elevation values.

This means that the monopile in HAWC2 has a height of the water depth plus interface level, giving it a total height of 42.4 m. The standard monopile diameter from the reference model of 6 m is used.

Hub height

The hub height can now be calculated by adding the tower height and half the RNA height to the interface height, see Table G.3.

Parameter	Value
$z_{Interface}$	17.4 [m]
Tower height	87.6 [m]
0.5* RNA height	2.5 [m]
Total Hub height	107.5 [m]

Table G.3: Hub height calculations.

Appendix H

H. Flange details

Raw material dimensions

The thickness of the raw material for the flange, tf_{rm}, is sketched below:

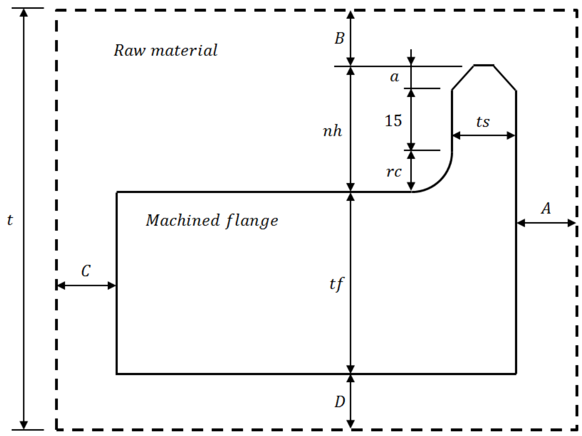

Figure H.1: Raw flange material dimensions [1].

The thickness and width of the raw material of the flange are given by the following equations.

$$tf_{rm} = tf + nh + B + D \qquad \text{Equation H.1}$$

$$wf_{rm} = wf + A + C \qquad \text{Equation H.2}$$

The nose height, nh, is assumed to be constant and set on 40 mm. The machining allowances, A, B, C and D are deduced from measurements and their value is 35, 25, 35 and 25 mm, respectively.

Bolt Extender

The bolt extenders are defined within SWP with the following dimensions:

	M42	**M48**	**M56**	**M64**
Inner diameter of bolt extender $[mm]$	44	50	59	67
Outer diameter of bolt extender $[mm]$	80	95	110	120

Table H.1: Bolt extender parameters.

The lengths of the bolt extenders are dimensioned to accommodate the min- and maximum clamp length of the bolts. The price of the bolt extender is calculated from the external dimensions, the density and price per kg:

$$Price_{be} = \left[\frac{€}{kg}\right] \cdot \rho_{steel} \cdot lbe \cdot \frac{\pi}{4} \cdot dbeo^2 \qquad \text{Equation H.3}$$

The price of the bolt extender material and machining is estimated to $1€/kg$.

Appendix I

I. Eigenmodes reference

Full System Eigenmode	Natural Frequency [Hz]	Damping Ratio [-]	Comments
1st Tower Fore-Aft	0.2400	0.0081	
1st Tower Side-to-Side	0.2400	0.0060	
1st Drivetrain Torsion	0.6000	0.0536	High-speed shaft locked by brake
1st Blade Collective Flap	0.6200	0.0059	All blades in-phase
1st Blade Asymmetric Flapwise Pitch	0.6600	0.0053	Blades 2 & 3 in-phase, blade 1 out-of-phase
1st Blade Asymmetric Flapwise Yaw	0.6900	0.0080	Blades 2 & 3 out-of-phase, blade 1 stationary
1st Blade Asymmetric Edgewise Pitch	1.0700	0.0048	Blades 2 & 3 out-of-phase, blade 1 stationary
1st Blade Asymmetric Edgewise Yaw	1.0800	0.0046	Blades 2 & 3 in-phase, blade 1 out-of-phase
2nd Tower Fore-Aft	1.9400	0.0053	
2nd Tower Side-to-Side	1.6700	0.0183	
2nd Blade Collective Flap	2.0000	0.0062	All blades in-phase
2nd Blade Asymmetric Flapwise Pitch	1.5500	0.0092	Blades 2 & 3 in-phase, blade 1 out-of-phase
2nd Blade Asymmetric Flapwise Yaw	1.6100	0.0053	Blades 2 & 3 out-of-phase, blade 1 stationary

Table I.1: HAWC 2 Eigenmodes reference values for the 5MW-NRELT, but for a different support structure as described in the report (20m) [86].